Energy Transmission Through and Along Thin Films Mediated by Surface Phonon-Polaritons

by

Dye-Zone A. Chen

B.S. Engineering Physics

University of California at Berkeley, 1996

S.M. Mechanical Engineering

Massachusetts Institute of Technology, 1999

SUBMITTED TO THE DEPARTMENT OF MECHANICAL ENGINEERING
IN PARTIAL FULFILLMENT OF THE REQUIREMENTS FOR THE DEGREE OF

DOCTOR OF PHILOSOPHY IN MECHANICAL ENGINEERING

AT THE

MASSACHUSETTS INSTITUTE OF TECHNOLOGY

SEPTEMBER 2007

© 2007 Massachusetts Institute of Technology. All rights reserved.

Signature of Author: _____

Department of Mechanical Engineering
July 13, 2007

Certified by: _____

Gang Chen
Warren and Towneley Rohsenow Professor of Mechanical Engineering
Thesis Supervisor

Accepted by: _____

Lallit Anand
Professor of Mechanical Engineering
Chairman, Department Committee on Graduate Students

Energy Transmission Through and Along Thin Films Mediated by Surface Phonon-Polaritons

by

Dye-Zone A. Chen

Submitted to the Department of Mechanical Engineering

on July 13, 2007 in Partial Fulfillment of the

Requirements for the Degree of Doctor of Philosophy in

Mechanical Engineering

Abstract

Surface phonon-polaritons are hybrid electromagnetic modes that are the result of photons coupling to transverse optical phonons. Recently, these surface modes have received much renewed interest primarily due to the fact that micro-fabrication techniques can now routinely create structures at the length scales of interest (nanometers to microns). This thesis investigates the transmission of energy mediated by surface phonon-polaritons.

First, the heat flux transported along the in-plane direction of a thin film is explored. A kinetic theory-based calculation is performed using a diffusion approximation. These results are further confirmed by simulations using fluctuational electrodynamics. It was found that for amorphous silicon dioxide films tens of nanometers thick, the in-plane heat flux carried by surface phonon-polaritons can exceed the heat flux carried by phonons in the film. The results also show that the effective thermal conductivity due to surface polaritons increases with decreasing film thickness, offering a method to potentially offset the reduction in thermal conductivity due to increased interface scattering of phonons in crystalline thin films.

Both calculations point to the propagation length of the surface phonon-polariton as the source for the large heat flux. An experimental measurement of the surface phonon-polariton propagation length on amorphous silicon dioxide is performed using attenuated total reflection and is found to agree well with the calculated value.

The last part of this thesis examines the energy transmission in the direction normal to the plane of the film. Specifically, the transmission of light through an amorphous silicon dioxide film perforated by sub-wavelength holes is experimentally measured. A five-fold increase through the perforated film versus through a solid film is observed in discrete frequency ranges, which strongly suggests the involvement of surface phonon-polaritons.

Thesis Supervisor: Gang Chen
Title: Warren and Towneley Rohsenow Professor of Mechanical Engineering

Acknowledgements

I think that I've been incredibly lucky to have completed this endeavor, and this is in no small part due to the many people who have helped me along the way. First, I have to thank Prof. Gang Chen for taking me on as a graduate student and being my advisor. I think Gang took a bit of a risk in doing so, and I've greatly appreciated his support over the years. I hope it has at least paid off in some small way for him too. Equally important, Prof. Martin Schmidt shepherded my case to get back into the PhD program. I've probably had an unusual trajectory through MIT, and without Marty's navigation, I probably wouldn't be writing these acknowledgements today. Thanks for being a true advisor, and also for carving out that 6.152J TA spot for me. I'd also like to thank the rest of my thesis committee, Prof. John D. Joannopoulos and Prof. Marin Soljačić, particularly for the collaboration on the EOT simulations.

The various members of the Nano-Engineering group have been a great help, most notably Arvind Narayanaswamy. I have been extremely lucky and privileged to have had him as an officemate, and I can't thank him enough for the countless and patient explanations, derivations, and conversations over the past few years. He is the true epitome of what an academic should be. I also want to thank Gregg Radtke for his help with the numerical integration in the fluctuational electrodynamics chapter. Without his help, I'm sure I would still be struggling with my code. The verbal sparring has also been a blast.

The staff of MTL helped more than just in the fab. Vicky Diadiuk taught me the phrase "Sh_t or get off the pot", and the friendly ribbing from Dennis Ward, Kurt Broderick, and Mr. Tierney made me feel like I'd never left. Thanks to Eric Lim, Bob Bicchieri, and Donal Jamieson for the training on the tools, and especially to Donal for the BBQ and cleaning up the STS chamber that time I DRIE'd a wafer into a million little pieces. Thanks also to Tim McClure of CMSE for letting me do things to his FTIR like duct tape a polarizer into place.

Thanks to my Mom and Dad for putting up with my long and circuitous route to finishing school. Particularly for letting me find my own way, and giving me the rope to make my own mistakes. I'm sure they never thought it would take me this long, but I'm also sure they're happy I'm finally done.

Thanks also to Uchan and Twooey, who helped in their own little ways, especially when I was studying for the quals. I look forward to giving the little ladies lots of ham in the future.

Finally, I owe more than I could ever express to my wife, Iliana, who kept me on the straight and narrow, particularly during my reckless times. I can't imagine a more patient and understanding woman, who in her own words, never broached the dreaded question "When are you graduating?" Thanks for everything, Mamacita.

"Being a graduate student is like becoming all of the Seven Dwarves.
In the beginning, you're Dopey and Bashful.
In the middle, you are usually sick (Sneezy), tired (Sleepy), and irritable (Grumpy).
But at the end, they call you Doc, and then you're Happy."

-Ronald T. Azuma

"The best rides are the ones where you bite off much more than you can chew—
and live through it."

-Doug Bradbury

Table of Contents

Title Page 1

Abstract 3

Acknowledgements 5

Table of Contents 9

List of Figures 13

List of Tables 17

Chapter 1 Introduction 19

1.1 Thermal Conductivity 21

1.2 Extraordinary Optical Transmission 23

1.3 Thesis Organization 25

Chapter 2 Surface Polariton Fundamentals 27

2.1 Dielectric Function 27

2.2 Bulk Polaritons 29

2.3 Single-Interface Surface Polariton 31

2.3.1 Dispersion Relation 32

2.3.2 Propagation Length & Penetration Depth 35

2.4 Thin Film Surface Polaritons 38

2.4.1 Dispersion Relations 39

2.4.2 Propagation Lengths 41

2.5 Coupling 43

2.5.1 Grating 44

2.5.2 Particle Scattering & NSOM 44

2.5.3 Prism 45

Chapter 3 Kinetic Theory Model 47

3.1 Introduction 47

3.2 Model 48

3.3 Boltzmann Transport Equation 51

3.4 Propagation Length 52

3.5 Classical Size Effects 54

3.6 Results 55

3.7 Conclusions 60
Chapter 4 Fluctuational Electrodynamics Model 61
4.1 Introduction 61
4.2 Model 62
4.3 Green's Functions 63
4.4 Fluctuation-Dissipation Theorem 64
4.5 Numerical Integration 66
4.5.1 Gaussian Quadrature 66
4.5.2 Monte Carlo 67
4.5.3 QUADPACK 67
4.6 Results 68
4.6.1 Spectral Flux 69
4.6.2 Propagation Lengths 71
4.6.3 Spectral Peak Location 73
4.7 Conclusions 77
Chapter 5 Propagation Length Measurement 79
5.1 Measurement Approach 79
5.1.1 Modified Otto Configuration 80
5.1.2 Attenuated Total Reflection 81
5.2 Angle Scan vs. Frequency Scan 82
5.3 Layered Media Reflection 82
5.3.1 Finite Film Thicknesses & Substrate 84
5.3.2 Suspended Thin Films 86
5.4 Sample Fabrication 88
5.4.1 Oxide Stress 88
5.4.2 Photoresist Spacer 92
5.5 Measurements 92
5.6 Conclusions 97
Chapter 6 Extraordinary Optical Transmission 99
6.1 Introduction 99
6.2 Sample Fabrication 100
6.3 Experimental Measurements 103
6.3.1 Solid Film 103

6.3.2 Perforated Films 105
6.4 FDTD Simulations 107
6.5 Conclusions 110
Chapter 7 Conclusions 111
7.1 Thesis Contributions 111
7.2 Future Directions 113
Appendix A Fluctuational Electrodynamics Expressions 115
Appendix B FORTRAN Recursion Code 123
Appendix C EOT Mask Set 129
References 131

List of Figures

Figure 1.1 Number of Articles Published Containing the Phrase "Surface Plasmon" [4] 20
Figure 1.2 Thermal Conductivity Size Effects. Data from M. Ashegi 22
Figure 1.3 Extraordinary Optical Transmission [30] 23

Figure 2.1 General Drude and Lorentz Dielectric Functions 29
Figure 2.2 Bulk Polariton Dispersion Relations and Phonon Dielectric Function 30
Figure 2.3 Schematic Depiction of Total Internal Reflection 31
Figure 2.4 Schematic Depiction of the Fields of a Generic Surface Wave 32
Figure 2.5 Bulk Polariton and Surface Polariton Dispersion Relations 34
Figure 2.6 Single-Interface Dispersion Relation and Propagation Length 36
Figure 2.7 Out-of-Plane Penetration Depths 37
Figure 2.8 Complex Plot of Wavevector 38
Figure 2.9 Anti-Symmetric and Symmetric Thin Film Modes 39
Figure 2.10 Graphical Representation of Newton-Raphson Method 40
Figure 2.11 Thin Film Dispersion Relations 41
Figure 2.12 Penetration Depths of a 200nm Film 42
Figure 2.13 SiC Thin Film Surface Polariton Propagation Lengths 43
Figure 2.14 Momentum Mismatch 43
Figure 2.15 Grating Coupling 44
Figure 2.16 Prism Coupling 46

Figure 3.1 Kinetic Theory Picture 47
Figure 3.2 Kinetic Theory Schematic 49
Figure 3.3 Propagation Lengths Due to Scattering 53
Figure 3.4 Crystalline SiC Bulk and Surface Polariton Thermal Conductivities 56
Figure 3.5 Amorphous SiO_2 Bulk and Surface Polariton Thermal Conductivities 57
Figure 3.6 Heat Flux per Unit Temperature Gradient 58
Figure 3.7 Propagation Length, Group Velocity, and DOS 59

Figure 4.1 Fluctuational Electrodynamics Schematic 62

Figure 4.2 Spectral Flux Inside 5 nm Film at x = 0.5 nm, and Spectrally-Integrated Flux.....69
Figure 4.3 Spectral Flux Outside 5 nm Film at x = 0.5 nm, and Spectrally-Integrated Flux..70
Figure 4.4 In-Plane Flux Inside Film as a Function of Distance from Heated Edge.....71
Figure 4.5 In-Plane Flux Outside Film as a Function of Distance from Heated Edge.....72
Figure 4.6 Propagation Lengths Calculated from Complex Dispersion Relations.....73
Figure 4.7 Prefactor and Integrand Inside Film 73
Figure 4.8 SiC Thin Film Dispersion Relations.....74
Figure 4.9 Prefactor and Integrand Outside Film 75
Figure 4.10 SiC Complex Dielectric Function.....75
Figure 4.11 Fluctuational Electrodynamics and Kinetic Theory Comparison.....76

Figure 5.1 Double Prism Configuration for Propagation Length Measurement 80
Figure 5.2 ATR Layer Geometry.....81
Figure 5.3 Surface Polariton Dispersion Relation and Prism Light Lines.....82
Figure 5.4 Calculated SiO_2 ATR Spectra 83
Figure 5.5 Actual ATR Geometry 85
Figure 5.6 Effect of Finite SiO_2 Film Thickness and Si Substrate.....85
Figure 5.7 Effect of Film Thickness for Suspended SiC Films.....87
Figure 5.8 SiC Thin Film Dispersion Relation and KBr Prism Light Line 87
Figure 5.9 Compressive Stress Film on Substrate.....88
Figure 5.10 Tensile Stress Film on Substrate.....88
Figure 5.11 Measured Thermal Oxide Stress.....90
Figure 5.12 PECVD TEOS Oxide Stress.....91
Figure 5.13 Measured and Calculated ATR Spectra with ZnSe Prism.....94
Figure 5.14 Measured and Calculated ATR Spectra with KBr Prism 95
Figure 5.15 Calculated Propagation Length of SiO_2 Surface Phonon-Polariton.....96

Figure 6.1 EOT Sample Geometry and Dimensions 100
Figure 6.2 Process Flow.....101
Figure 6.3 Mask Pattern Scaling.....102
Figure 6.4 SEM of Etched Holes (courtesy of C. T. Harris).....102
Figure 6.5 Measured and Calculated Transmission Through a Solid Film.....104
Figure 6.6 Measured Transmission Through Perforated Oxide Films 105

Figure 6.7 Complex Plot of the SiO_2 Surface Phonon-Polariton Wavevector 107
Figure 6.8 FDTD Computational Cell (courtesy of Rafif Hamam) 108
Figure 6.9 FDTD Simulation Results (courtesy of Rafif Hamam) 110

Figure A.1 Imaginary Part of Integrand.....121
Figure A.2 Real Part of Integrand 121

Figure C.1 Mask Layout.....129
Figure C.2 Mask Detail 1 130
Figure C.3 Mask Detail 2 130

List of Tables

Table 2.1 Plasma Frequencies and Damping Constants for Various Metals 28

Table 2.2 Longitudinal Optical Frequencies, Transverse Optical Frequencies, and Damping Constants for Various Dielectrics 29

Table 4.1 Gaussian Quadrature Formulas 66

Table 4.2 Extracted Propagation Lengths 72

Table 5.1 Measured Thermal Oxide Wafer Bow & Stress 89

Table 5.2 Measured PECVD TEOS Oxide Wafer Bow & Stress 91

Table 5.3 Calculated SiC Propagation Lengths 97

Table 5.4 Calculated SiO_2 Propagation Lengths 97

Table 6.1 FDTD Dielectric Function Parameters 109

Chapter 1

Introduction

The term "polariton" was first introduced by Robert Fano in 1956 [1] and is generically used to describe a hybrid quasi-particle that consists of a photon coupled to some other elementary particle or excitation, such as an electron, a phonon, or a magnon. When light travels through the bulk of a metal and interacts with the free electron gas, the quantum of the hybrid mode is called a plasmon (or more correctly a plasmon-polariton). Plasmons were first described by Ritchie in 1957 [2] in the context of electron energy loss experiments in metal foils. Analogously, photons interacting with phonons in a dielectric are called phonon-polaritons.

The term "surface polariton", in reference to polaritons bound to the surface of a material, was coined by Cunningham in 1974 [3]. A surface polariton is an electromagnetic wave that is trapped on the interface between two different media. Much like surface modes in other disciplines, such as fluids or solid mechanics, the magnitude of the surface polariton's fields decay exponentially in the directions perpendicular to the interface. Surface polaritons can also be thought of as quasi-particles that are manifest as a collective oscillation of charges at the interface that then propagate along that interface. They will be discussed in greater depth in Chapter 2.

Surface polaritons have recently received much renewed interest as illustrated in Figure 1.1. The number of articles published each year on the topic has been growing rapidly. This surge of interest is primarily due to the fact that micro-fabrication techniques now allow routine fabrication of structures at the length scales of interest, which are in the nanometer (10^{-9} m) to micron (10^{-6} m) range.

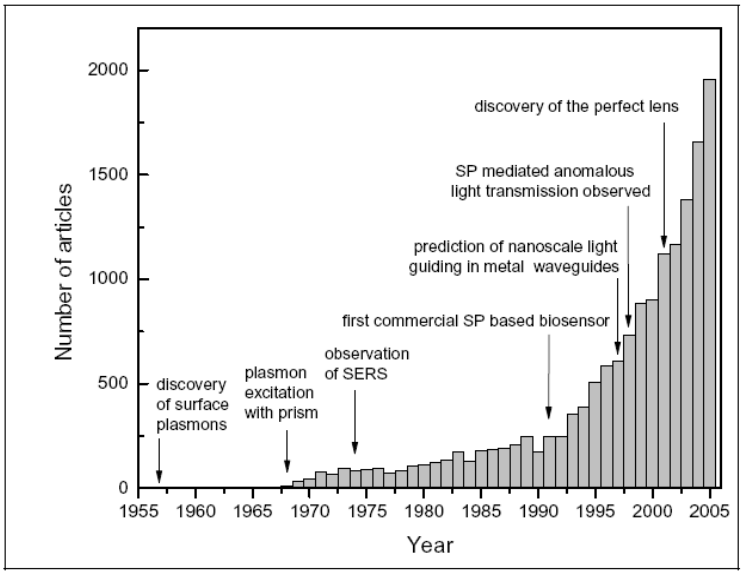

Figure 1.1 Number of Articles Published Containing the Phrase "Surface Plasmon" [4]

As a result, surface polaritons have found numerous applications in many diverse fields. In biology and chemistry, sensors have been developed to detect chemical and biological properties based on surface polariton resonances [5], and magneto-optic data storage using surface plasmon-enhanced read/write heads has also been explored [6]. In Surface Enhanced Raman Scattering (SERS) the molecule under investigation is placed on a polaritonic substrate material such as gold or silver [7]. The resulting Raman signal is increased by up to eight orders of magnitude because of the electromagnetic field enhancement due to the surface polaritons. Combined with the concurrent chemical

enhancement, the overall Raman signal can be increased by as much as 10^{15}. The burgeoning field of nano-optics, or plasmonics, looks to process optical signals in the same manner as electrical integrated circuits. Surface plasmon-based Bragg reflectors [8], Mach-Zender interferometers [9], and optical switches at telecom wavelengths [10] are being used to create these integrated optical circuits. An interesting feature is that these optical circuits could in parallel also carry electrical signals. Finally, the unique properties of surface polaritons have also been applied to the field of radiative heat transfer, where they play an important role in near-field radiation [11] and enhanced thermophotovoltaic devices [12].

Clearly, surface polaritons have found application in many varied branches of science and engineering, and there are several good review papers and books that provide an introduction to the topic [9, 13-19]. In this thesis, the focus is on two particular applications of surface polaritons. The first is the energy transport, or effective thermal conductivity, along the in-plane direction of thin films due to surface polaritons. The second topic is an exploration of the role of surface polaritons in Extraordinary Optical Transmission (EOT). EOT is a recently observed phenomenon where the transmission through a perforated film is significantly greater than expected. Both of these topics will be discussed in greater detail in the Sections that follow.

1.1 Thermal Conductivity

The ability of a material to conduct heat is phenomenologically described by its macroscopic thermal conductivity. In amorphous materials, the thermal conductivity is generally low, with no established methods to increase the capability for heat conduction. Also, for thin films and wires made of crystalline materials, the thermal conductivity decreases as the length scale of the structure decreases [20-22] due to increased scattering of the heat carriers by surfaces

and interfaces. These classical size effects further reduce the thermal conductivity as is shown in Figure 1.2.

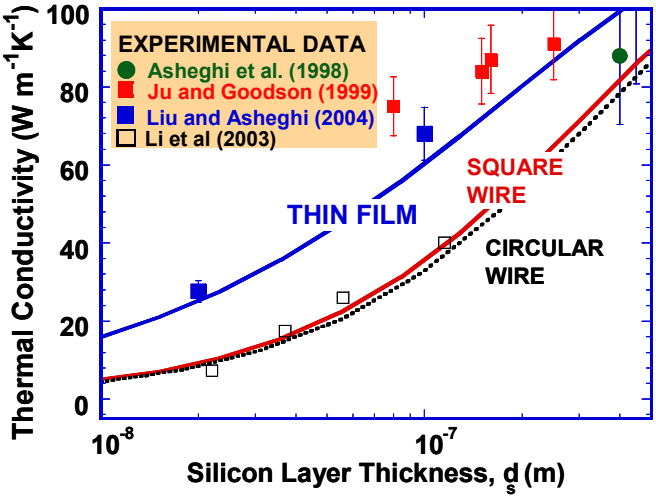

Figure 1.2 Thermal Conductivity Size Effects. Data from M. Ashegi

Recovery of this reduction in thermal conductivity is of interest in devices where thin films and wires are used for reasons other than their thermal performance. For example, in optoelectronics and microprocessors, heat dissipation is becoming one of the limiting factors in performance, and exploiting surface polaritons may provide a channel for this recovery. The motivation for this is three-fold. First, it is well-known that surface polaritons have long propagation lengths [23, 24], particularly on thin films [25], which from a simple kinetic theory perspective could lead to large energy transport. Secondly, in nanostructures surface effects are more important than volumetric effects due to a high surface area to volume ratio. This also suggests that surface polaritons may play an important role in energy transport along films with nanoscale thickness. Finally, it has previously been shown that surface polaritons can be used to increase the radiative heat transfer between two parallel

surfaces [12, 26, 27] (i.e. in the direction perpendicular to the surfaces) and also enhance energy transfer to molecules [28, 29].

1.2 Extraordinary Optical Transmission

One of the most interesting and hotly debated phenomena of the past decade is extraordinary optical transmission. The first experimental observation was reported in 1998 by Ebbesen and co-workers [30]. In their experiments, light was normally incident on an optically-thick metal film which was perforated by an array of sub-wavelength holes. Since the diameter of the holes was smaller than half the wavelength of the light, the theoretically calculated transmission through the perforated film was very small [31]. However, the measured spectra exhibited peak transmission intensities that were much higher than expected.

Shown in Figure 1.3 is a reproduction of a transmission spectrum that was collected.

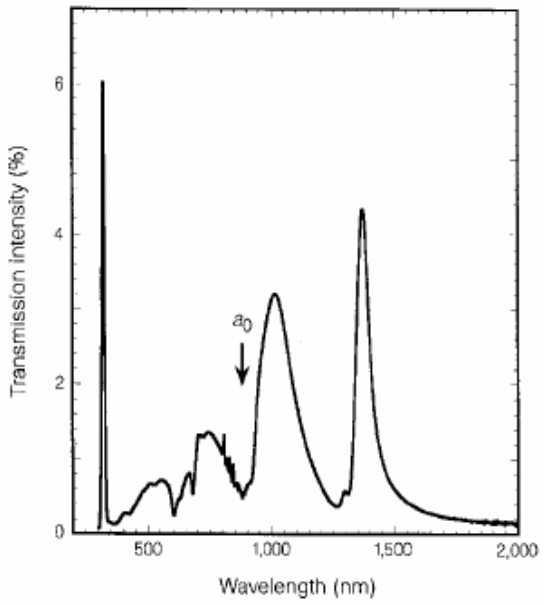

Figure 1 Zero-order transmission spectrum of an Ag array ($a_0 = 0.9\,\mu m$, $d = 150\,nm$, $t = 200\,nm$).

Figure 1.3 Extraordinary Optical Transmission [30]

The silver film was perforated by a square lattice holes of diameter d and period a_0. For the dimensions given in the figure, it is easily calculated that the holes cover 2.2% of the area of the surface. However, it is seen that there are peaks in the transmission intensity (~4%) which are much greater than this. This observation is particularly surprising for two reasons. First, the fact that the observed transmission is greater than the clear area of the holes implies that some of the light which is impinging on the opaque portions of the film is somehow being channeled through the holes. Second, the diameter of the holes is less than half the wavelength of the incident light. Thus, from a classical point of view, there are no propagating modes supported in the holes, and the transmission of the light should be completely cut-off.

Since this and other observations of EOT [32-36], there has been significant research activity in trying to understand the mechanisms by which the transmission occurs [37]. Depending on the relative sizes of the hole diameter, periodicity, and wavelength, there are several possible explanations. These include Fabry-Perot waveguide resonances [38], perforated perfect conductors which mimic surface waves [39, 40], and actual surface plasmons, although as has been noted by several authors, the detailed physical mechanism of the transmission is still unclear [32, 41, 42].

One experiment which may shed further light on the debate is to investigate whether or not EOT occurs for materials such as dielectrics that support surface phonon-polaritons. This idea has also been suggested by other researchers [32], although to date, only one experiment has been done with crystalline silicon carbide [43], and the rest have all been on metals.

1.3 Thesis Organization

Chapter 2 provides a brief overview of the fundamentals of surface polaritons, introduces the dispersion relations, and discusses various coupling mechanisms. In the next chapter, a kinetic theory-based model for the thermal conductivity due to surface polaritons along the in-plane direction of thin films is developed. Chapter 4 presents a more rigorous calculation of the same situation using fluctuational electrodynamics. These results agree well with those from kinetic theory. Both calculations indicate that the key to the large energy carried by surface polaritons is their propagation length. So, in Chapter 5 an experimental measurement of the surface phonon-polariton propagation length via attenuated total reflection is made and compared to calculations. Switching to energy transmission in the normal direction, through the film, Chapter 6 discusses experimental results for the extraordinary optical transmission of light through an amorphous silicon dioxide film perforated by sub-wavelength holes. Finally, conclusions are drawn in Chapter 7.

Chapter 2

Surface Polariton Fundamentals

In this chapter, a brief introduction to surface polaritons is given to highlight the aspects relevant to this thesis. Starting with the concept of a dielectric function, bulk polaritons are discussed, followed by surface polaritons on a single interface and then on a thin film. The chapter concludes with a description of various methods for coupling to the surface modes.

2.1 Dielectric Function

In general, the dielectric function, $\vec{\boldsymbol{\varepsilon}}\left(\vec{\mathbf{k}},\omega\right)$, of a material is a tensor that gives the relationship between the electric field $\vec{\mathbf{E}}$ and the electric displacement $\vec{\mathbf{D}}$, where $\vec{\mathbf{k}}$ is the wavevector and ω is the angular frequency. In the continuum approximation (at length scales greater than atomic) the spatial dispersion can usually be neglected, and for isotropic materials the dielectric function reduces to a scalar function of frequency, $\varepsilon\left(\omega\right)$.

In metals, the dielectric response is dominated by the free electron gas which can be well approximated by a Drude model [44],

$$\varepsilon\left(\omega\right)=1-\frac{\omega_p^2}{\omega^2-i\omega\Gamma} \tag{2.1}$$

where $i = \sqrt{-1}$, Γ is the damping constant, and $\omega_p^2 = ne^2/\varepsilon_0 m$ is the plasma frequency of the material where n is the electron concentration, e is the charge of an electron, $\varepsilon_0 = 8.85\text{x}10^{-12}\,\text{F}\cdot\text{m}^{-1}$ is the permittivity of free space, and m is the mass of an electron.

For the phonon vibrations that dominate in dielectrics such as silicon carbide and silicon dioxide, the corresponding dielectric function is given by a Lorentz model,

$$\varepsilon(\omega) = \varepsilon_\infty \left(1 + \frac{\omega_{LO}^2 - \omega_{TO}^2}{\omega_{TO}^2 - \omega^2 - i\omega\Gamma} \right) \tag{2.2}$$

where ω_{LO} is the longitudinal optical phonon frequency and ω_{TO} is the transverse optical phonon frequency. Good sources for experimental measurements of optical constants include Palik's *Handbook of Optical Constants* [45] and a series of papers by Johnson & Christy [46-48]. Values for a few materials of interest are given in Table 2.1 and Table 2.2. It should be noted that the values for silicon dioxide are for the amorphous phase, and those for silicon carbide are for the 3C polytype which forms a cubic structure [49, 50].

Material	ω_p (rad s^{-1})	Γ (rad s^{-1})
Aluminum (Al)	$1.8\text{x}10^{16}$	$7.59\text{x}10^{13}$
Gold (Au)	$9.1\text{x}10^{15}$	$7.73\text{x}10^{13}$
Silver (Ag)	$5.7\text{x}10^{15}$	$5.08\text{x}10^{13}$

Table 2.1 Plasma Frequencies and Damping Constants for Various Metals

Material	ω_{LO} (rad s^{-1})	ω_{TO} (rad s^{-1})	Γ (rad s^{-1})	ε_∞
Boron Nitride (BN)	2.44x10^{14}	1.97x10^{14}	9.88x10^{11}	4.46
Silicon Carbide (SiC)	1.82x10^{14}	1.49x10^{14}	8.92x10^{11}	6.7
Silicon Dioxide (SiO_2)	-	-	-	-
1st resonance	9.42x10^{13}	8.95x10^{13}	1.17x10^{12}	2.0014
2nd resonance	2.34x10^{14}	2.07x10^{14}	8.92x10^{12}	2.0014

Table 2.2 Longitudinal Optical Frequencies, Transverse Optical Frequencies, and Damping Constants for Various Dielectrics

Shown in Figure 2.1 are plots of the real and imaginary parts of the plasma and phonon dielectric functions normalized to the plasma frequency and the longitudinal optical frequency respectively. Note that below the plasma frequency, and between the transverse optical and longitudinal optical frequencies, the real parts of the dielectric functions are negative. Furthermore it is easily seen that the metal dielectric function is simply a special case of the Lorentz model where $\omega_{LO} = \omega_p$ and $\omega_{TO} = 0$.

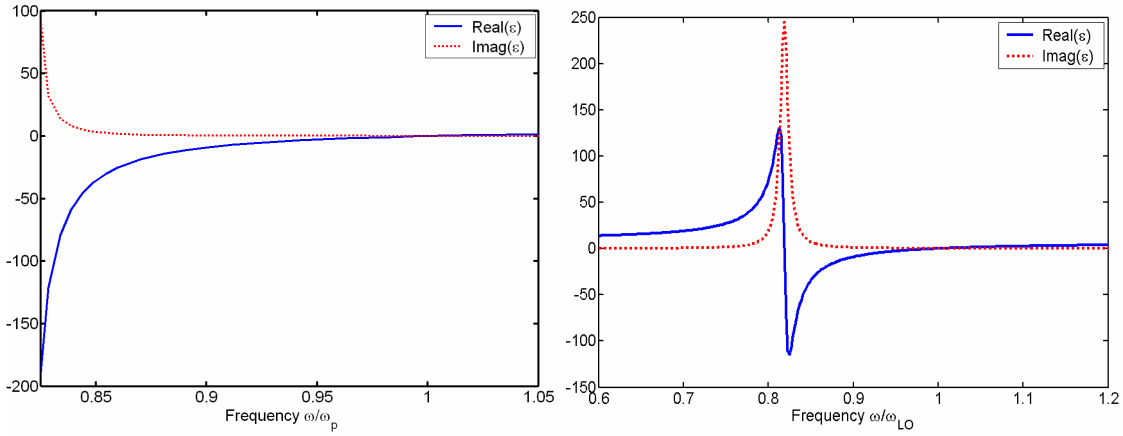

Figure 2.1 General Drude and Lorentz Dielectric Functions

2.2 Bulk Polaritons

As mentioned in Chapter 1, bulk polaritons are mixed modes that can be understood in terms of their dispersion relation, which relate the energy of the mode to the momentum of

the mode. For light propagating in free space, its wavevector is given by $k = 2\pi/\lambda$ where λ is the wavelength, and the associated quantum mechanical momentum is given by $\hbar k$ where $\hbar$ is Planck's constant divided by 2π. Thus, the dispersion relation is simply $\omega = ck$ where $c = 1/\sqrt{\mu_0 \varepsilon_0}$ is the speed of light and $\mu_0 = 4\pi \text{x} 10^{-7}\,\text{N}\cdot\text{A}^{-2}$ is the permeability of free space.

For light propagating through a medium characterized by a dielectric function $\varepsilon(\omega)$ (or a complex index of refraction $\tilde{N} = n + i\kappa = \sqrt{\varepsilon}$), the dispersion relation simply becomes,

$$\omega = \frac{ck}{\sqrt{\varepsilon}}. \tag{2.3}$$

Plotted in Figure 2.2 is the dispersion relation of light propagating in free space (the light line) and the bulk polaritons for a material with a phonon dielectric function (as noted in Section 2.1 the plasma dielectric function is simply a subset).

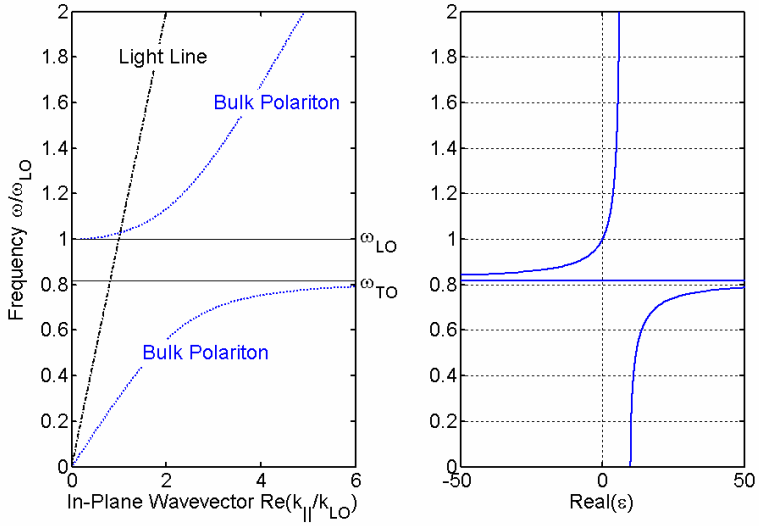

Figure 2.2 Bulk Polariton Dispersion Relations and Phonon Dielectric Function

The dispersion relation plots the energy ($\hbar\omega$) as a function of the real part of the momentum ($\hbar k$). The angular frequency is normalized to the longitudinal optical frequency,

and $\omega_{LO} = ck_{LO}$. From Eqn. (2.3) it is seen that there are only real solutions when the dielectric function is positive. Between the transverse optical and longitudinal optical frequencies the real part of the dielectric function is negative, and thus there is a gap in the bulk polariton dispersion relations where no bulk modes exist.

2.3 Single-Interface Surface Polariton

As the name implies, surface polaritons are electromagnetic waves that propagate along the interface between two media when certain conditions are met. These conditions will be derived and discussed in more detail below. First, consider the situation shown in Figure 2.3.

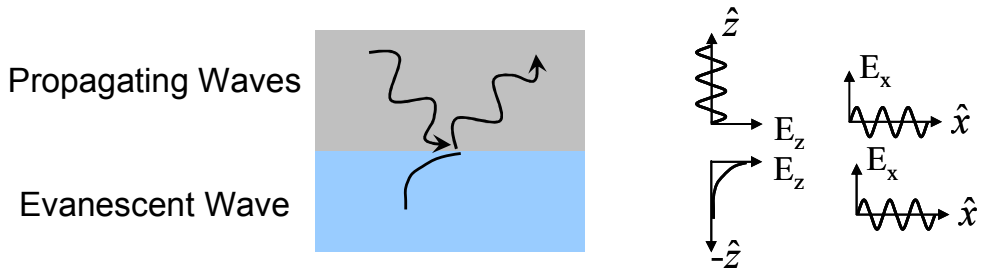

Figure 2.3 Schematic Depiction of Total Internal Reflection

It depicts the well-known phenomena of total internal reflection. On one side of the interface is the medium with a higher index of refraction which supports waves that propagate in the $\hat{x}-$ and $\hat{z}-$directions. When the angle of incidence is greater than the critical angle, the electromagnetic wave in the lower index material is evanescent and decays exponentially in the direction perpendicular to the interface. The evanescent wave propagates only along the surface. In this context, a surface polariton is simply an electromagnetic wave which is evanescent on both sides of the interface, and is shown schematically in Figure 2.4. The collective oscillation of electric charges at the interface forms an electromagnetic wave that propagates along the surface.

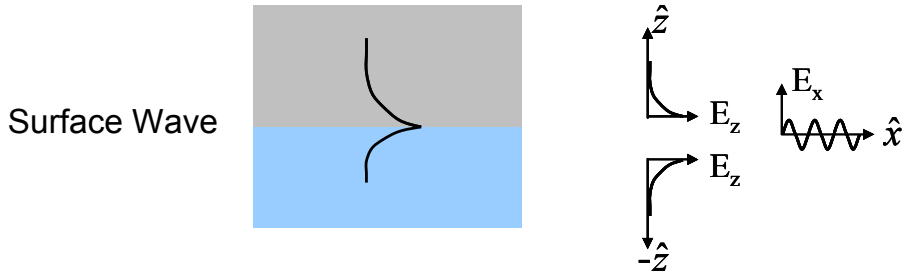

Figure 2.4 Schematic Depiction of the Fields of a Generic Surface Wave

2.3.1 Dispersion Relation

One of the requirements for a surface polariton is that the electromagnetic wave be Transverse Magnetic (TM) polarized [15]. This is equivalent to p-polarized, or parallel-polarized, and means that the electric field is in, or parallel to, the plane of incidence. In the coordinate system of Figure 2.4, this corresponds to $\vec{\mathbf{E}} = E_x\hat{x} + E_z\hat{z}$. Analogously, Transverse Electric (TE) polarization is s-polarized, or *senkrecht* (German for perpendicular), and means that $\vec{\mathbf{E}} = E_y\hat{y}$. The boundary condition at the interface between the two media is that the normal component of $\vec{\mathbf{D}}$, D_z, be continuous. Since there is no free charge and ε is different on either side of the interface, E_z must be discontinuous across the interface. Since only the TM mode has an electric field component that is normal to the interface, TM polarization is a requirement for the excitation of surface polaritons.

A simple way to derive the other condition for the existence of surface polaritons starts with considering the electric fields of the TM mode on either side of the interface

$$\begin{aligned}\vec{\mathbf{E}}_1 &= \left(E_{1x}, 0, E_{1z}\right)e^{i\left[\left(k_{1x}x + k_{1z}z\right) - \omega t\right]} \\ \vec{\mathbf{E}}_2 &= \left(E_{2x}, 0, E_{2z}\right)e^{i\left[\left(k_{2x}x + k_{2z}z\right) - \omega t\right]}\end{aligned}. \tag{2.4}$$

Applying Coulomb's Law, $\nabla \cdot \vec{\mathbf{D}} = 0$, in each medium gives

$$E_{1z} = -\frac{k_x}{k_{1z}} E_{1x}$$
$$E_{2z} = -\frac{k_x}{k_{2z}} E_{2x} \tag{2.5}$$

where $k_{1x} = k_{2x}$ by phase matching [51], and the corresponding magnetic fields can be found from Faraday's Law, $\nabla \times \vec{\mathbf{E}} = -\mu \frac{\partial}{\partial t} \vec{\mathbf{H}}$,

$$H_{1y} = \frac{\varepsilon_1 \omega}{k_{1z}} E_{1x}$$
$$H_{2y} = \frac{\varepsilon_2 \omega}{k_{2z}} E_{2x} \tag{2.6}$$

The boundary conditions also require that the tangential components of $\vec{\mathbf{E}}$ and $\vec{\mathbf{H}}$ be continuous, and thus $E_{1x} = E_{2x}$ and $H_{1y} = H_{2y}$. Substituting into Eqn. (2.6),

$$\frac{\varepsilon_1}{k_{1z}} = \frac{\varepsilon_2}{k_{2z}}, \tag{2.7}$$

and the wave equation, $\nabla^2 \vec{\mathbf{E}} - \mu_0 \frac{\partial^2}{\partial t^2} \vec{\mathbf{D}} = 0$, in each medium gives

$$k_{1z}^2 = \varepsilon_1 \frac{\omega^2}{c^2} - k_x^2$$
$$k_{2z}^2 = \varepsilon_2 \frac{\omega^2}{c^2} - k_x^2 \tag{2.8}$$

Since the normal components of the surface polariton fields decay exponentially away from the interface, k_{1z} and k_{2z} are both purely imaginary and of opposite sign. From Eqn. (2.7) this also forces ε_1 and ε_2 to be of opposite sign. Thus, when ε_1 is a positive dielectric, such as air, this condition requires that $\varepsilon_2 < -1$.

Finally, the dispersion relation is obtained by substituting Eqn. (2.8) into Eqn. (2.7),

$$k_x = \frac{\omega}{c}\sqrt{\frac{\varepsilon_1\varepsilon_2}{\varepsilon_1+\varepsilon_2}}\,. \tag{2.9}$$

Plotted in Figure 2.5 is the dispersion relation of the surface polariton along with the corresponding bulk polaritons at an interface of air and a polar material with a phonon dielectric function. It is seen that the surface polariton has a real solution in the gap of the bulk modes, which is a general characteristic of surface waves. It is interesting to note that the same physical situation that gives rise to the usual Fresnel reflection and transmission coefficients at a single interface also gives rise to surface polaritons. One simply has to allow for the dielectric function to be negative.

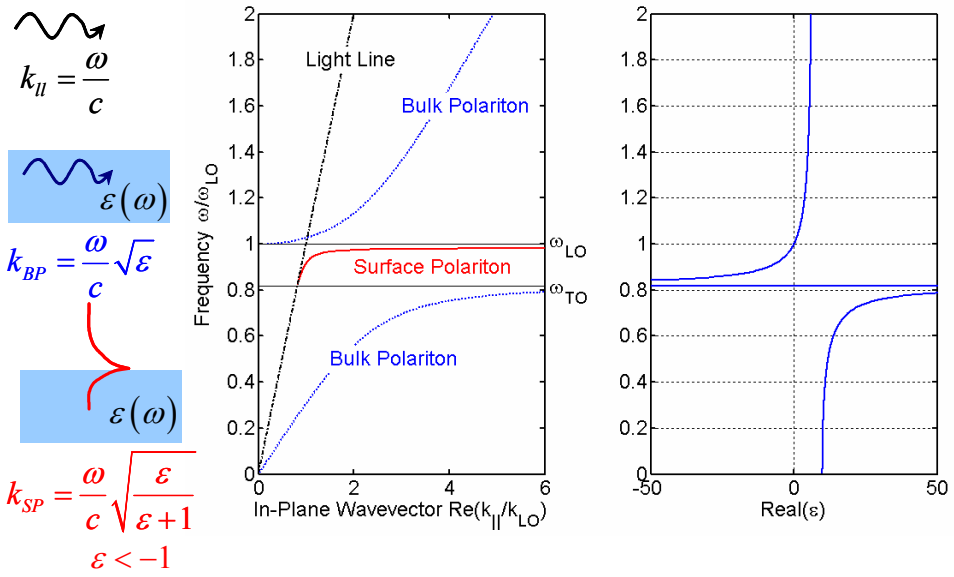

Figure 2.5 Bulk Polariton and Surface Polariton Dispersion Relations

It is also important to note from the dispersion relation or Eqn. (2.9) that at any given frequency the surface polariton has a larger wavevector than the light line. This implies that it is not possible to directly couple from propagating light to the surface mode since there is a momentum mismatch. In this sense, the surface polariton is bound to the surface

and non-radiating. This characteristic can also be seen by considering the Fresnel reflection coefficient for normally incident light,

$$R = |r|^2 = \left| \frac{n_1 - n_2}{n_1 + n_2} \right|^2 . \tag{2.10}$$

When $\varepsilon_2 < 0$, then $n_2 = i \cdot n$ since $n_2 = \sqrt{\varepsilon_2}$. Thus

$$R = \left| \frac{1 - in}{1 + in} \right|^2 = \left| \frac{1 - 2in - n^2}{1 + n^2} \right|^2 = \frac{1 + 2n^2 + n^4}{\left(1 + n^2\right)^2} = 1 \tag{2.11}$$

and all of the incident radiation is reflected when ε_2 is negative. Methods to overcome the momentum deficit and allow propagating light to couple to surface polaritons will be discussed in Section 2.5.

Figure 2.5 also illustrates the hybrid nature of the surface polariton. At low wavevectors, the surface polariton dispersion relation follows the light-line very closely, revealing the photon-like nature of the mode in that regime. As the frequency increases, the dispersion relation flattens and becomes phonon-like.

2.3.2 Propagation Length & Penetration Depth

The discussion thus far has tacitly assumed that ε is real. When the complex nature of ε is considered a choice has to be made. From Eqn. (2.2) and Eqn. (2.9) it is seen the dielectric function and dispersion relation are in actuality complex. Thus, in solving for these dispersion relations, either the wavevector is chosen to be real, resulting in a complex frequency or vice versa [52, 53]. In the case when ω is chosen to be complex, the imaginary part of the frequency gives the lifetime of the mode. This is often the choice made in the case of electron energy loss experiments. When the frequency is chosen to be real, the in-

plane wavevector $k_{\|}$ is complex, and the imaginary part is identified with the propagation length by

$$\Lambda = \frac{1}{2\,\mathrm{Im}\{k_{\|}\}} \tag{2.12}$$

in the same manner as the work done for superlattices [54] and electron energy bands [55]. This perspective is more convenient for transport problems and is chosen for the work in this thesis. The validity of this approach is further supported when the imaginary part of $k_{\|}$ is much smaller than the real part. Plotted in Figure 2.6 are the dispersion relation and propagation lengths for the choice of real frequency and complex wavevector. The zig-zag bend in the dispersion relation is observed for experiments at a fixed frequency and varied angle [56].

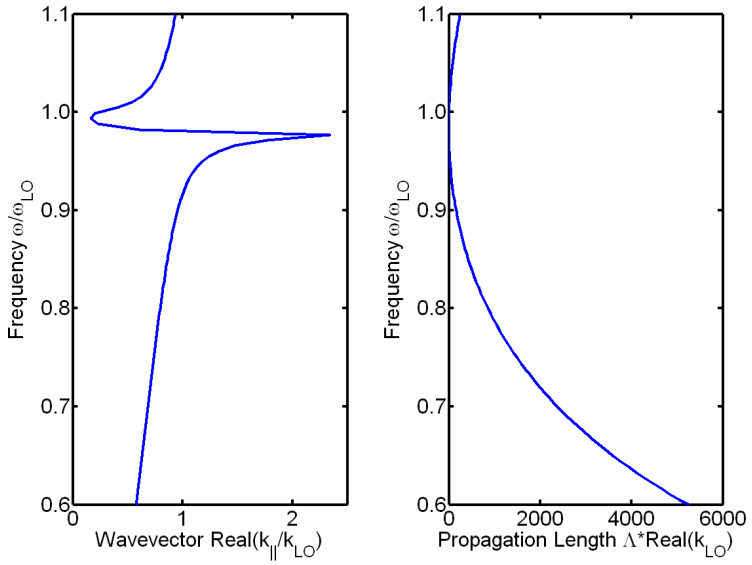

Figure 2.6 Single-Interface Dispersion Relation and Propagation Length

The out-of-plane penetration depths are calculated from Eqn. (2.8) and $\delta = 1/2\,\mathrm{Im}\{k_z\}$ in each medium. In Figure 2.7 it is seen that the surface polariton penetrates

a factor of two or even an order of magnitude more into the air side than into the material. This is due to the fact that there is almost no absorption in the air.

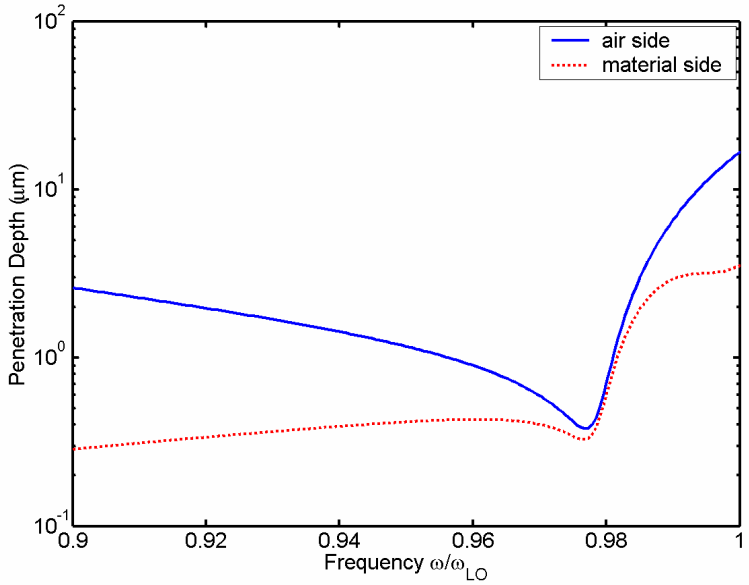

Figure 2.7 Out-of-Plane Penetration Depths

When the wavevector is complex, the criterion to have a surface polariton is not as simple as $\varepsilon_2 < -1$ as previously discussed. Rather, it is more appropriate to look at a complex plot of the real and imaginary parts of the wavevector to determine whether the mode is trapped on the surface (real part of $k_{||}$ is greater than the light line) and propagating (imaginary part of $k_{||}$ is not too large). Shown in Figure 2.8 is a complex plot of the wavevector, k_{sp}, which has been normalized to the light line in vacuum. The contour is generated by plotting the real and imaginary parts of the wavevector at each frequency. Where the real part of the wavevector is greater than the light line the modes are non-radiating. To have a propagating mode, the imaginary part of the wavevector needs to be small, else absorption will damp out the mode. It is seen that there are regions where the imaginary part of the wavevector is less than a tenth of the real part which indicates that the

damping is relatively low. Together, these two characteristics indicate the existence of a surface polariton.

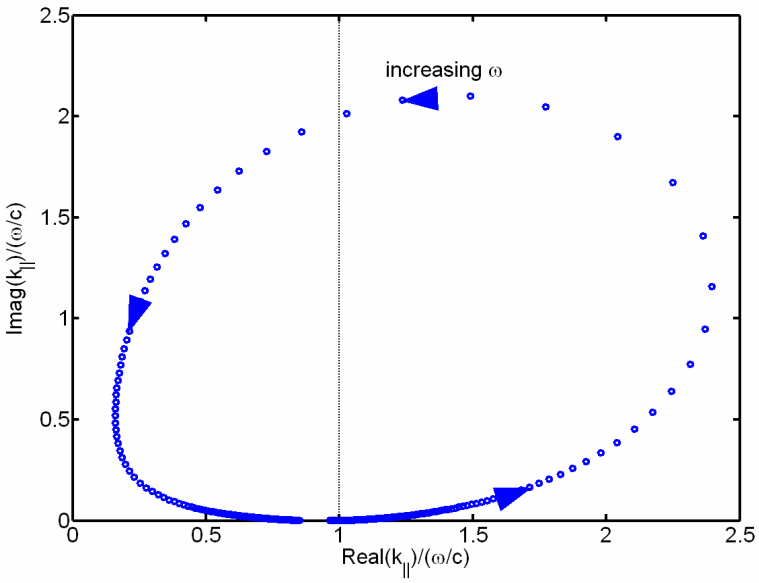

Figure 2.8 Complex Plot of Wavevector

2.4 Thin Film Surface Polaritons

For a thin film, there will be two surface polaritons, one on each surface of the film. It is well-known that as the film thickness decreases, the degeneracy of the two modes is lifted by a splitting into an anti-symmetric mode and a symmetric mode [17]. The modes are labeled in terms of the associated electric field distributions as shown in Figure 2.9. It should be noted that the charge distribution would be described oppositely.

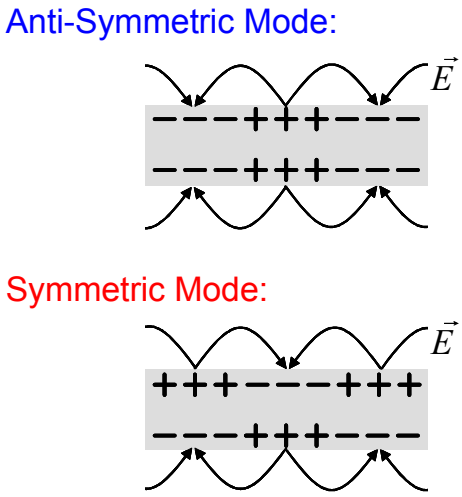

Figure 2.9 Anti-Symmetric and Symmetric Thin Film Modes

2.4.1 Dispersion Relations

The anti-symmetric and symmetric dispersion relations are given respectively by [17]

$$\frac{\varepsilon_2}{\varepsilon_1} = -\frac{k_{2z}}{k_{1z}} \tanh\left(\frac{d}{2i} k_{2z}\right) \tag{2.13}$$

$$\frac{\varepsilon_2}{\varepsilon_1} = -\frac{k_{2z}}{k_{1z}} \coth\left(\frac{d}{2i} k_{2z}\right) \tag{2.14}$$

where ε_2 is the dielectric function of the film surrounded on both sides by ε_1, k_{2z} and k_{1z} are the perpendicular components of the wavevector inside and outside the film respectively, and d is the thickness of the film. It should be noted that these expressions are for the symmetric situation where the medium on both side of the film are the same.

Equation (2.13) and Eqn. (2.14) are transcendental equations that must be solved numerically. There are some general zero finding techniques [57], but in this work a simple Newton-Raphson technique is used to obtain the dispersion relations. This iterative method uses the function $f(x)$, its derivative $f'(x)$, and a current guess x_n, to find a root x, of the function. Using the current guess, the tangent to the function at that point is found. The

x-intercept of the tangent generally gives a better approximation of the desired root, and is given by

$$x_{n+1} = x_n - \frac{f(x_n)}{f'(x_n)}. \tag{2.15}$$

This approach is illustrated graphically in Figure 2.10.

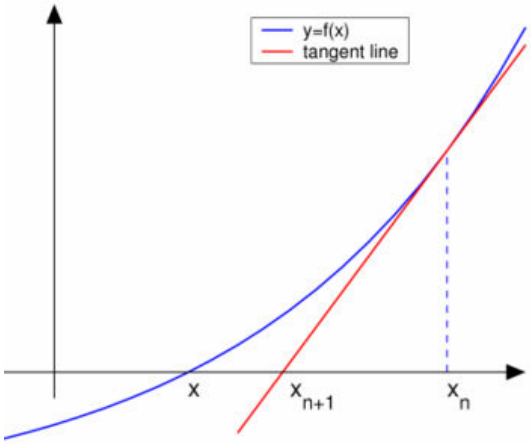

Figure 2.10 Graphical Representation of Newton-Raphson Method

The drawback to the Newton-Raphson method is that it is rather sensitive to the starting guess. To generate the starting guess at each frequency, the $\tanh(x)$ and $\coth(x)$ of Eqn. (2.13) and Eqn. (2.14) are expanded with the first few terms of the Taylor series of $\exp(x)$. This results in an approximate expression for $k(\omega)$. The Newton-Raphson iteration proceeds until $x_{n+1} - x_n \le 10^{-8}$.

The calculated dispersion relations for a thin film surrounded by vacuum are plotted in Figure 2.11 for various film thicknesses. For reference, the dispersion relation at a single interface between a half-space of the material and vacuum is also shown.

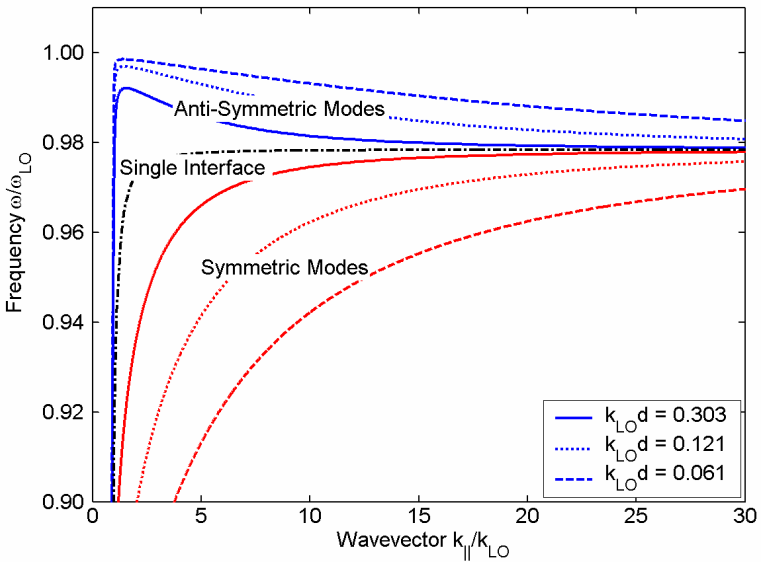

Figure 2.11 Thin Film Dispersion Relations

At large values of $k_{||}$ both the anti-symmetric mode and the symmetric mode of the thin film dispersion relations approach the single interface curve asymptotically. Furthermore, as the thickness of the film increases, both the symmetric and the anti-symmetric dispersion relations approach the single interface curve. The splitting between the two modes is more pronounced as the film thickness decreases, as given by [17, 25, 58, 59],

$$d << \frac{1}{k_{2z}}. \tag{2.16}$$

This is analogous to the splitting of two degenerate energy levels connected by a coupling potential. As the coupling increases (the film thickness decreases), the degeneracy lifts by splitting into a higher energy (anti-symmetric) mode and a lower energy (symmetric) mode.

2.4.2 Propagation Lengths

Shown in Figure 2.12 are the normalized field distributions for a 200 nm thick film. Note that the plot of the fields inside the film has been magnified by 50 times. It is seen that the fields decay rapidly inside the film, but penetrate significantly into the surrounding dielectric.

Furthermore, the penetration depth of the anti-symmetric mode into the medium surrounding the film is three times greater than the symmetric mode.

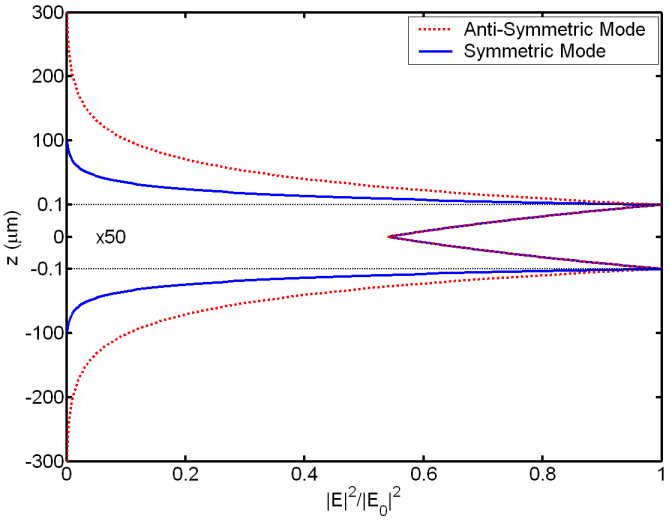

Figure 2.12 Penetration Depths of a 200nm Film

As a result, a greater fraction of the anti-symmetric mode propagates in the surrounding dielectric, which in the case of vacuum, is lossless. Thus, the anti-symmetric mode has a very long propagation length [52], which actually increases as the film thickness decreases [59]. Thus, it is often called the long range surface polariton [59].

The thin film propagation lengths for various film thicknesses of silicon carbide are plotted in Figure 2.13. At a film thickness of about 2 μm the criterion of Eqn. (2.16) is no longer satisfied, and the propagation lengths of both modes approach the single-interface value.

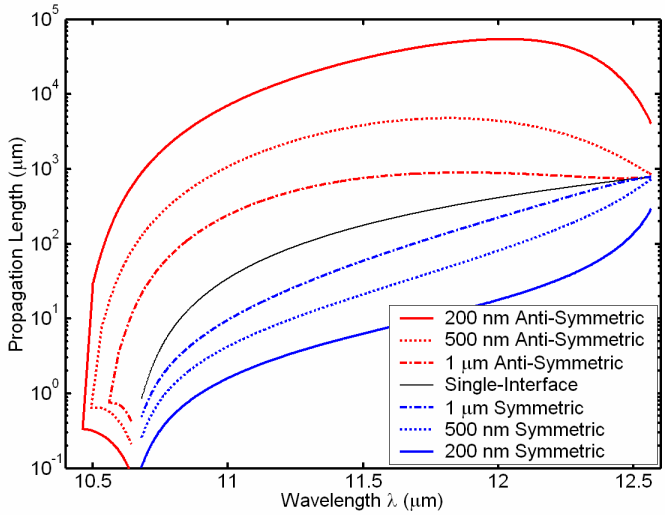

Figure 2.13 SiC Thin Film Surface Polariton Propagation Lengths

2.5 Coupling

As discussed in Section 2.3.1, the dispersion relation of the surface polariton always lies to the right of the light line. As a result, extra momentum is required to couple propagating light to or from a surface polariton as illustrated in Figure 2.14. The three main methods of providing this momentum will be briefly described.

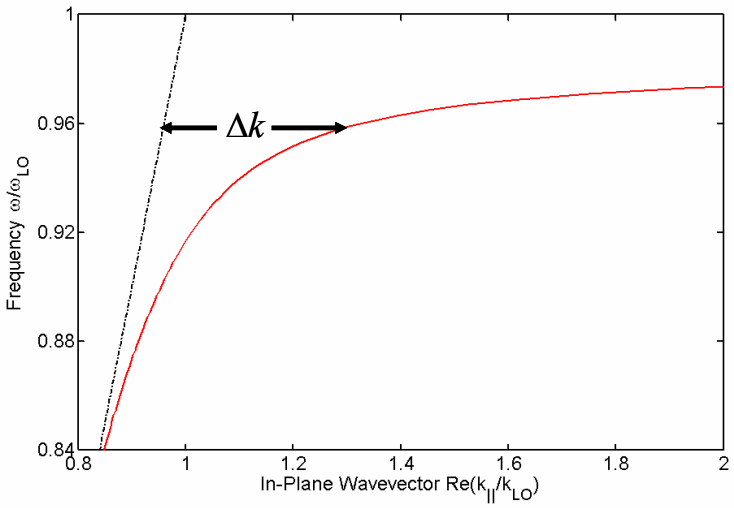

Figure 2.14 Momentum Mismatch

2.5.1 Grating

The first method is to use a grating as illustrated in Figure 2.15. Light that strikes a periodically corrugated surface with period *P* is imparted momentum by virtue of the Fourier transform of the grating's spatial variation [60]. The dominant term is the first component which is given by $2\pi/P$. This method has been studied and used by several researchers to couple to surface polaritons [61-64].

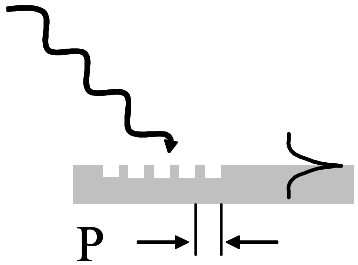

$$\Delta k = \frac{2\pi}{P}$$

Figure 2.15 Grating Coupling

2.5.2 Particle Scattering & NSOM

In an analogous manner, scattering by particles or rough surfaces can also launch surface polaritons. The drawback is that the imparted momentum is not well-defined and only some of the components fulfill the momentum condition. A similar concept is used in Near-field Scattering Optical Microscopy (NSOM) [65]. In this method, the tip of an atomic force microscope or similar hardware is used to perturb the evanescent field of the surface polariton and the scattered light is then collected by a detector. The NSOM technique has been used to map surface polariton field distributions [66, 67] and also to measure propagation lengths [68].

2.5.3 Prism

The last technique for coupling is via total internal reflection and a prism. Consider the evanescent wave that results from total internal reflection as shown in Figure 2.3. The total wavevector on the optically rarer side is given by $k_2^2 = k_x^2 + k_z^2$ where $k_2 = \sqrt{\varepsilon_2}\omega/c$. For the evanescent wave, k_z is purely imaginary, so that $k_x^2 = k_2^2 + |k_z|^2$ which results in an in-plane wavevector which is larger than propagating light. Specifically, it is given by

$$k_x = \sqrt{\varepsilon_p}\,\frac{\omega}{c}\sin\theta_i \tag{2.17}$$

where ε_p is the dielectric function of the prism and θ_i is the incident angle. At the appropriate angle and frequency, the in-plane momentum of the evanescent wave can be made to match that of the surface polariton. Thus, since the energy and momentum match, the evanescent wave can be used to excite the surface polariton.

Two configurations that are used to realize this coupling method are shown in Figure 2.16. Shown in Figure 2.16(a) is the Otto configuration which was developed in 1968 [69, 70]. The air gap is set by spacers, and is generally on the order of the wavelength. Maintaining this gap can be a challenge, particularly in the visible range. Figure 2.16(b) shows the Kretschmann-Raether configuration [71] which has the polaritonic layer in contact with the prism. This configuration requires that the film layer be thin enough for the radiation to tunnel to the other side. The Otto configuration will be used to measure the surface polariton propagation length and will be discussed in greater detail in Chapter 5.

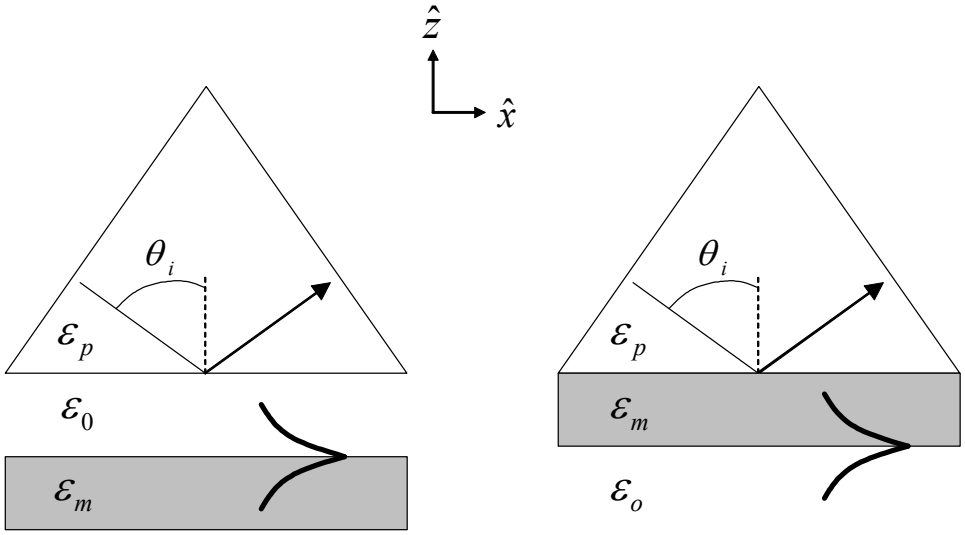

(a) Otto (b) Kretschmann-Raether

Figure 2.16 Prism Coupling

Chapter 3

Kinetic Theory Model

In this Chapter, a kinetic theory-based model for the thermal conductivity due to surface polaritons is developed using the Rosseland diffusion approximation and the Boltzmann transport equation. Calculations for amorphous silicon dioxide and crystalline silicon carbide are presented and compared to the bulk phonon thermal conductivity.

3.1 Introduction

We calculate the contribution of the surface polaritons to the in-plane energy flux using a kinetic theory-based approach. This method assumes a diffusive process where the particles of interest travel for a time τ before colliding. This statistical treatment is illustrated schematically in Figure 3.1.

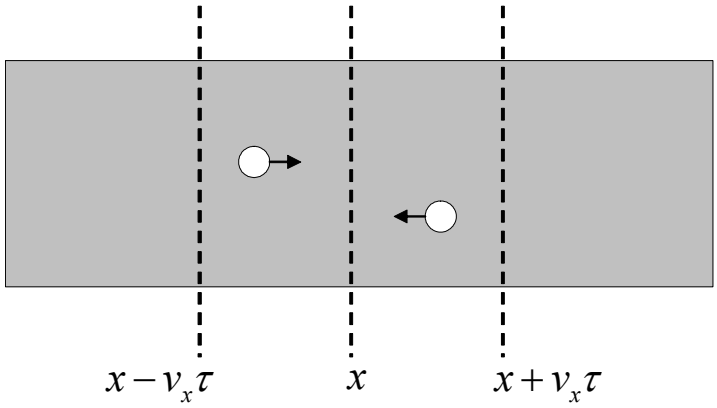

Figure 3.1 Kinetic Theory Picture

The particles are assumed to be moving randomly, so that at any spatial location half will cross in the positive $\hat{x}-$direction, and half in the negative $\hat{x}-$direction. Thus, the net energy flux in the positive direction is given by

$$Q_{+x} = \frac{1}{2}\left(nEv_x\right)\Big|_{x-v_x\tau} - \frac{1}{2}\left(nEv_x\right)\Big|_{x+v_x\tau} \tag{3.1}$$

where n is the number of carriers per volume, E is the energy of each carrier, and v_x is the average particle velocity in the $\hat{x}-$direction. Expanding each term around x and simplifying,

$$Q_{+x} = -\frac{d}{dx}\left(nEv_x\right)v_x\tau\,, \tag{3.2}$$

and chain rule gives

$$Q_{+x} = -v_x\tau\frac{d\left(nE\right)}{dT}\frac{dT}{dx}v_x\,. \tag{3.3}$$

where T is the temperature. Since the temperature rate of change of the energy is the specific heat, c_v, and the average velocity is related by $v_x^2 = v^2/3$, the well-known result for the thermal conductivity is obtained,

$$Q_{+x} = -\frac{1}{3}\left(c_v v\Lambda\right)\frac{dT}{dx} \tag{3.4}$$

where the mean free path is given by $\Lambda = v\tau$. It should be noted that this is only a very cursory treatment, and a more detailed analysis based on the Boltzmann Equation follows below.

3.2 Model

This diffusion approximation is valid when the characteristic length of heat transfer is at least several times longer than the mean free path of the particle of interest, in this case, the

surface polariton in-plane propagation length. An analogous situation is that of radiation through an optically thick, isotropically scattering, and absorbing medium where conduction and convection are ignored. In the field of radiative heat transfer, this is called the Rosseland diffusion approximation [72, 73].

To develop a model of the thermal conductivity due to surface phonon-polaritons with this framework, consider energy transport along the two surfaces of a thin film as shown in Figure 3.2. The thickness of the film is d and the lengths in the $\hat{x}-$ and $\hat{y}-$directions are L_x and L_y respectively. The surface area in the *x-y* plane, A, is $L_x L_y$. There is an imposed temperature gradient in the $\hat{x}-$direction from T_L to T_H, and the temperature is taken to be uniform in the $\hat{y}-$direction. The film is assumed thin enough to neglect temperature gradients in the $\hat{z}-$direction. The material has a frequency-dependent dielectric function given by $\varepsilon_2(\omega)$ and is bounded on either side by a medium with dielectric constant ε_1, which is taken to be vacuum. It is found that with higher dielectric constant surroundings the thermal conductivity increase still occurs, although the onset of the increase is delayed to smaller film thicknesses. The surface polariton fields on both surfaces of the film decay exponentially into the film as well as into the surroundings.

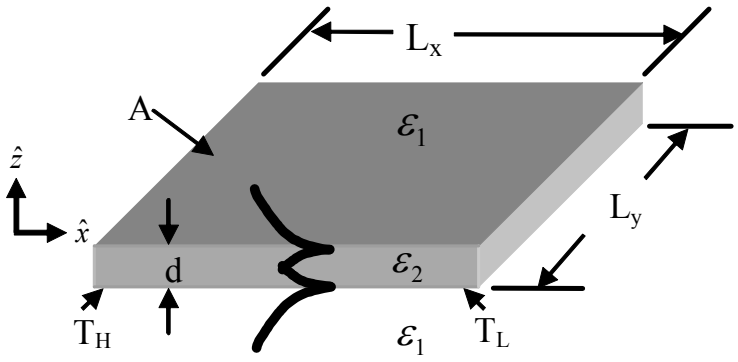

Figure 3.2 Kinetic Theory Schematic

The surface wave heat flux crossing a plane normal to the $\hat{x}-$direction, per unit length in the $\hat{y}-$direction (in units of W m^{-1}), is given by

$$Q_x = \frac{1}{A}\sum_{k_x}\sum_{k_y}\hbar\omega\left(k_x,k_y\right)f\left(T\right)\vec{v}_g\cdot\hat{x}, \tag{3.5}$$

where k_x and k_y are the wavevectors in the $\hat{x}-$ and $\hat{y}-$directions respectively, f is the distribution function (to be discussed in Section 3.3), and $\vec{v}_g$ is the group velocity.

Periodic boundary conditions quantize the wavevectors, $k = 2\pi n/L$, so that Eqn. (3.5) can be expressed as an integral,

$$Q_x = \frac{1}{\left(2\pi\right)^2}\int_{-\infty}^{\infty}\int_{-\infty}^{\infty}\hbar\omega f(T)\left|\vec{v}_g\cdot\hat{x}\right|d^2k_{\|} \tag{3.6}$$

where $d^2k_{\|} = d\theta k_{\|}dk_{\|}$, θ is the in-plane angle from the $\hat{x}-$axis, and $k_{\|}$ is the in-plane wavevector.

In the case of phonons, ω, k_x, and k_y are real quantities, and $k_x = 2\pi n/L_x$ and $k_y = 2\pi m/L_y$ where n and m take on integer values from $-\infty$ to ∞. However, as discussed in Section 2.3.2, in the case of surface polaritons, the dielectric function and dispersion relations are complex. In choosing a real frequency, a complex in-plane wavevector, $k_{sp} = \sqrt{k_x^2 + k_y^2}$, results. The real part of k_{sp}, denoted here as $k_{\|}$, is used with the real frequency in calculating the energy flux, and the imaginary part is used to calculate the propagation length. This approach is further supported by the fact that the imaginary part of k_{sp} is much smaller than $k_{\|}$ in the range over which the dominant contribution to the thermal conductivity integral occurs.

3.3 Boltzmann Transport Equation

The probability of finding a particle at a particular time, t, and location, $\vec{\mathbf{r}}$, with a momentum, $\vec{\mathbf{k}}$, is given by the distribution function, $f\left(\vec{\mathbf{r}},\vec{\mathbf{k}},t\right)$. For non-equilibrium situations, the Boltzmann equation [74] is a conservation equation for this distribution function and is given by:

$$\frac{\partial f}{\partial t}+\frac{\hbar\vec{k}}{m^*}\cdot\vec{\nabla}_r f+\frac{\vec{F}}{\hbar}\cdot\vec{\nabla}_k f=\sum_{k'} f(k')S(k',k)-\sum_{k'} f(k)S(k,k') \tag{3.7}$$

where m^* is the effective mass of the carrier, $\vec{\mathbf{F}}$ is the externally applied force, and $S(k',k)$ and $S(k,k')$ are the respective scattering rates from state k' to k and from k to k'.

Under the relaxation time approximation, with steady-state conditions and no applied external force, the equation simplifies to

$$\frac{\hbar\vec{k}}{m^*}\cdot\vec{\nabla}_r f=-\frac{f-f_o}{\tau} \tag{3.8}$$

where f_0 is the equilibrium distribution and τ is the relaxation time. Using the semi-classical equations of motion, $\hbar\vec{k}/m^*$ is identified as the velocity of the particular $\vec{k}$ state. With no loss of generality, if the temperature is assumed to vary only in the $\hat{x}-$direction, the distribution only varies in the $\hat{x}-$direction as well and can be re-arranged as

$$f(T)=f_o(T)-\Lambda\cos\theta\frac{\partial f}{\partial x}, \tag{3.9}$$

where Λ is the mean free path. For phonons and photons (and thus also for surface phonon-polaritons), f_0 is given by the Bose-Einstein distribution,

$$f_{BE}\left(T\right)=\frac{1}{\exp\left(\frac{\hbar\omega}{k_B T}\right)-1}. \tag{3.10}$$

Substituting Eqn. (3.9) into Eqn. (3.6), the fluxes in the positive and negative $\hat{x}-$directions are given by,

$$Q_{+x} = \frac{1}{(2\pi)^2} \int_{-\frac{\pi}{2}}^{\frac{\pi}{2}} \cos\theta d\theta \int_0^\infty \hbar\omega \left(f_o(T) - \Lambda \cos\theta \frac{d}{dx} f(T) \right) \left| \vec{v}_g \right| k_{\|} dk_{\|} \tag{3.11}$$

$$Q_{-x} = \frac{1}{(2\pi)^2} \int_{\frac{\pi}{2}}^{\frac{3\pi}{2}} \cos\theta d\theta \int_0^\infty \hbar\omega \left(f_o(T) - \Lambda \cos\theta \frac{d}{dx} f(T) \right) \left| \vec{v}_g \right| k_{\|} dk_{\|} . \tag{3.12}$$

and the net flux in the positive $\hat{x}-$direction is

$$Q_{x,net} = -d \frac{dT}{dx} \left[\frac{1}{4\pi d} \int_o^\infty \hbar\omega \Lambda \frac{df}{dT} \left| \vec{v}_g \right| k_{\|} dk_{\|} \right] \tag{3.13}$$

where chain rule has been used on the distribution function, and the term in brackets is defined as the effective thermal conductivity (per unit width in the $\hat{y}-$direction) due to surface polaritons, K_s (in W m^{-1} K^{-1}). Equivalently, using the 2-D density of states per unit area, $g_{2D}(\omega) = k/(2\pi\, d\omega/dk)$,

$$K_s = \frac{1}{2d} \int_0^\infty \hbar\omega \Lambda \frac{df}{dT} \left| \vec{v}_g \right| g_{2D}(\omega) d\omega . \tag{3.14}$$

3.4 Propagation Length

As described in Section 2.3.2, the propagation length of the surface phonon-polaritons is taken to be $\Lambda = 1/2\,\mathrm{Im}\{k_{sp}\}$. The propagation lengths calculated in this manner agree well with approximate expressions found in the literature for surface polaritons on thin films [17].

In calculating the propagation length, scattering due to surface roughness is a potential concern. Following the work of Mills [23], the propagation lengths due to surface roughness scattering of surface polaritons into radiative p-polarized and s-polarized modes

and into other surface phonon-polariton modes are calculated. The input parameters to these models are the surface roughness peak-to-peak height and periodicity. Typical CMOS gate oxides are now less than 2 nm thick, and so an estimate of 1 nm for the film root-mean-square surface roughness height and average distance between peaks was chosen for the calculations. The propagation lengths due to these two loss mechanisms are calculated and plotted in Figure 3.3. For comparison, the anti-symmetric mode propagation lengths for 10 nm and 50 nm films are also shown. It is seen that the propagation lengths due to scattering are several orders of magnitude greater than that due to the surface phonon-polariton attenuation.

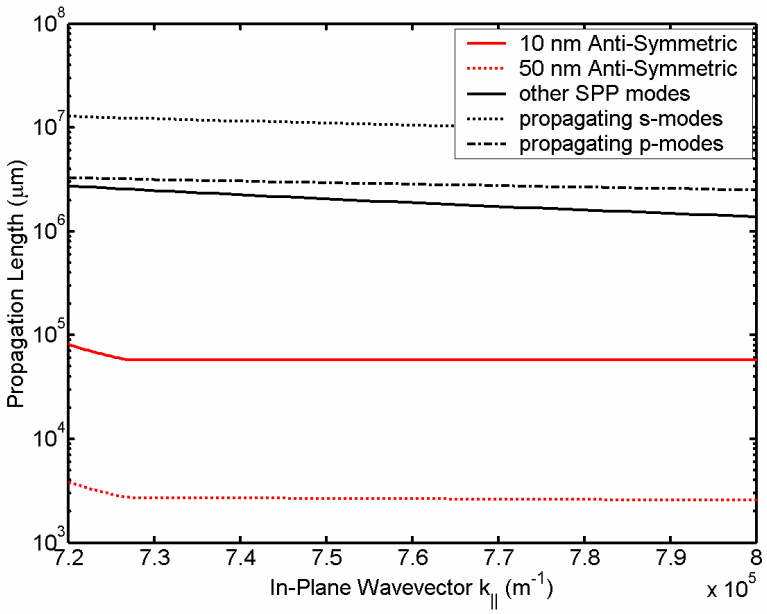

Figure 3.3 Propagation Lengths Due to Scattering

Furthermore, an examination of the integrand of Eqn. (3.14) shows that the majority of the surface phonon-polariton contribution to the thermal conductivity occurs for in-plane wavelengths longer than 1 μm. Since these wavelengths are significantly larger than the surface roughness, the surface scattering will not significantly affect the surface phonon-

polaritons [17]. Thus, the propagation length of the surface wave is used for the mean free path.

3.5 Classical Size Effects

In general, the phonon contribution to the bulk thermal conductivity decreases as the film thickness decreases because of an increase in surface scattering of the phonons. This phenomenon is important when the carrier's mean free path becomes comparable to or larger than the film thickness. This reduction in thermal conductivity can be estimated using a Fuchs-Sonderheim model [75],

$$k_{film} = k_{bulk}\left[1 - \frac{3(1-p)}{2\zeta}\int_0^1 \left(\mu - \mu^3\right)\left(\frac{1-\exp\left(-\frac{\zeta}{\mu}\right)}{1-p\exp\left(-\frac{\zeta}{\mu}\right)}\right)d\mu\right] \tag{3.15}$$

where k_{film} is the effective thermal conductivity of the film, k_{bulk} is the bulk thermal conductivity, $\zeta = d/\Lambda$ is the film thickness normalized to the carrier mean free path, $\mu = \cos\theta$ is the direction cosine, and p is the specularity parameter which indicates the fraction of specularly reflected carriers.

The specularity parameter is a function of the carrier's thermal wavelength, $\lambda = hv/k_B T$ (where v is the average sound velocity), and is approximated by [76]

$$p(\lambda) = \exp\left(-\frac{16\pi^3\eta^2}{\lambda^2}\right) \tag{3.16}$$

where η is the peak-to-peak surface roughness. This implies that for completely diffuse reflection ($p = 0$),

$$\eta >> \frac{\lambda}{4\pi^{3/2}} \approx \frac{\lambda}{20}. \tag{3.17}$$

For SiC, the average sound velocity is 4.2×10^3 m s^{-1} [77] which results in a thermal wavelength of 6 Å, which is of the order of the usual range of about 10 to 20 Å [75] at room temperature. Thus we see that most of the reflection is diffuse.

The other input into the Fuchs-Sonderheim model is the phonon mean free path. Following the work of Dames [78], the silicon carbide mean free path is calculated to be 377 nm at 300 K. However, in amorphous thin films such as SiO_2, the phonons have a very short mean free path due to the lack of a crystal structure. The corresponding phonon mean free path for oxide is only 2.6 nm, which is two orders of magnitude smaller. Thus, size effects in oxide only begin to play a role at much smaller length scales.

3.6 Results

Calculations were performed for crystalline silicon carbide and amorphous silicon dioxide. For crystalline materials, the dielectric function is well-approximated by a damped harmonic oscillator model as given in Section 2.1. However, for amorphous materials such as silicon dioxide (glass), the actual form of the dielectric function is more complicated than the simple expression used above, and consists of several overlapping resonances. As such, the frequency dependence of the dielectric function used in the calculations is obtained from published experimental values of the complex index of refraction [45].

The thermal conductivity due to surface phonon-polaritons is calculated using Eqn. (3.13), and the reduction in phonon thermal conductivity is calculated in accordance with Eqn. (3.15), assuming completely diffuse scattering and using a bulk thermal conductivity of 360 W m^{-1} K^{-1} [79] for 3C-SiC. Both thermal conductivities are plotted as a function of film thickness in Figure 3.4.

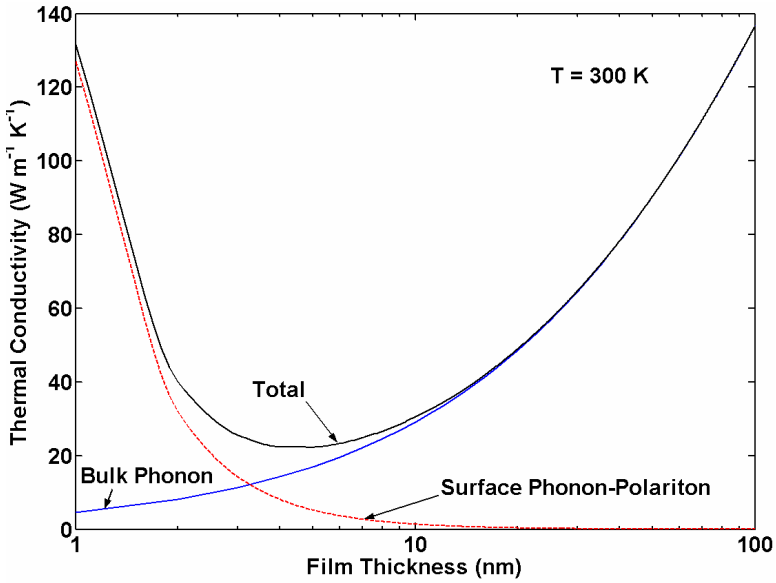

Figure 3.4 Crystalline SiC Bulk and Surface Polariton Thermal Conductivities

It is seen that the phonon and surface phonon-polariton contributions to the thermal conductivity follow distinctly different trends. As expected, the phonon thermal conductivity decreases with decreasing film thickness as more scattering occurs. In contrast, the thermal conductivity contribution from the surface phonon-polaritons increases with decreasing film thickness. The two thermal conductivities are of comparable value when the film thickness is about 3 nm.

The results for SiC results are interesting, but the surface polariton contribution to thermal conductivity isn't significant until the film thickness is extremely thin. This is primarily due to the fact that silicon carbide inherently has a high bulk thermal conductivity due to its crystalline structure. This motivated the examination of an amorphous material such as silicon dioxide which has a much lower bulk thermal conductivity of 1.4 W m^{-1} K^{-1} [80]. However, the surface polariton resonance of an amorphous material is weaker than that of a crystalline one. The calculations for oxide are shown in Figure 3.5.

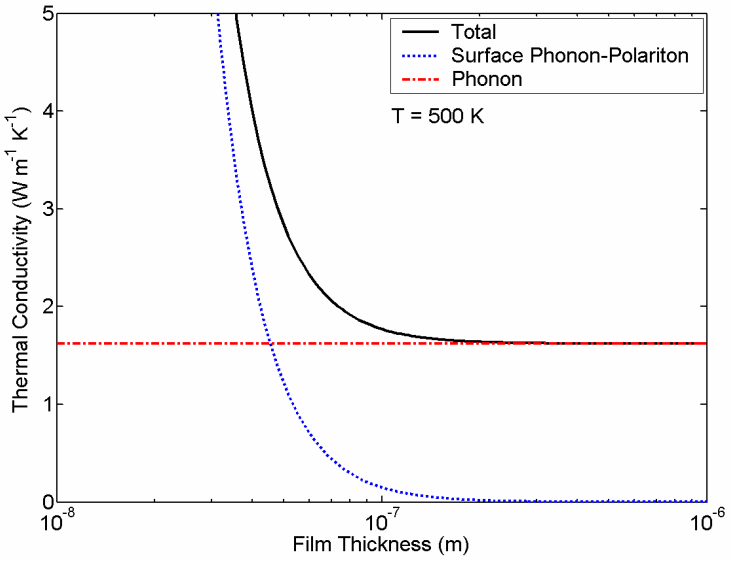

Figure 3.5 Amorphous SiO_2 Bulk and Surface Polariton Thermal Conductivities

It is seen that at film thicknesses greater than 100 nm, the thermal conductivity is dominated by the phonon contribution and is essentially constant. This is because the oxide phonon mean free path as calculated in Section 3.5 is about 3 nm, and thus the phonon contribution to the thermal conductivity is approximately independent of the film thickness in the range considered. The surface phonon-polariton contribution to the oxide follows the same trend as for silicon carbide. As the film thickness decreases below about 60 nm, the thermal conductivity increases dramatically due to the increasing contribution of the surface phonon-polaritons.

An examination of the heat flux per unit temperature gradient ($Q_{x,net}/(dT/dx)$) and thermal conductivity as a function of film thickness due to the surface modes alone shows two distinct regimes as shown in Figure 3.6. For film thicknesses greater than about 1 μm the heat flux is a constant, and the thermal conductivity simply scales inversely proportional to the film thickness. In this regime the surface phonon-polariton modes at the two surfaces are not coupled, and hence the total energy flux is not affected by the thickness of the film.

The increase in the thermal conductivity is due solely to the geometric consideration of transporting the same amount of flux through a smaller cross-sectional area.

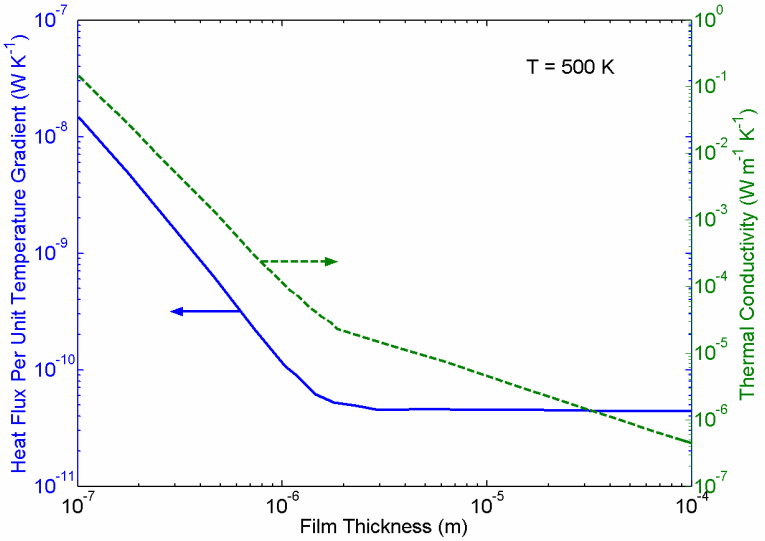

Figure 3.6 Heat Flux per Unit Temperature Gradient

However, in the thickness regime below 1 μm, the slope of the thermal conductivity curve is much larger. This is due to the fact that in addition to the thickness-dependent scaling, the actual amount of heat flux transported by the surface phonon-polaritons is greatly increased. In this regime, the film is thin enough that there is significant interaction between the surface phonon-polaritons on either side of the film.

A more detailed examination of the individual components that constitute the argument of the thermal conductivity integral in Eqn. (3.14) reveals that the mean free path is the source of the increased contribution. The argument of the integral is essentially the product of the mean free path, group velocity, and density of states. These parameters are plotted for the anti-symmetric and symmetric modes of a 50 nm thick film of amorphous silicon dioxide in Figure 3.7.

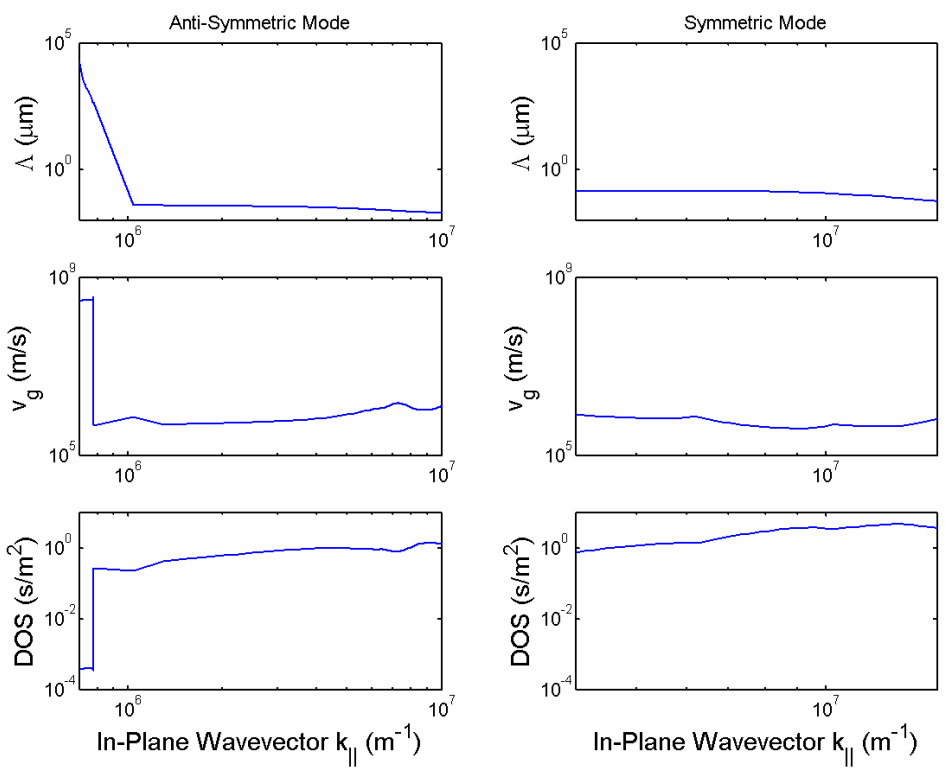

Figure 3.7 Propagation Length, Group Velocity, and DOS

The 2-D density of states is proportional to the in-plane wavevector and is inversely proportional to the group velocity. As such, the density of states and group velocity effectively cancel each other in the thermal conductivity integral. Thus, the source of the increased surface polariton thermal conductivity is the propagation length. As can be seen from Figure 3.7, the overwhelming majority of the surface polariton thermal conductivity is due to the anti-symmetric branch at small wavevectors where the propagation length is orders of magnitude larger than at large wavevectors. As the film thickness decreases, the propagation length of the anti-symmetric branch continues to increase [52, 59] as a greater fraction of the mode propagates in the lossless surrounding dielectric [52]. This large propagation length then enables large contributions to the thermal conductivity. In particular, it is the light-line portion of the anti-symmetric branch where most of the contribution to the thermal conductivity occurs. As seen in Figure 2.11, in this region the

anti-symmetric mode is photon-like, with a large group velocity and large propagation length. A typical propagation length in this region is 2 cm for a 50 nm thick silicon dioxide film. This long propagation length implies that only thin films with lengths much longer than this distance can benefit from the increased surface phonon-polariton thermal conductivity.

3.7 Conclusions

A kinetic theory-based model was developed to calculate the heat flux carried by surface polaritons on nanoscale thin films. The calculations show that the effective thermal conductivity due to the surface polaritons increases as the film thickness decreases. The phenomenon is particularly notable for amorphous materials such as silicon dioxide, where at film thicknesses of about 50 nm, the in-plane heat flux carried by surface phonon-polariton modes can exceed the heat flux carried by the phonon modes. Analysis shows that the long propagation length of the anti-symmetric thin film surface polariton is the source of the increase. This phenomenon potentially points to a novel method to recover the reduction in thermal conductivity due to classical size effects.

Chapter 4

Fluctuational Electrodynamics Model

Given the interesting results of the kinetic theory model, a more rigorous approach to calculating the energy carried by surface modes is carried out using fluctuational electrodynamics. This chapter briefly describes the electromagnetic formulation of thermal radiation using the dyadic Green's functions and the fluctuation-dissipation theorem. Calculations for silicon carbide thin films are presented that compare well with the kinetic theory results.

4.1 Introduction

The fluctuational electrodynamics approach for calculating thermal radiation was pioneered by Rytov in 1958 [81, 82]. The method accounts for the contributions due to evanescent waves, which are not included in geometrical optics, and therefore also describes near-field effects. It has been used by several researchers to compute near-field thermal radiation and directly calculate emission properties of multi-layer structures [11, 12, 56]. The fundamental idea of the approach is that the electric charges of a material in thermal equilibrium will experience random, thermal vibrations. These oscillating charges form fluctuating currents which are then a source for electromagnetic radiation. Thus, this is a method for directly calculating thermal radiation. The explicit relationship between the fluctuating current

density and the temperature is given by the fluctuation-dissipation theorem of statistical physics, which is discussed in Section 4.4.

4.2 Model

The physical system under consideration is shown in Figure 4.1. The film is infinite in the $\hat{x}-$ and $\hat{y}-$ directions, and has a thickness d in the $\hat{z}-$ direction. The material is polar and has a complex, frequency-dependent dielectric function given by $\varepsilon_2(\omega)$. The material is assumed to be isotropic, non-magnetic and is surrounded on either side by vacuum. To compute the in-plane flux, half of the film (from $x = -\infty$ to 0) is taken to be the source, and is assumed to be at a temperature T. The other half of the film is required to solve the electromagnetic problem, but is assumed to be at 0 K. The temperature of the left-half of the film is uniform in the $\hat{y}-$ direction, and the film is assumed thin enough that variations in the $\hat{z}-$ direction are negligible.

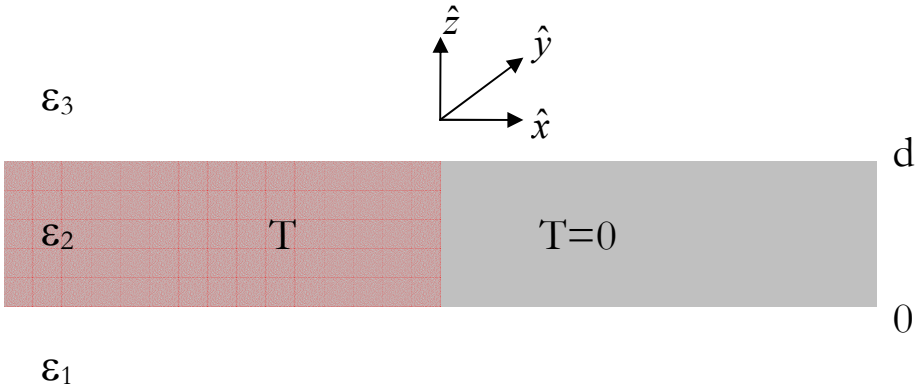

Figure 4.1 Fluctuational Electrodynamics Schematic

4.3 Green's Functions

The first step is to solve for the electric and magnetic fields due to a point source. This is done using the dyadic Green's functions [83] of the vector Helmholtz equation, since the current density source and calculated fields are vectors. The Green's functions can be thought of as the spatial analogues to the impulse response or transfer function. For a current source at $\mathbf{r'}$, the Fourier transform of the electric and magnetic fields at $\mathbf{r}$ are given by,

$$\begin{aligned}\mathbf{E}(\mathbf{r},\omega) &= i\omega\mu_o \int_{V'} d^3r' \ddot{\mathbf{G}}_{\mathbf{E}}(\mathbf{r},\mathbf{r'},\omega)\cdot\mathbf{J}(\mathbf{r'},\omega) \\ \mathbf{H}(\mathbf{r},\omega) &= \int_{V'} d^3r' \ddot{\mathbf{G}}_{\mathbf{H}}(\mathbf{r},\mathbf{r'},\omega)\cdot\mathbf{J}(\mathbf{r'},\omega)\end{aligned} \tag{4.1}$$

where $\ddot{\mathbf{G}}_{\mathbf{E}}(\mathbf{r},\mathbf{r'},\omega)$ and $\ddot{\mathbf{G}}_{\mathbf{H}}(\mathbf{r},\mathbf{r'},\omega)$ are the dyadic Green's functions which are related by $\ddot{\mathbf{G}}_{\mathbf{H}}(\mathbf{r},\mathbf{r'},\omega) = \nabla\times\ddot{\mathbf{G}}_{\mathbf{E}}(\mathbf{r},\mathbf{r'},\omega)$, $\mathbf{J}(\mathbf{r'},\omega)$ is the current density, and the integration is performed over the V', which is the volume containing the source.

To calculate the power flow, we are interested in terms of the form $\langle E_i(\mathbf{r},\omega)H_j^*(\mathbf{r},\omega)\rangle$ where the brackets are needed to indicate the statistical ensemble average since the thermal radiation is stochastic, *i* and *j* denote the Cartesian coordinates, and the * indicates the complex conjugate. Using Eqn. (4.1),

$$\langle E_i(\mathbf{r},\omega)H_j^*(\mathbf{r},\omega)\rangle = i\omega\mu_o \int_{V'} d^3r' \int_{V''} d^3r'' G_{E_{il}}(\mathbf{r},\mathbf{r'},\omega) G^{T*}_{H_{jm}}(\mathbf{r},\mathbf{r''},\omega)\langle J_l(\mathbf{r'},\omega)J_m(\mathbf{r''},\omega)\rangle \tag{4.2}$$

where the ^{T} indicates the matrix transpose.

The Green's function used in these calculations was developed in terms of *s*- and *p*-polarized waves which allows for the explicit inclusion of the Fresnel coefficients of a multi-layer geometry [56, 84]. When the observation and source points are in the same layer, the electric Green's function is given by [84],

$$\vec{\mathbf{G}}_{\mathbf{E}}\left(\mathbf{r},\mathbf{r}',\omega\right)=\int_{-\infty}^{\infty}\int_{-\infty}^{\infty}\frac{dk_x dk_y}{4\pi^2}e^{i\left(k_x\left(x-x'\right)+k_y\left(y-y'\right)\right)}\begin{bmatrix}\dfrac{i}{2k_{z2}}\left[\hat{s}\hat{s}+\hat{p}\hat{p}\right]e^{ik_{z2}|z-z'|}-\dfrac{1}{k_0^2\varepsilon_2}\delta\left(z-z'\right)\hat{z}\hat{z}\\ +\dfrac{i}{2k_{z2}}\left[\hat{s}\rho_{23}^{s}\hat{s}+\hat{p}_2^{+}\rho_{23}^{p}\hat{p}_2^{-}\right]e^{ik_{z2}\left(z+z'\right)}\\ +\dfrac{i}{2k_{z2}}\left[\hat{s}\rho_{21}^{s}\hat{s}+\hat{p}_2^{-}\rho_{21}^{p}\hat{p}_2^{+}\right]e^{ik_{z2}\left(d-z+d-z'\right)}\end{bmatrix} \quad (4.3)$$

where $k_0=\omega/c$, $k_\rho=\sqrt{k_x^2+k_y^2}$, $k_{z2}=\sqrt{\varepsilon_2 k_0^2-k_x^2-k_y^2}$, $\hat{s}=\left(k_y\hat{x}-k_x\hat{y}\right)/k_\rho$,

$\hat{p}=\left(k_\rho/k_2-k_{z2}\left(z-z'\right)/\left(|z-z'|k_2\right)\right)\hat{z}$, $\hat{p}_2^{\pm}=-k_{z2}\left(k_x\hat{x}+k_y\hat{y}\right)/\left(k_2k_\rho\right)\pm k_\rho/k_2\,\hat{z}$, and

$\rho_{2j}^{s,p}=r_{2j}^{s,p}/\left(1-r_{21}^{s,p}r_{23}^{s,p}e^{2ik_{z2}d}\right)$ for the *s*- and *p*-polarized waves respectively, and $j=1,3$. r_{12} and r_{23} are the Fresnel reflection coefficients at the interfaces between layers 2 and 1, and between layers 2 and 3 respectively. The magnetic Green's function is obtained by taking the curl of Eqn. (4.3). The corresponding expression for the Green's function is used when the source and observation points are in different layers and can be found in the references [84].

4.4 Fluctuation-Dissipation Theorem

The ensemble average of the currents in Eqn. (4.2) is related to the temperature of the system by the fluctuation-dissipation theorem [85] from statistical physics. It was first derived by Callen and Welton in 1951 [86]. It relates the microscopic fluctuations of a system in thermodynamic equilibrium to macroscopic, dissipative quantities. For a generalized force and velocity related by a complex impedance,

$$V\left(\omega\right)=Z\left(\omega\right)Q\left(\omega\right)=\left(R\left(\omega\right)+iX\left(\omega\right)\right)Q\left(\omega\right) \quad (4.4)$$

the spectral density of the generalized force is given by,

$$\left\langle V^2\left(\omega\right)\right\rangle=\frac{2R\left(\omega\right)}{\pi}\frac{\hbar\omega}{\exp\left(\hbar\omega/k_BT\right)-1} \quad (4.5)$$

where k_B is Boltzmann's constant, and T is the temperature.

For an isotropic and local medium in thermal equilibrium at a temperature T, the theorem states that the cross-spectral correlation function of the current density is given by,

$$\left\langle J_i(\mathbf{r},\omega) J_j(\mathbf{r}',\omega) \right\rangle = \frac{\varepsilon_o \varepsilon'' \omega \Theta(\omega,T)}{\pi} \delta_{ij} \delta(\mathbf{r}-\mathbf{r}') \tag{4.6}$$

where ε'' is the imaginary part of the dielectric function, δ_{ij} is the Kronecker delta function, $\delta(\mathbf{r}-\mathbf{r}')$ is the Dirac delta function, and $\Theta(\omega,T) = \hbar\omega / \left[\exp(\hbar\omega/k_B T) - 1\right]$. The zero-point energy is neglected due to reciprocity of the heat transfer conductances. The Kronecker delta function is due to the material being isotropic, and the Dirac delta function is a result of being spatially local. For the net $\hat{x}$-directed flux, substituting Eqn. (4.6) into Eqn. (4.2) gives,

$$\left\langle E_y H_z^* - E_z H_y^* \right\rangle = \frac{i\omega^2 \mu_0 \varepsilon_0 \varepsilon'' \Theta(\omega,T)}{\pi} \int_0^d dz' \int_{-\infty}^{\infty} dy' \int_{-\infty}^{0} dx' \left(G_{E_{yj}} G_{H_{jz}}^{T*} - G_{E_{zj}} G_{H_{jy}}^{T*} \right) \tag{4.7}$$

where repeated indices are summed.

The integration over the $\hat{y}-$ direction of the source region in Eqn. (4.7) results in a Dirac delta function which collapses the two integrations over k_y into one. However, the corresponding integration in the $\hat{x}-$ direction is the Fourier transform of the step function, which consists of two terms given by $\pi\delta(k_{x'} - k_x) + i/(k_{x'} - k_x)$ where k_x is for the $\ddot{\mathbf{G}}_{\mathbf{E}}$ integration and $k_{x'}$ is for $\ddot{\mathbf{G}}_{\mathbf{H}}$. The first term leads to the expression for the in-plane flux in the case where the entire film is at the same temperature. As expected, this term does not contribute to the net $\hat{x}-$ direction flux. Thus the focus is on the second term which unfortunately introduces a singularity into the integrand whenever k_x equals $k_{x'}$.

4.5 Numerical Integration

The final expression after analytical simplification is given explicitly in Appendix A. The resulting integral is a virtual "perfect storm" of numerical integration with four dimensions, infinite limits, a highly oscillatory integrand, and multiple singularities. In addition to the singularity whenever k_x equals $k_{x'}$, there are also singularities when z equals z', when k_x and k_y simultaneously equal zero, and when $k_{x'}$ and k_y simultaneously equal zero. Three methods of evaluation are briefly discussed. A good, basic introduction to numerical integration is the book by Davis & Rabinowitz [87].

4.5.1 Gaussian Quadrature

One method of approximating an integral is to use a Gaussian quadrature rule. The integral is approximated as a weighted sum of the function evaluated at specified points. The points, x_k, are the roots of orthogonal polynomials from which the weights, w_k, are calculated for specific weighting functions. Three common quadrature formulas are listed in Table 4.1. The drawback to these quadrature schemes is that to obtain reasonable accuracy, they require "smooth" functions which closely approximate the weighting function. When applied to the integral of interest, it was found that the solution did not converge, but continued to oscillate even as the number of evaluation points was increased.

Quadrature Type	Formula
Gauss-Hermite	$\int_{-\infty}^{\infty} f(x)dx = \int_{-\infty}^{\infty} e^{-x^2}\left[e^{x^2} f(x)\right]dx \approx \sum_{k=1}^{N} w_k e^{x_k^2} f(x_k)$
Gauss-Laguerre	$\int_0^{\infty} f(x)dx = \int_0^{\infty} e^{-x}\left[e^{x} f(x)\right] \approx \sum_{k=1}^{N} w_k e^{x_k} f(x_k)$
Gauss-Legendre	$\int_a^b f(x)dx = \frac{b-a}{2}\int_{-1}^{1} f\left(\frac{b-a}{2}x + \frac{b+a}{2}\right)dx \approx \frac{b-a}{2}\sum_{k=1}^{N} w_k f\left(\frac{b-a}{2}x_k + \frac{b+a}{2}\right)$

Table 4.1 Gaussian Quadrature Formulas

4.5.2 Monte Carlo

Another method of integrating difficult integrals is to use the Monte Carlo method. The mean value of an integral over an interval is given by

$$\overline{f}(x) = \frac{\int_a^b f(x)\,dx}{(b-a)}. \tag{4.8}$$

Given a random sampling of n points in the interval $[a,b]$, the average value of the function evaluated at those points is given by

$$\hat{f}_n = \frac{1}{n}\sum_{i=1}^{n} f(x_i). \tag{4.9}$$

With a large enough number of points, it would be expected that Eqn. (4.8) is approximately equal to Eqn. (4.9), and

$$\int_a^b f(x)\,dx \approx \frac{b-a}{n}\left[f(x_1) + f(x_2) + \ldots + f(x_n)\right]. \tag{4.10}$$

The advantage of the Monte Carlo method is that arbitrarily difficult integrals can be evaluated. However, the downside is that convergence goes as $n^{-1/2}$ [88], and thus a large number of computationally expensive function evaluations are required for accuracy. Quasi-random number sequences such as Niederreiter [89], Sobol [90], and Faure [91] sequences can accelerate convergence by more uniformly covering the domain. However, it was found that with 10^9 points, the integral of interest had not yet converged.

4.5.3 QUADPACK

In the end, the integral was evaluated numerically using QUADPACK [92] which is a library of FORTRAN subroutines for estimating one-dimensional integrals. The adaptive routines

split the domain of integration into intervals and then evaluate the integral over each interval using Gauss-Kronrod rules [93]. A higher order rule and a lower order rule are used in each interval, and the difference gives an estimate of the error. Intervals with large errors are further sub-divided to concentrate effort where required. In particular, a routine using adaptive bisection with the Wynn epsilon algorithm [94] to speed up the integration of integrable singularities was extended to 4-D to perform the integration over k_x, $k_{x'}$, k_y, and z'. An example of the recursive code implementation is given in Appendix B. Furthermore, in the actual code, the integration is split around each of the singularities mentioned above as the QUADPACK routine better handles singularities at the endpoints.

For practical computational purposes, the infinite limits of integration in k_x, $k_{x'}$, and k_y,are set to a value of 10^{10}. The effect of this truncation is to set a bound on the smallest x location which can be evaluated. The dependence of the integral on wavevector and position is of the form $\exp(-k_x x)$ so that at a particular x location, the contribution due to increasingly larger wavevectors decreases and becomes negligible. Using a criterion of e^{-5}, the smallest x position that can be evaluated with reasonable confidence is 0.5 nm. Due to the oscillatory nature of the integrand, convergence was slow to obtain. With a relative error specification of 10^{-3}, each spatial location and frequency took between 3 and 72 hours to compute on a 3 GHz Unix workstation with 4 GB of RAM.

4.6 Results

Calculations were performed for silicon carbide, using a Lorentz model, Eqn. (2.2), for the dielectric function. The constants ($\varepsilon_\infty = 6.7$, $\omega_{LO} = 1.82\text{x}10^{14}$ rad/s, $\omega_{TO} = 1.49\text{x}10^{14}$ rad/s, $\gamma = 8.92\text{x}10^{11}$ rad/s) were obtained by a fit to literature values [45]. Given the form of the

Green's functions, it was straightforward to separate the contributions due to the TE and the TM modes. As expected, it was found that only the TM mode had a significant contribution to the flux, which is consistent with the involvement of surface phonon-polaritons.

4.6.1 Spectral Flux

The spectral flux inside a 5 nm thick film is plotted in Figure 4.2 for various z heights in the film. As discussed in Section 4.5.3, these calculations were done 0.5 nm from the heated edge of the film, and the inset to the figure shows the spectrally-integrated flux as a function of z location in the film. Figure 4.3 shows the analogous plots for outside the film.

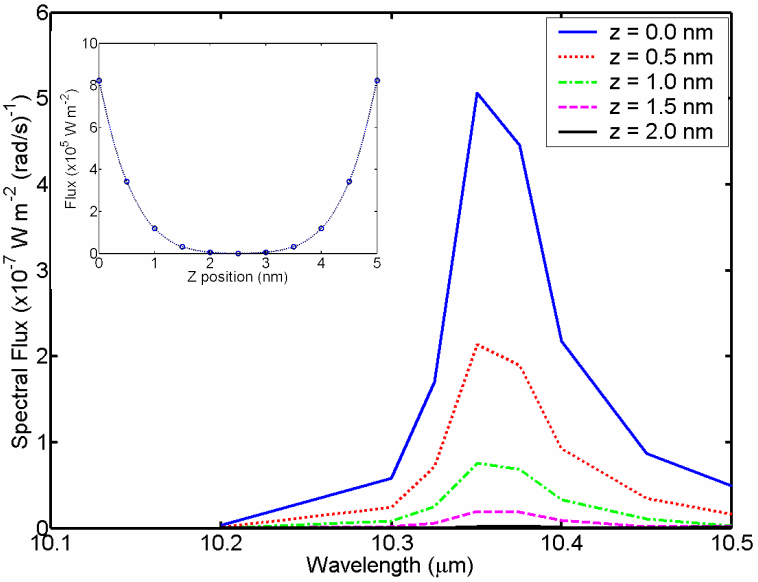

Figure 4.2 Spectral Flux Inside 5 nm Film at x = 0.5 nm, and Spectrally-Integrated Flux

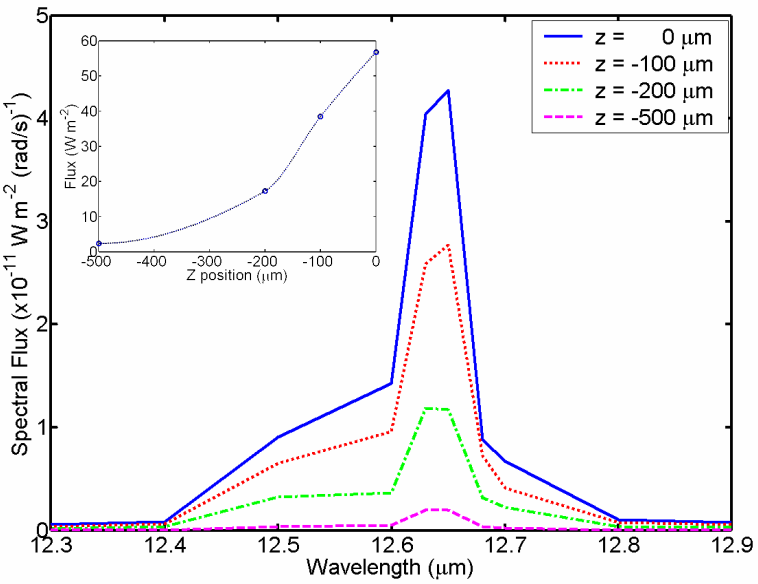

Figure 4.3 Spectral Flux Outside 5 nm Film at x = 0.5 nm, and Spectrally-Integrated Flux

Immediately, two observations are made. The first is that the wavelength where the peak spectral flux occurs is different inside the film and outside. Second, it is seen that inside the film, the majority of the in-plane power is carried near the edges of the film, and that it then decays to zero at the center. The flux outside the film is nearly four orders of magnitude smaller, but the penetration into the air is significantly greater, on the order of 100 μm. This trend can be understood by considering the fields of the anti-symmetric and symmetric surface polariton modes of a thin film. The field of the symmetric mode is mainly inside the film, where the damping of the material provides absorption. In contrast, most of the anti-symmetric mode propagates outside the film. Thus, with vacuum surrounding the film, the anti-symmetric mode experiences very little damping and the fields penetrate much farther. Similarly, the in-plane propagation length of the anti-symmetric mode should also be greater. The spectral fluxes for other film thicknesses show the same trends.

4.6.2 Propagation Lengths

The propagation lengths are extracted by calculating the average flux as a function of x position. Using spline interpolation, the flux is integrated over z and then divided by the film thickness to calculate an average flux. Plotted in Figure 4.4 is the average flux inside the film as a function of distance from the heated edge. It is seen that the flux decays exponentially with distance as the energy is absorbed by the film. The propagation lengths inside the film are calculated to be on the order of several nanometers and are listed in Table 4.2. Outside the film, the average in-plane flux is higher and has a much longer propagation length, on the order of tens of centimeters as shown in Figure 4.5.

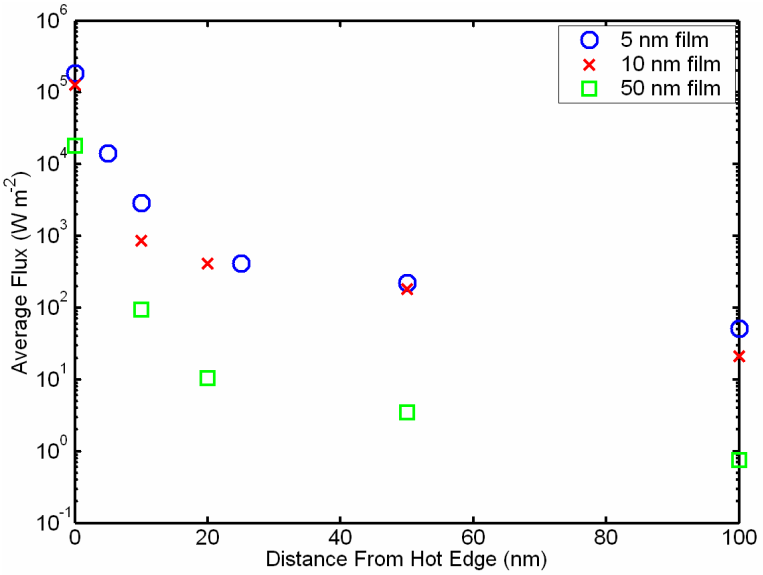

Figure 4.4 In-Plane Flux Inside Film as a Function of Distance from Heated Edge

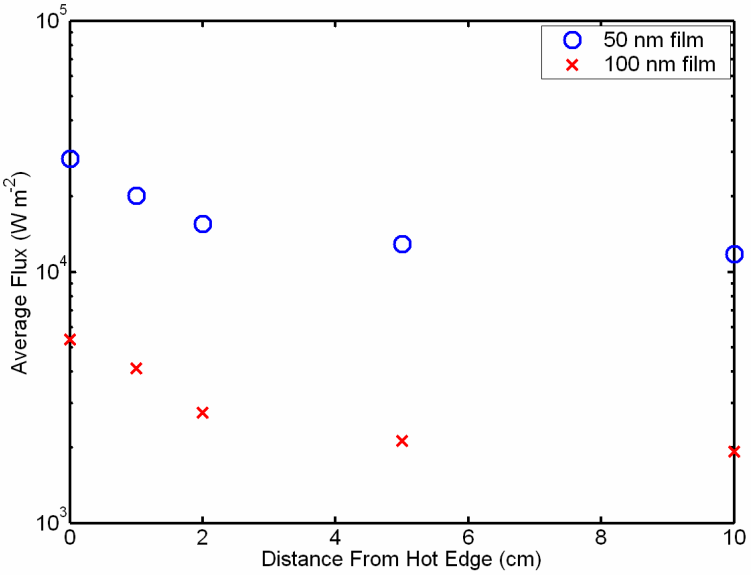

Figure 4.5 In-Plane Flux Outside Film as a Function of Distance from Heated Edge

Film Thickness (nm)	Λ inside film	Λ outside film
5	5 nm	-
10	2 nm	-
50	1 nm	25 cm
100	-	10 cm

Table 4.2 Extracted Propagation Lengths

The propagation lengths extracted from the fluctuational electrodynamics calculations compare reasonably well with the values from the complex thin film dispersion relations and Eqn. (2.12). From Figure 4.2 it is seen that inside the film the spectral flux peaks at about 10.4 μm. At this wavelength, the anti-symmetric mode of a 50 nm thick film has a propagation length less than 0.1 μm as shown in Figure 4.6. Outside the film, the spectral peak is around 12.6 μm where the anti-symmetric mode has a propagation length of around 10 to 100 cm.

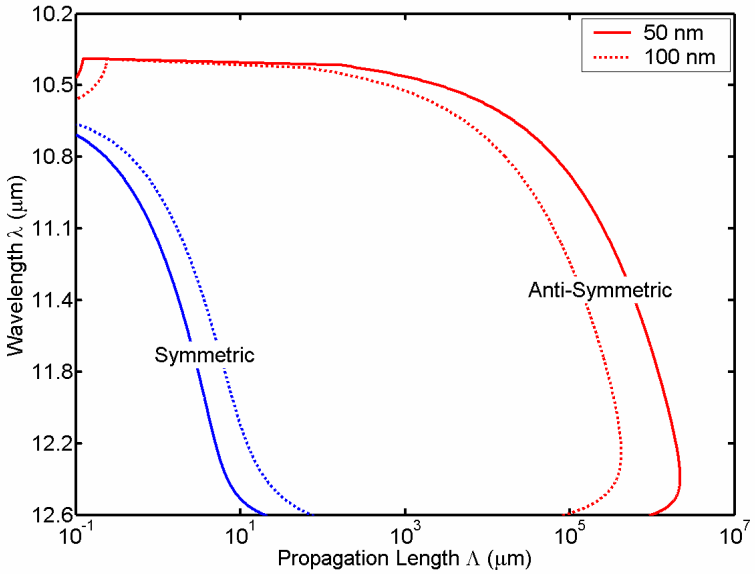

Figure 4.6 Propagation Lengths Calculated from Complex Dispersion Relations

4.6.3 Spectral Peak Location

The question then is why are the spectral peaks inside and outside the film at different wavelengths? Looking at Eqn. (4.7) it is seen that the spectral flux can be broken into a prefactor term times the actual quadruple integral. Figure 4.7 plots these two terms individually for inside a 50 nm film.

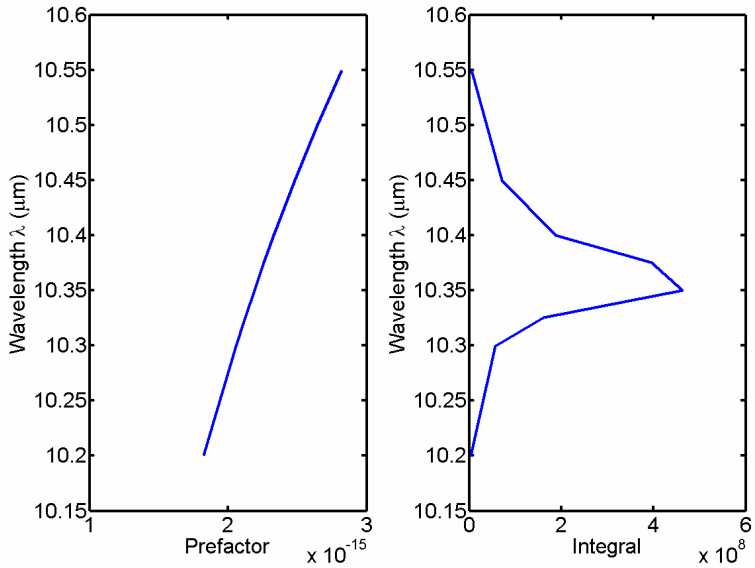

Figure 4.7 Prefactor and Integrand Inside Film

The prefactor term depends mainly on the product of ω^2 and the imaginary part of the dielectric function, ε. In this wavelength range the imaginary part of the dielectric function is basically constant, and so the prefactor varies only slightly. The integral, however, exhibits a peak that corresponds to where the anti-symmetric mode is flat, as shown in Figure 4.8. It appears that the integral has its peak value where the density of states is highest.

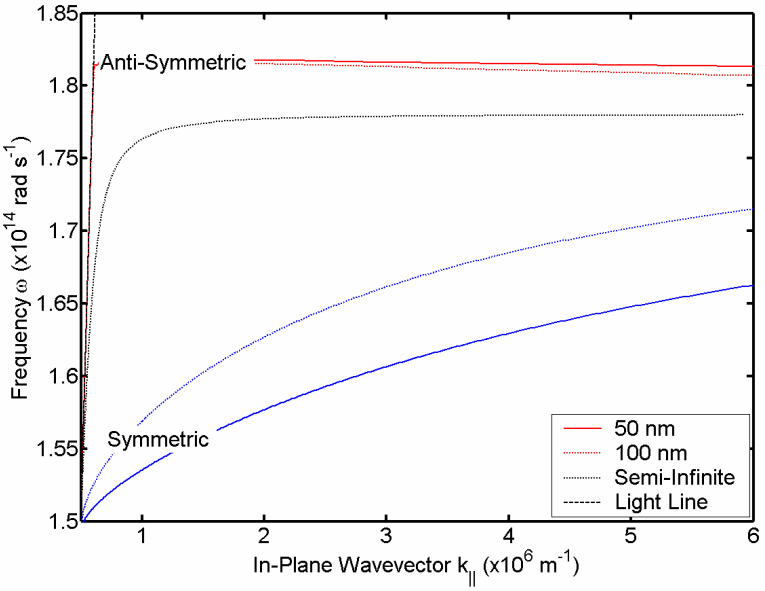

Figure 4.8 SiC Thin Film Dispersion Relations

Outside the film, the trend is different. Figure 4.9 shows that the integral exhibits some structure, but doesn't vary by more than a factor of two, which isn't enough to account for the peak shown in Figure 4.3. Instead, the dependence appears to be the result of variation in the prefactor, which peaks strongly at the frequency where the imaginary part of the silicon carbide dielectric function is largest, as shown in Figure 4.10.

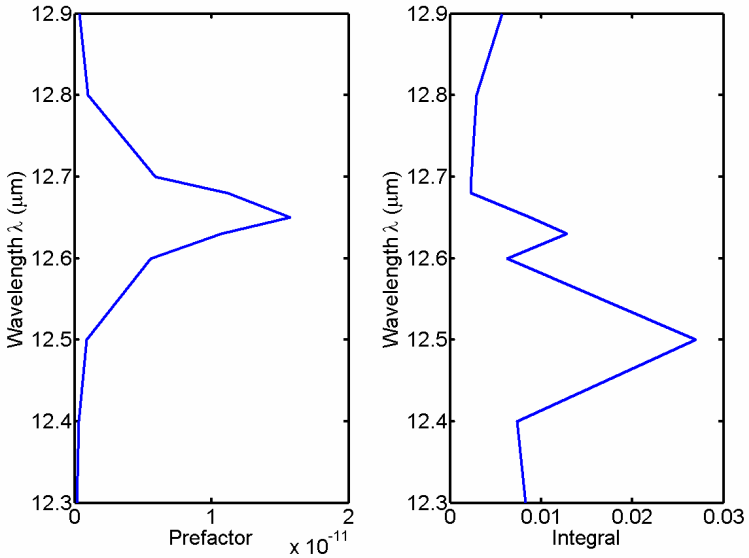

Figure 4.9 Prefactor and Integrand Outside Film

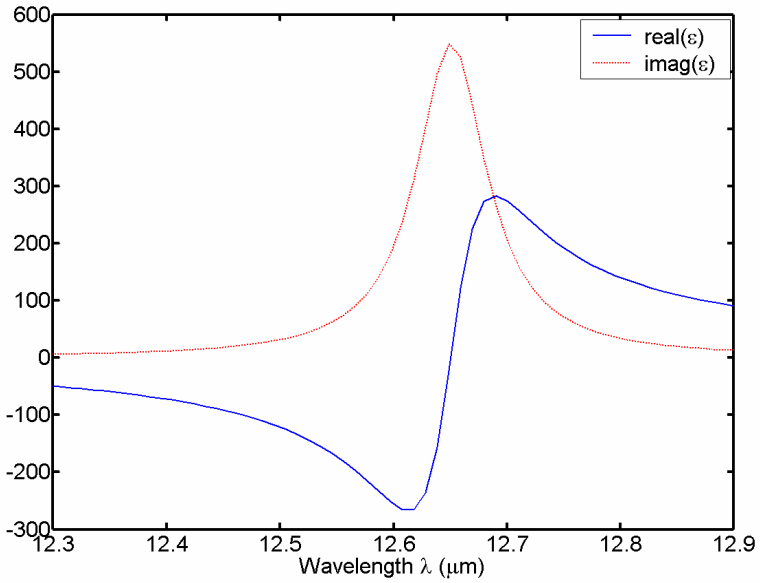

Figure 4.10 SiC Complex Dielectric Function

At first glance, this result is not intuitive, as large absorption should occur where the imaginary part of the dielectric function is large. However, most of the flux is in the anti-symmetric mode which mainly travels in the vacuum outside the film, where there is no damping. The peak in the prefactor essentially picks out a frequency in the regime where the anti-symmetric mode has a large group velocity, and its dispersion relation is very close to

the light line as shown in Figure 4.8. In this range, the density of states is fairly flat, and correspondingly the integral doesn't vary much. Due to the large group velocity, the propagation length is also large. The fact that the surface polariton dispersion relation is very close to the light line also indicates that the perpendicular component of the wavevector is very small. As a result, the corresponding penetration depth is quite large as was seen in the inset to Figure 4.3.

Finally, the overall in-plane flux as a function of film thickness from the fluctuational electrodynamics calculation is compared to the previous kinetic theory-based calculations [95] from Chapter 3. The results of the two calculations are plotted in Figure 4.11.

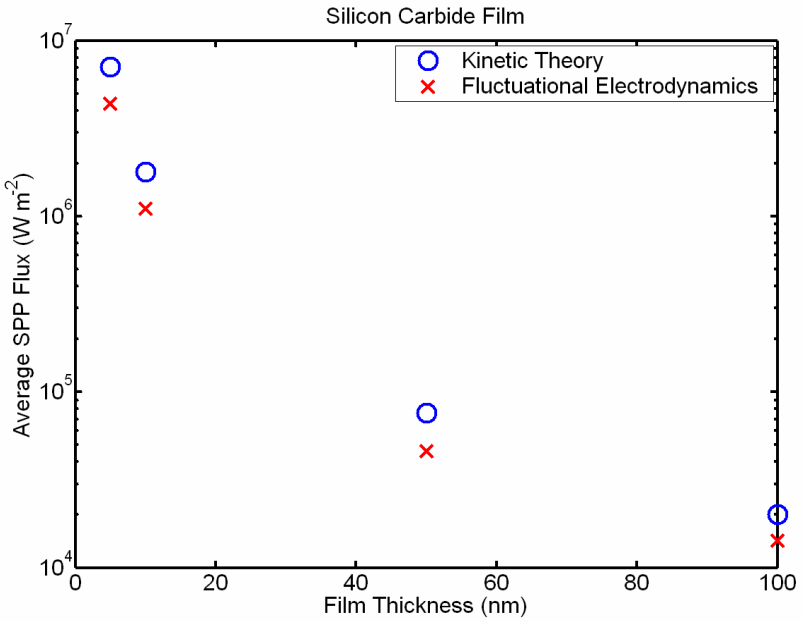

Figure 4.11 Fluctuational Electrodynamics and Kinetic Theory Comparison

Interestingly, in both approaches it is seen that thinner films actually transport more flux. As discussed above, this is due to the fact that the anti-symmetric mode of the thin film dispersion relation has a propagation length that increases as the film thickness decreases. As the film thickness increases beyond the critical point given by Eqn. (2.16), there is no longer

a splitting of the modes and the effect diminishes. The discrepancy between the two approaches is likely due to the error tolerance for the numerical integration and the finite integration of the limits in the fluctuational electrodynamics computation.

4.7 Conclusions

In this chapter a fluctuational electrodynamics calculation of the in-plane flux carried by surface phonon-polaritons on a thin film of silicon carbide was performed. Interestingly, it was found that thinner films carry more flux, and that it is primarily transported by the anti-symmetric thin film surface polariton. The calculations agree fairly well with previous calculations using a kinetic theory-based approach.

The discrepancy between the two approaches is likely due to the numerical integration where the contributions due to large wavevectors were truncated. Potential improvements would be to include these contributions and also to increase the error tolerance. However, the time required to do the computation with the code that was developed already approaches weeks to calculate one spatial point and frequency. To get results in a reasonable amount of time, more advanced techniques are needed. Two potential approaches include implementing CUBPACK [96], which is a FORTRAN 95 package for dealing with automatic integration over n-dimensions (cubature) using simplices and hyperrectangles, and DECUHR [97], which deals with integration of singular functions. Another line of attack may be to continue with the Monte Carlo approach but implement one of the quasi-random number sequences mentioned in Section 4.5.2.

Chapter 5

Propagation Length Measurement

From the work done in Chapter 3 and Chapter 4 it is clear that the key to the high thermal conductivity is the long propagation length of the surface polariton, particularly of the long-range anti-symmetric mode. Thus, measuring the propagation length of the surface polariton is the first experimental step to take. In this chapter, measurements using attenuated total reflection (ATR) and Fourier Transform Infra-Red (FTIR) spectroscopy are presented and discussed. Due to fabrication difficulties, only the single-interface surface polariton has been measured to date.

5.1 Measurement Approach

The surface phonon-polaritons of the amorphous phase of silicon dioxide (SiO_2) have not been studied due to the fact that it is not a crystalline material. However, there are still frequencies where the real part of the dielectric function is negative and surface phonon-polaritons are supported. One is around 9 μm (2.094×10^{14} rad s^{-1}) and the other is around 21 μm (8.976×10^{13} rad s^{-1}) [45]. Although the phonon resonance is relatively weak, oxide is a very commonly used material in micro-fabrication and as such its surface phonon-polariton modes are potentially of interest. As described in Section 2.5, there are three main ways to couple to surface polaritons. For NSOM measurements specialized equipment is required,

and the coupling efficiency by gratings can be low. Thus, a prism coupling approach was taken for these measurements.

5.1.1 Modified Otto Configuration

To measure propagation lengths with prism coupling, the natural choice is to use the Otto configuration described in Section 2.5.3. To accomplish this task, the configuration is slightly modified as shown in Figure 5.1. Two right-angle prisms are positioned over the surface of interest at some distance apart. The first prism is used to launch the surface wave, and the second is used to couple the surface mode out to a detector. By varying the distance between the two prisms, the attenuation of the surface polariton can be measured. This approach was taken by Schoenwald in 1973 [24] to measure the propagation length of the copper-air surface plasmon-polariton. At a wavelength of 10.6 μm, they measured the propagation length to be 1.6 cm.

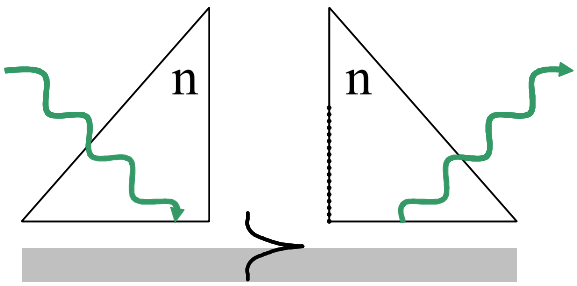

Figure 5.1 Double Prism Configuration for Propagation Length Measurement

The limitation with this approach is finding a laser source with the right frequency to excite the surface polariton. In particular, for silicon dioxide, there are no easily available sources at the appropriate resonance frequencies.

5.1.2 Attenuated Total Reflection

An alternative method of prism coupling is to use FTIR with ATR. It is experimentally easier to realize [98-103], but requires a little more analysis to extract the propagation length. In this arrangement, the evanescent wave from total internal reflection is used to provide the extra momentum required to couple propagating light to the surface polariton. Shown in Figure 5.2 are the layers and materials used. The interface of interest is separated from the zinc selenide (ZnSe) prism by an air gap of distance d, and the prism has an index of refraction greater than air. The light in the prism is incident on the prism-air interface at an angle greater than the critical angle so that it experiences total internal reflection. The evanescent wave at the prism-air interface can have sufficient momentum in the $\hat{x}-$direction so that at the appropriate frequency and air gap, it couples to the surface phonon-polariton at the air-SiO_2 interface. The reflected light is measured and is very close to unity for all frequencies except around the surface polariton resonance. At this frequency, there is a dip in the reflection as the evanescent wave couples to the surface polariton. The frequency of the dip can be determined from the intersection of the prism light line and the surface polariton dispersion relation as shown in Figure 5.3.

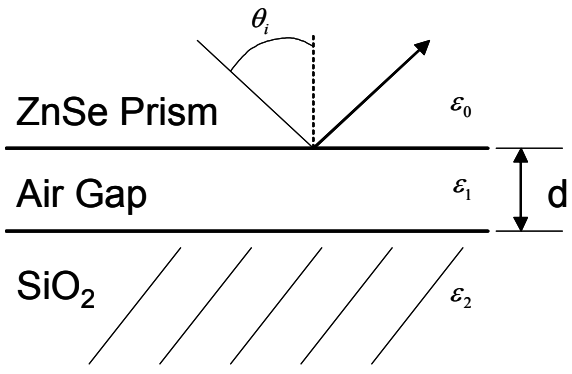

Figure 5.2 ATR Layer Geometry

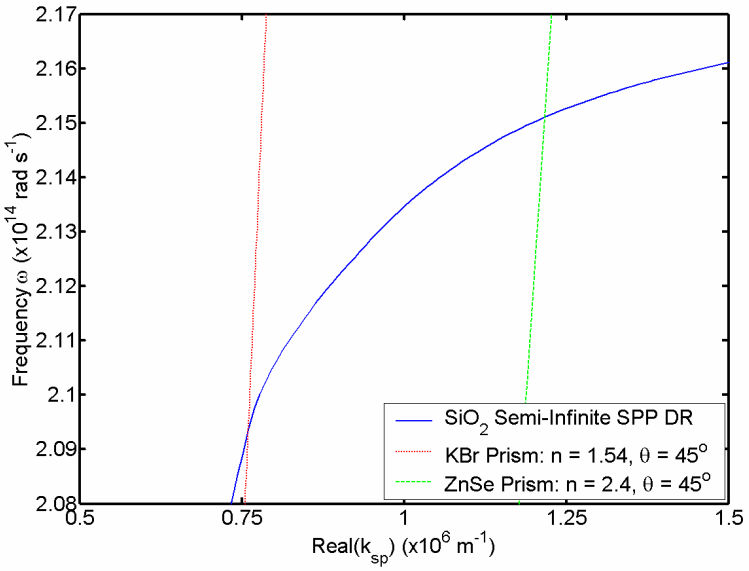

Figure 5.3 Surface Polariton Dispersion Relation and Prism Light Lines

5.2 Angle Scan vs. Frequency Scan

With the Otto configuration, there are two options regarding how the measurement is made. The frequency of the light can be held constant, and the incident angle can be scanned. This effectively varies the in-plane momentum, $k_x = \sqrt{\varepsilon_0}\frac{\omega}{c}\sin\theta_i$ where ε_0 is the dielectric constant of the prism. Alternatively, the other option is to hold the incident angle fixed and scan the frequency. This is the natural choice for ATR measurements using FTIR where the crystal geometry and angle of incidence are predetermined by the equipment.

5.3 Layered Media Reflection

The structure of Figure 5.2 is readily modeled using the standard reflection and transmission equations for layered media [51, 104]. For a simple three layer geometry, the reflectivity, $R = |r|^2$, and the reflection coefficient is given by

$$r = \frac{r_{01} + r_{12}\exp(2i\beta)}{1 + r_{01}r_{12}\exp(2i\beta)} \tag{5.1}$$

where $r_{lm} = (\varepsilon_m k_{zl} - \varepsilon_l k_{zm})/(\varepsilon_m k_{zl} + \varepsilon_l k_{zm})$ is the TM mode Fresnel reflection coefficient at the single interface between layers l and m, k_{zl} is the perpendicular component of the wavevector in layer l, and $\beta = k_{z1}d$ is the extinction coefficient in the air gap. For additional layers, recursion relations [51] and propagation matrices [51] are used to find the overall reflectivity or transmissivity.

Shown in Figure 5.4 are the calculated reflectivity spectra for a system of ZnSe/Air/SiO_2 layers with various air gap spacings. ZnSe has an index of refraction of 2.4, and the corresponding critical angle is θ_c = 24.6°. It is seen that there are two dips in the spectra which correspond to the two regions where the real part of the oxide dielectric function is negative.

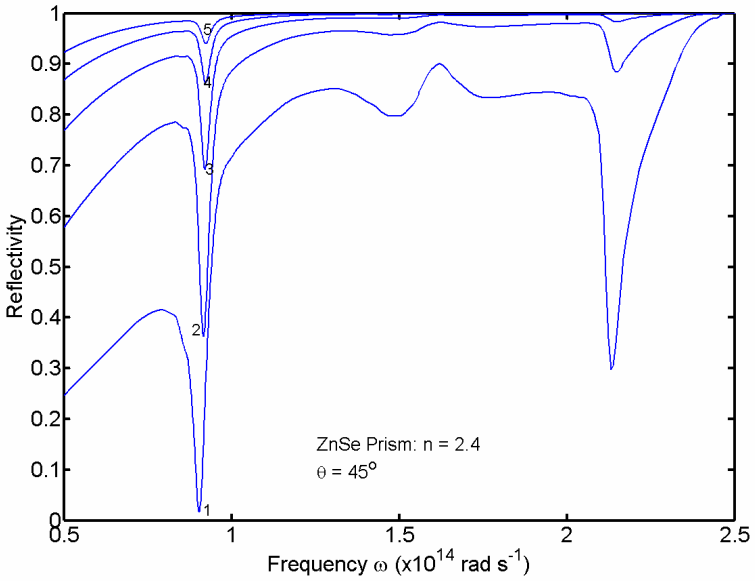

Figure 5.4 Calculated SiO_2 ATR Spectra

When complete coupling occurs, the reflectivity, as given by the modulus squared of Eqn. (5.1), goes to zero. Thus the optimum gap is given by

$$d = \mathrm{Re}\left\{ \frac{1}{2k_{z1}} \cos^{-1}\left(-\frac{\left(r_{01}^2 - r_{12}^2\right)}{2r_{01}r_{12}} \right) \right\}. \tag{5.2}$$

Using Eqn. (5.2), complete coupling is calculated to occur at 2.094×10^{14} rad s^{-1} with an air gap of 0.7 μm, and at 8.976×10^{13} rad s^{-1} with a gap of 0.95 μm. However, with air gaps less than 1 μm, there are practical concerns of trapping particles between the sample and prism surfaces, and thus a larger gap spacing is desirable. For the dip at 9 μm, it is seen that an air gap of one to two micron still produces a noticeable dip in the ATR reflectivity, and so a nominal 2 μm air gap was used.

5.3.1 Finite Film Thicknesses & Substrate

As indicated in Figure 5.5, the actual structure will consist of a finite thickness film on a substrate. This substrate underneath the film potentially affects the reflectivity due to penetration of the wave at the air-oxide interface into the substrate. To measure the single-interface surface polariton propagation length, the oxide layer needs to be thick enough to approximate an infinite half-space. The calculated effect of a silicon substrate on various film thicknesses of oxide is shown in Figure 5.6. The calculations show that an oxide film thickness of about 1 μm or greater will prevent perturbations by the second interface between the SiO_2 film and the silicon substrate. For film thicknesses below 0.5 μm there is a significant modification of the reflectivity. There is a shift of the peak dip frequency and an increase in reflectivity. Thus, the samples were fabricated with an oxide thickness of 1 μm.

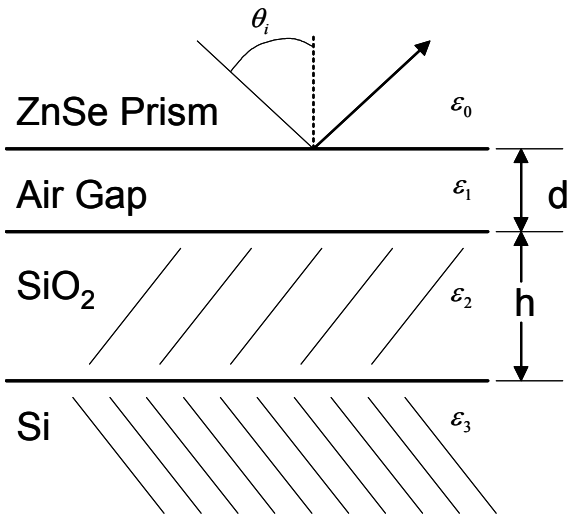

Figure 5.5 Actual ATR Geometry

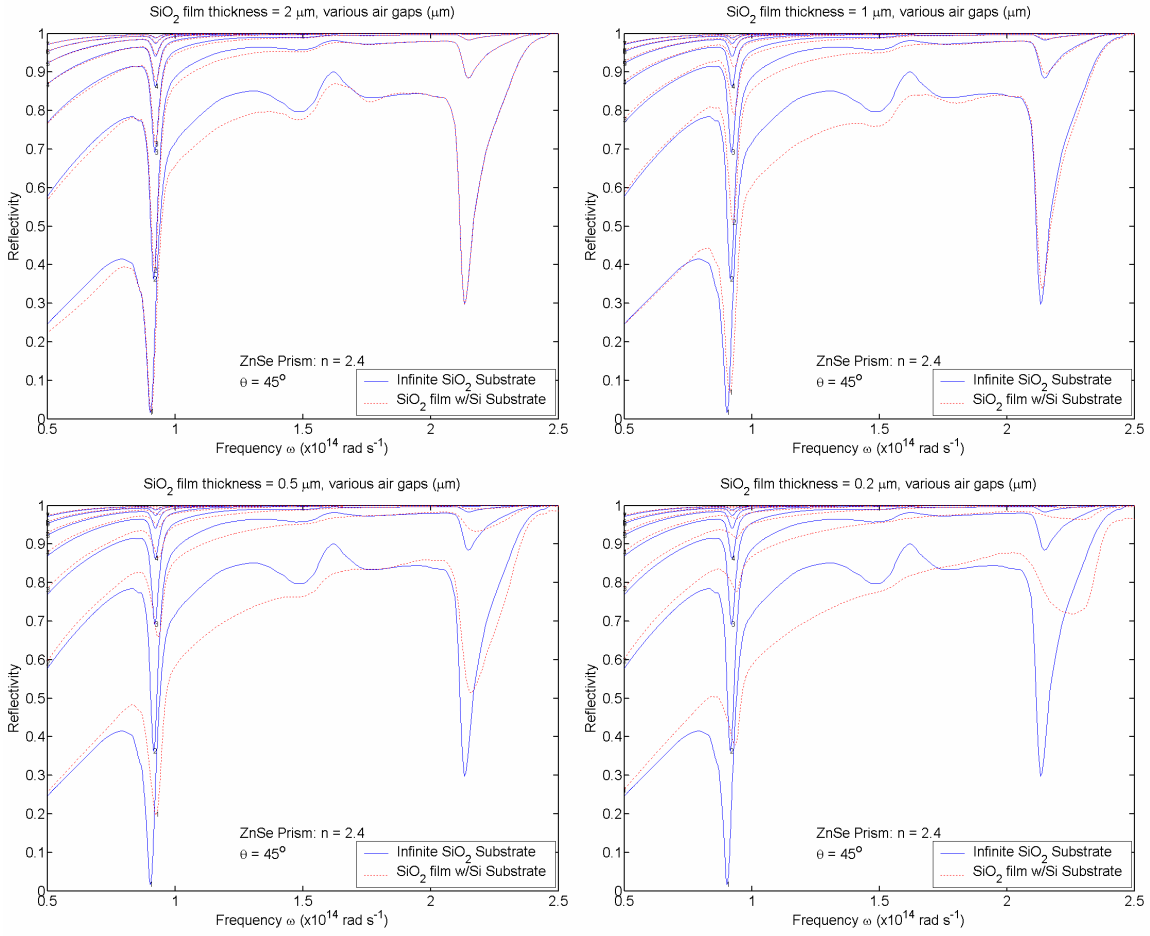

Figure 5.6 Effect of Finite SiO_2 Film Thickness and Si Substrate

5.3.2 Suspended Thin Films

As discussed in Section 2.4, for suspended films that support surface polaritons on both surfaces, the thin film surface polariton dispersion relations predict a splitting into a higher frequency anti-symmetric mode and a lower frequency symmetric mode. This splitting is also predicted in the ATR spectra as shown in Figure 5.7. However, due to compressive stress concerns, it is difficult in practice to realize a freely-suspended silicon dioxide membrane. Thus, these calculations were done for a suspended silicon carbide film and a potassium bromide (KBr) prism. KBr has an index of 1.54, which gives the prism light line a steeper slope than ZnSe. Thus, the intersection with the surface polariton dispersion relation occurs in a region where the group velocity is higher, and the resulting propagation length is longer. The intersection of the prism light line and SiC thin film dispersion relations is shown in Figure 5.8. It is seen that the intersection of the dispersion relations agree well with the locations of the dips in the ATR spectra.

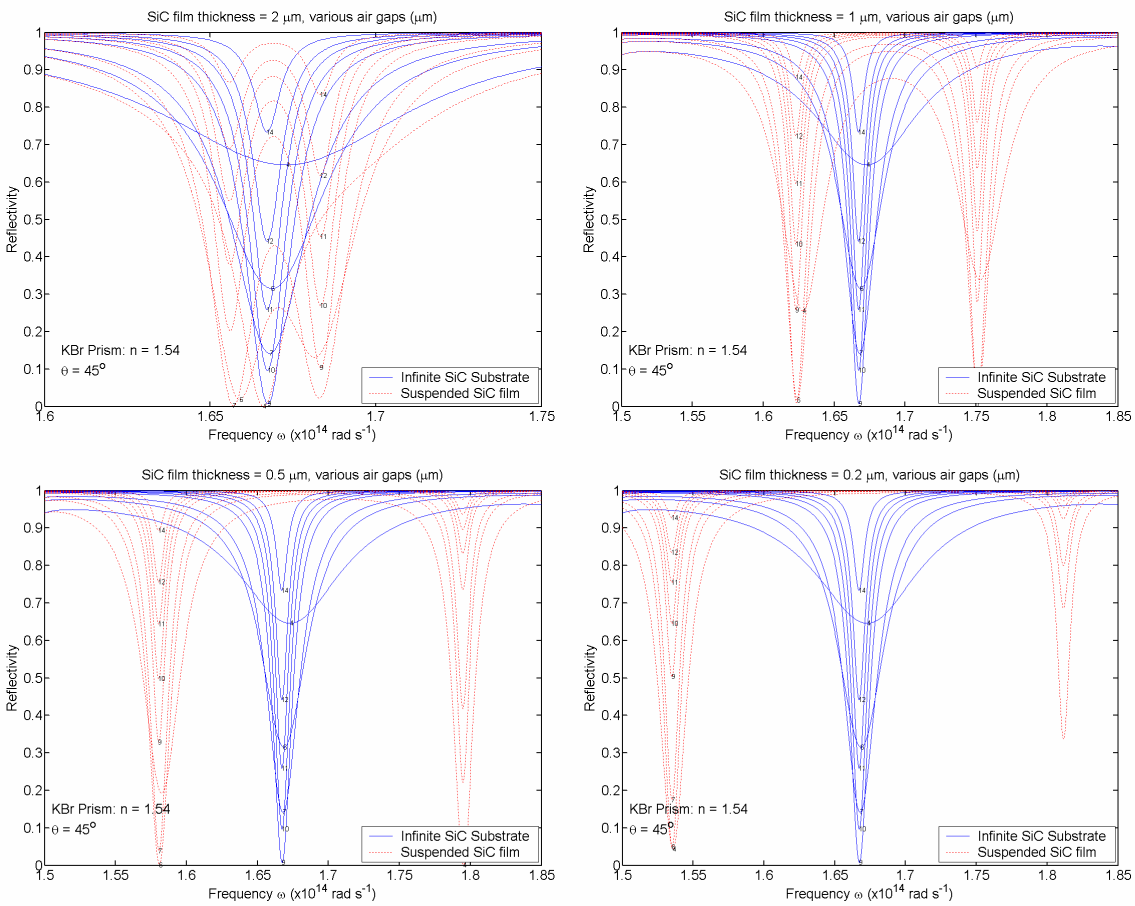

Figure 5.7 Effect of Film Thickness for Suspended SiC Films

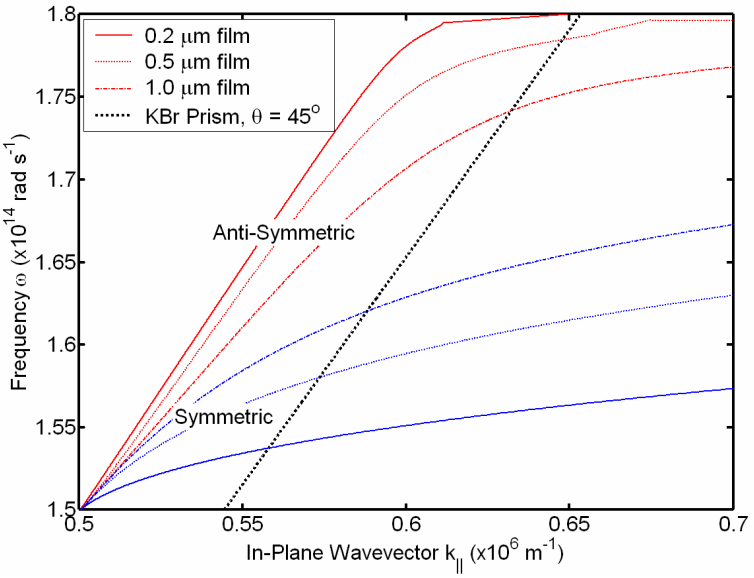

Figure 5.8 SiC Thin Film Dispersion Relation and KBr Prism Light Line

5.4 Sample Fabrication

5.4.1 Oxide Stress

As briefly mentioned in Section 5.3.2, one of the concerns with thermally grown oxide is that it is known to exhibit a residual stress that is on the order of 200 MPa compressive [105]. This compressive stress would cause a suspended membrane to wrinkle or crumple up, and would also cause a film deposited on a substrate to bend as illustrated in Figure 5.9.

Figure 5.9 Compressive Stress Film on Substrate

Figure 5.10 Tensile Stress Film on Substrate

The Stoney equation [106, 107] can be used to calculate the resulting curvature of the two layer system due to the film stress, and is given by

$$R = \frac{ET^2}{6\sigma(1-\nu)t} \tag{5.3}$$

where R is the radius of curvature, σ is the film stress, E is the Young's modulus of the substrate, T is the substrate thickness, ν is the substrate Poisson's ratio, and t is the film thickness. Eqn. (5.3) is valid when $t/T < 0.01$.

For one micron of thermal oxide on a 550 μm thick silicon wafer, the resulting wafer bow is calculated to be approximately -62 μm for a 150 mm diameter silicon wafer with a

biaxial Young's modulus of $180x10^9$ Pa. This bow was confirmed by measuring six wafers with a Tencor FLX-2320 Thin Film Stress Measurement system. The system uses laser interferometry to determine the wafer curvature before and after the deposition of the film. To determine the film stress, the oxide layer thickness was needed as an input, and was separately measured using a KLA-Tencor UV 1280 spectroscopic ellipsometer. The resulting measurements are listed in Table 5.1 and the stress for the six samples is plotted in Figure 5.11. Each wafer was measured twice in orthogonal directions. The bow was measured to be between -56 and -66 μm for the six different samples, in good agreement with the prediction using the Stoney equation. However, with this level of curvature, even across a smaller 2 inch sample, the resulting bow is about -7 μm which would still prevent the desired one to two micron gap for the Otto configuration.

Wafer	Orientation	Film thickness (Å)	Bow (μm)	Stress (MPa)
1	horizontal	10357	-57.73	-242
2	horizontal	10308	-56.18	-233
3	horizontal	10356	-66.52	-267
4	horizontal	10340	-60.49	-242
5	horizontal	10350	-64.87	-259
6	horizontal	10343	-56.61	-234
1	vertical	10357	-60.47	-258
2	vertical	10308	-62.46	-253
3	vertical	10356	-63.45	-255
4	vertical	10340	-61.37	-248
5	vertical	10350	-62.77	-253
6	vertical	10343	-60.16	-249

Table 5.1 Measured Thermal Oxide Wafer Bow & Stress

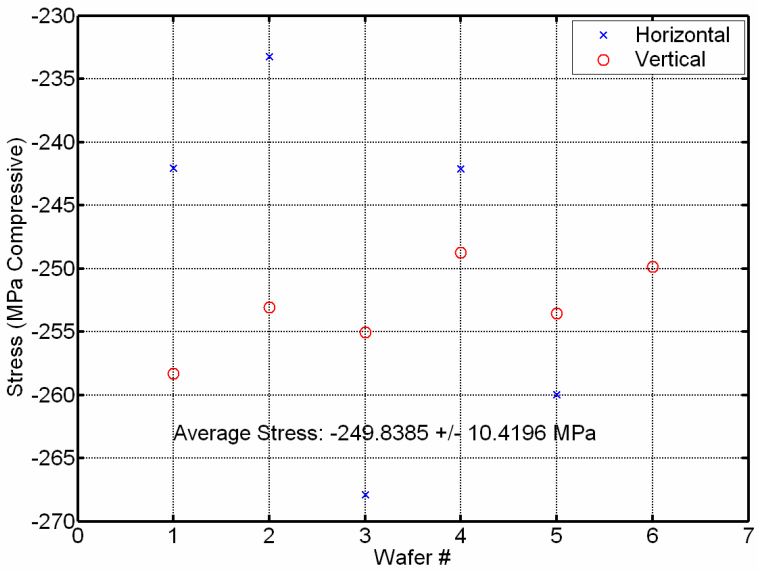

Figure 5.11 Measured Thermal Oxide Stress

To overcome this problem, a plasma-enhanced chemical vapor deposition (PECVD) recipe was developed for a low-stress oxide. Tetraethylorthosilicate-based (TEOS) oxide was deposited using a Novellus Concept One system. The deposition was done at a temperature of 350 °C at a nominal rate of 0.25 μm/min. Motivated by the work of Zhang [108, 109], the percentage of low-frequency RF power was varied for each deposition while the total power was held constant. It was found that the resulting residual stress of the deposited oxide could be controlled from compressive to tensile as the percentage of low-frequency RF power was decreased as shown in Table 5.2 and Figure 5.12. The most neutral stress is achieved with 40% low-frequency RF power, and this was the recipe used for making the samples. This wafer was cut into 2 inch square samples using a diesaw.

% Low-Frequency RF	Orientation	Film thickness (Å)	Bow (μm)	Stress (MPa)
50	horizontal	9913	-26.06	-70.1
40	horizontal	10236	-0.76	-2.0
30	horizontal	10389	40.87	104.9
20	horizontal	10526	40.62	102.9
25	horizontal	10432	54.38	139
35	horizontal	10274	23.58	61.2
50	vertical	9913	-72.49	-195
40	vertical	10236	-6.53	-17.0
30	vertical	10389	14.92	38.3
20	vertical	10526	30.04	76.1
25	vertical	10432	25.12	64.2
35	vertical	10274	4.28	11.1

Table 5.2 Measured PECVD TEOS Oxide Wafer Bow & Stress

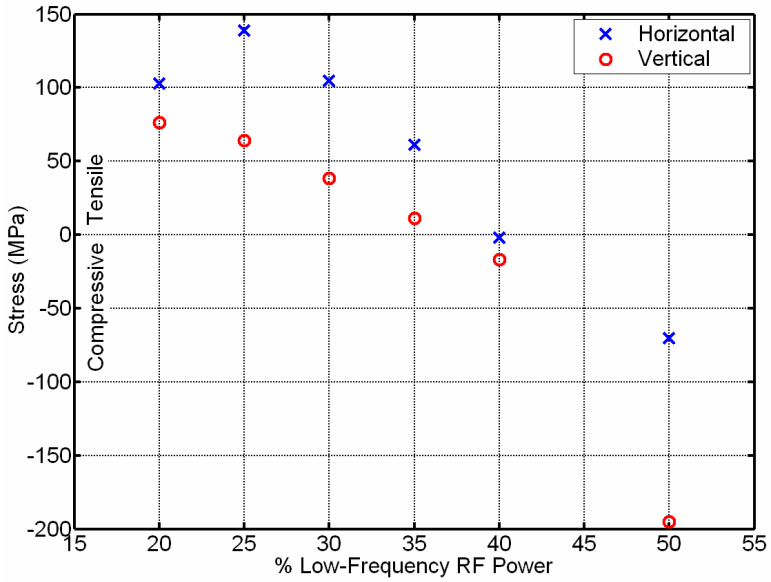

Figure 5.12 PECVD TEOS Oxide Stress

It is also observed from Figure 5.12 that the PECVD stress measurements made across the wafer in the horizontal direction are systematically higher than those in the vertical direction (although the one vertical measurement made at 50% low-frequency RF

power appears a statistical outlier). The physical difference between the two measurement directions is the presence of the wafer flat which reduces the effective vertical dimension. However, this trend is not observed in the stress measurements of the thermal oxide in Figure 5.11, and so the difference in measured stress can not be attributed to the wafer flat. Rather, it is likely that there is some non-uniformity in the deposition chamber which leads to an anisotropic film thickness or stress during the deposition. Each wafer is rotated through five different locations during each deposition and may be preferentially exposed to the plasma, leading to the observed difference between the horizontally and vertically measured stresses.

5.4.2 Photoresist Spacer

The other experimental difficulty is in specifying and controlling the air gap. The desired $2\,\mu m$ air gap was realized by using dots of photoresist as spacers. A small amount of photoresist was placed at the edges of the chip which was then spun at 2000 rpm for 30 seconds to achieve the desired thickness. A 95° C, one hour hard bake was performed to drive off residual solvents and harden the resist.

5.5 Measurements

Measurements were made using a Thermo-Nicolet Magna-IR 860 Spectrometer set up with a liquid nitrogen-cooled mercury cadmium telluride detector, and a KBr beam splitter. The detector has a resolution of 4 cm^{-1} and a spectral range of 650 cm^{-1} to 4000 cm^{-1}. As a result only the surface phonon-polariton at $9\,\mu m$ could be studied. A ZnSe wire grid polarizer was used to set the polarization of the incident light, and 128 scans were used to collect the data. A horizontal ATR accessory with a 50 mm x 10 mm x 2 mm 45° single pass trapezoid ZnSe crystal allowed for multiple reflections of the beam to interact with the sample. Slight

pressure was applied on the sample with a small clamp and thumb screw to ensure good contact between the photoresist spacers and the crystal surface. Excessive pressure was avoided as it would cause the ATR crystal to break.

The measured ATR spectra are shown in Figure 5.13. Both the TE and the TM modes were measured separately, and as expected only the reflectivity spectrum of the TM mode exhibits coupling to the surface mode. The wavelength of the dip is found to be at $8.72\,\mu m$, in good agreement with the prediction of 8.76 μm from the intersection of the prism and surface polariton dispersion relations shown in Figure 5.3. Also plotted in the figure is the calculated reflectivity for a 1 μm thick SiO_2 film on a silicon substrate, separated from the prism by a 2 μm air gap. It is seen that the measured data is blue-shifted by about 50 nm and that the magnitude has an offset of 0.008. As seen from Figure 5.4, the dip in reflectivity is strongly dependent on the air gap. In fact, the dependence is exponential as was shown above in Eqn. (5.1). Repeating the calculation with a reduced air gap of $1.9\,\mu m$ shifts the position of the dip in reflectivity and provides a much better fit to the data. Given the details of the experimental apparatus, a 100 nm variation in air gap spacing is not unreasonable.

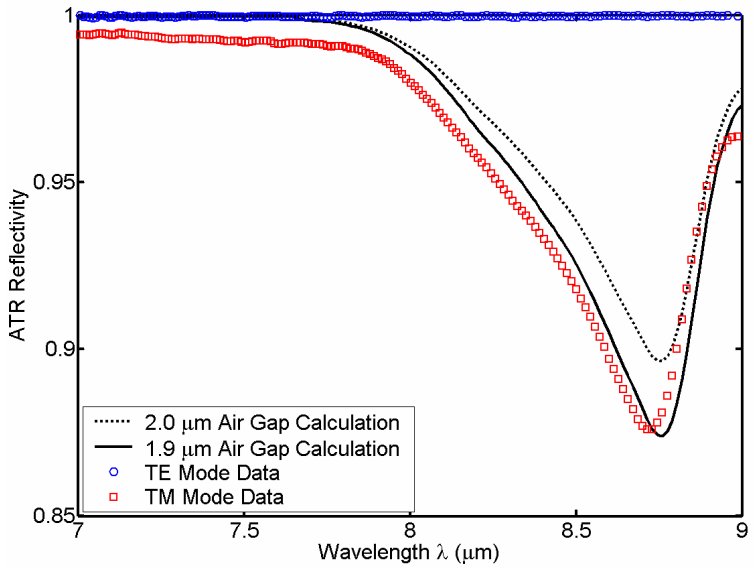

Figure 5.13 Measured and Calculated ATR Spectra with ZnSe Prism

A measurement was also made using a potassium bromide (KBr) prism and is shown in Figure 5.14. The KBr light line intersects the dispersion relation at a steeper portion of the curve as was shown in Figure 5.3. As a result, the corresponding propagation length is longer. For this measurement, the gap was nominally 10 μm, and was obtained by using thick photoresist to create the spacers.

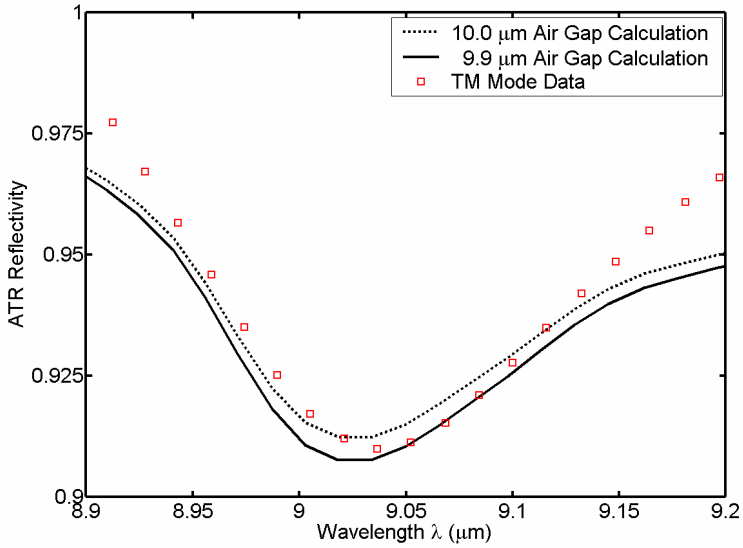

Figure 5.14 Measured and Calculated ATR Spectra with KBr Prism

To extrapolate the propagation length from the measured ATR spectra we start with the expression for the multi-layer reflectivity, Eqn. (5.1) and algebraically manipulate it to explicitly include the surface polariton wavevector, $k_{sp} = (\omega/c)\sqrt{\varepsilon_1\varepsilon_2/\varepsilon_1+\varepsilon_2}$. Thus, at each frequency,

$$R(k_{sp}) = \left| \frac{r_{01} + \dfrac{(\varepsilon_2 k_{z1} - \varepsilon_1 k_{z2})^2 / (\varepsilon_1^2 - \varepsilon_2^2)}{k_x^2 - k_{sp}^2} e^{2i\beta}}{1 + r_{01} \dfrac{(\varepsilon_2 k_{z1} - \varepsilon_1 k_{z2})^2 / (\varepsilon_1^2 - \varepsilon_2^2)}{k_x^2 - k_{sp}^2} e^{2i\beta}} \right|^2 \tag{5.4}$$

A MATLAB zero finding routine, FZERO, was then used to find the value of the complex surface polariton wavevector that gives the best fit to the ATR data. Averaging over the range of frequencies where data was taken, it was found that the surface phonon-polariton propagation length is $10.8 \pm 1.3 \mu m$ at 8.72 μm, and $13.4 \pm 1.4 \mu m$ at 9.03 μm.

The calculated value of the oxide surface polariton propagation length is shown in Figure 5.15. It is seen that at 8.72 μm the corresponding propagation length has a value of nine micron which is in good agreement with the value extracted from the ATR measurement. Similarly, at 9.03 μm, the calculated propagation length of 16 μm is in fair agreement with the extracted value.

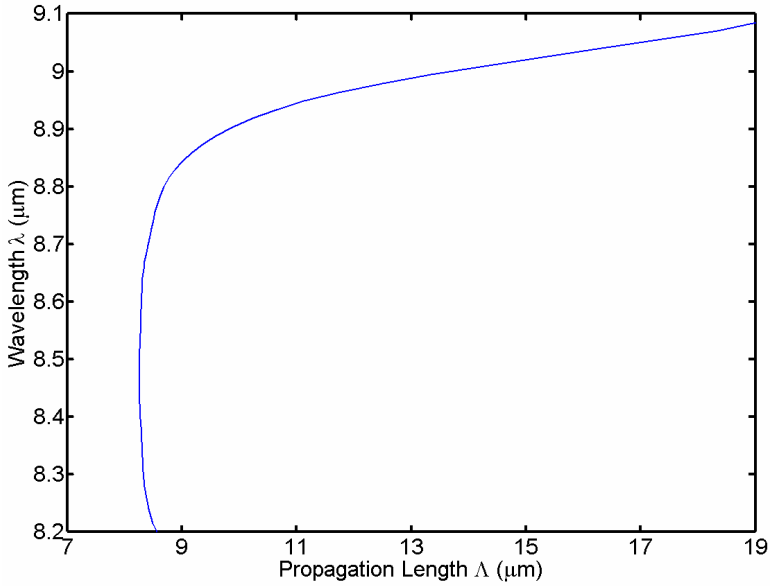

Figure 5.15 Calculated Propagation Length of SiO_2 Surface Phonon-Polariton

For reference, the calculated propagation lengths for various surface phonon-polaritons on silicon carbide and amorphous silicon dioxide are listed in Table 5.3 and Table 5.4. The propagation lengths are a function of frequency, so for illustrative purposes only the maximum calculated value is listed. For thin films this will occur for the anti-symmetric mode, and for silicon dioxide, it is the stronger dielectric function resonance at 9 μm that is listed.

Surface Polariton Type	Film Thickness	Maximum Propagation Length
Single Interface	-	700 μm
Thin Film	1 μm	845 μm
Thin Film	500 nm	4.7 mm
Thin Film	200 nm	54 mm
Thin Film	100 nm	31 cm
Thin Film	50 nm	1.6 m
Thin Film	10 nm	56 m

Table 5.3 Calculated SiC Propagation Lengths

Surface Polariton Type	Film Thickness	Maximum Propagation Length
Single Interface	-	35 μm
Thin Film	1 μm	42 μm
Thin Film	500 nm	187 μm
Thin Film	200 nm	1.4 mm
Thin Film	100 nm	5.7 mm
Thin Film	50 nm	23 mm

Table 5.4 Calculated SiO_2Propagation Lengths

5.6 Conclusions

An experimental measurement of the propagation length of the single-interface surface phonon-polariton on amorphous silicon dioxide was made. The propagation length was extracted from the spectral reflectivity which was measured by attenuated total reflection. It was found that the experimentally measured propagation length of 10.8 μm agreed well with the value calculated from the complex in-plane wavevector and tabulated values of the dielectric function.

The limitation of the ATR method used is that it only picks out one point on the dispersion relation. The ability to vary the incident angle would be ideal to map out the full

dispersion. Furthermore, it is the anti-symmetric mode of suspended films that has the greatest propagation length. Unfortunately, it was not possible to measure suspended samples due to fabrication difficulty, although some process development was started. It should also be noted that given some of the extremely large surface polariton propagation lengths, the actual effective mean free path will be set by the sample dimensions, so that the surface polariton transport is actually ballistic.

Chapter 6

Extraordinary Optical Transmission

In this chapter, the focus is turned away from energy transport along the in-plane direction of a thin film, and is now focused on transmission in the perpendicular direction, or through the film. Specifically, experimental measurements are presented of the transmission through an amorphous silicon dioxide film that has been perforated by sub-wavelength holes. The data agree very well with simulations performed in conjunction with Rafif Hamam of Prof. Marin Soljačić's group.

6.1 Introduction

As briefly discussed in Section 1.2, the possible explanations for extraordinary optical transmission (EOT) suggest that the effect should be observed in materials with a negative dielectric function [32]. Metals can support surface plasmons, and for dielectrics the analogue are surface phonon-polaritons. The surface plasmon range extends from $\omega_p / \sqrt{1+\varepsilon_d}$ down to zero frequency, where ε_d is the dielectric constant of the surrounding medium. However, the surface phonon-polariton resonance only occurs over a finite frequency range which is defined roughly between the transverse optical and longitudinal optical phonon frequencies. With the exception of one measurement on silicon carbide [43],

all of the experimental EOT measurements to date have been of metal films. Although amorphous silicon dioxide has a weak dielectric resonance, the measurements and calculations in this chapter demonstrate that EOT also occurs through a perforated dielectric film.

6.2 Sample Fabrication

Shown in Figure 6.1 are the dimensions and geometry of the samples fabricated and measured. The film of thickness t resides on a substrate. The circular holes have a diameter d and are arranged in a square lattice with periodicity a_0. The diameter of the holes is specified to be less than half the wavelength of the incident light so that no propagating guided modes are supported.

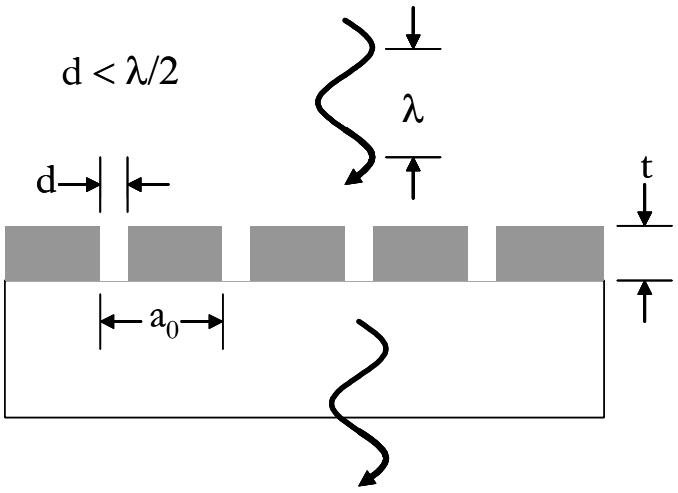

Figure 6.1 EOT Sample Geometry and Dimensions

The fabrication of the samples was very straightforward and accomplished via standard micro-fabrication techniques. Schematic cross-sections of the process are shown in Figure 6.2. The substrates consisted of silicon wafers obtained from Silicon Quest International. The wafers were double side polished, 500 μm thick, p-type, <100> wafers

with 1-10 Ω-cm resistivity. The first step was to grow one micron of thermal oxide on the silicon wafers using a wet recipe. Pattern transfer was achieved using direct contact photolithography using positive resist. The chrome on soda lime glass mask was made by Advance Reproductions and pen plots are reproduced in Appendix C. A buffered oxide etch was used to simultaneously etch the desired pattern and remove the backside oxide, and a final oxygen plasma was used to ash the photoresist.

6" DSP <100> wafer
500 μm +/- 5 μm

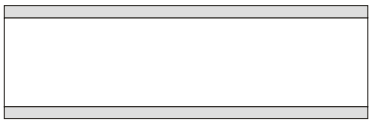

Grow 1 μm thermal oxide

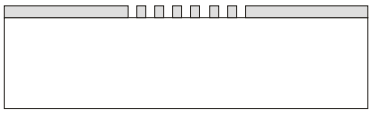

[FRONTSIDE] photo

BOE oxide

Ash resist

Figure 6.2 Process Flow

One practical concern regarding the pattern generation of the mask was the number of drawing elements. The desired patterns consisted of a square lattice of circular holes covering an area of 12 mm by 12 mm. The lattice constant of the hole arrays was 4 μm and 8 μm, and the diameter of the holes was 2 μm. A quick calculation shows that this would result in 2 to 9 million circles for each sample. With 12 samples per wafer, this becomes an unwieldy number of elements for the drawing software and mask pattern generation. A solution is to instead layout the reversed image as illustrated in Figure 6.3. Instead of scaling

by n^2 where n is the number of rows and columns of elements, the number of elements of the reversed image scales as $2n$. Thus, instead of 9 million circles, there are only approximately 6,000 rectangles for each sample which is a significant savings in element count. However, the drawback is that instead of circles, squares result.

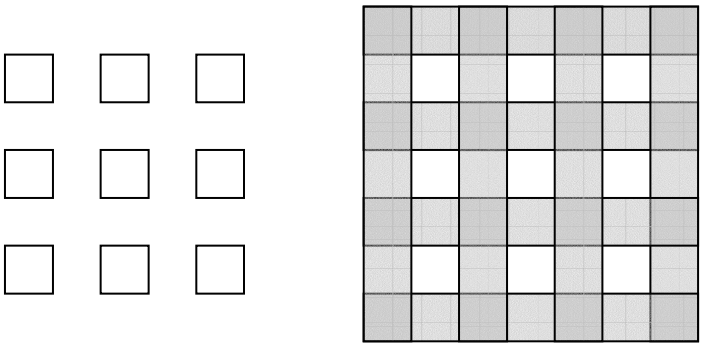

Figure 6.3 Mask Pattern Scaling

Fortuitously, the mask maker had some issues with the reproduction fidelity of the 2 micron linewidths, and the resulting squares actually appeared as circles on the mask. A scanning electron micrograph (SEM) image of the actual etched holes in silicon dioxide is shown in Figure 6.4.

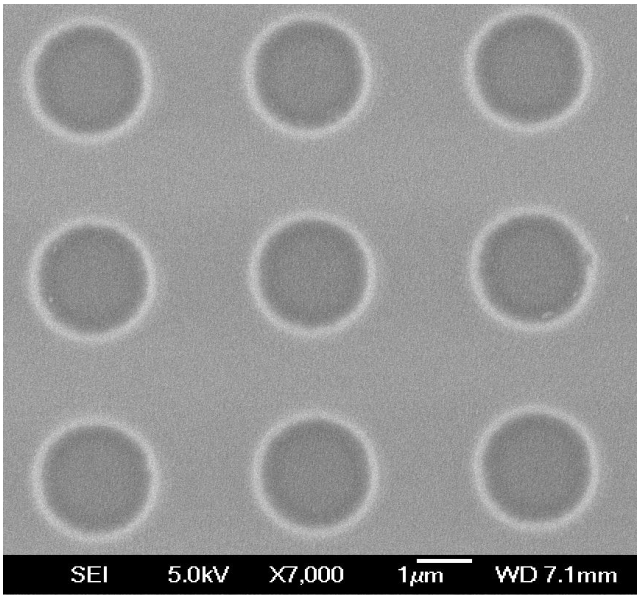

Figure 6.4 SEM of Etched Holes (courtesy of C. T. Harris)

6.3 Experimental Measurements

Similar to the propagation length measurements of Chapter 5, the infra-red transmission spectra of the samples were measured using FTIR spectroscopy. This time the Thermo-Nicolet Magna-IR 860 Spectrometer was set up with a DTGS/KBr detector, and a KBr beam splitter. This detector has a spectral range of 400 cm^{-1} to 4000 cm^{-1} with a resolution of 4 cm^{-1}. Transmission spectra were obtained for normal incidence, and an aperture was used to produce a spot size of approximately 8.75 mm in diameter on the sample.

6.3.1 Solid Film

Shown in Figure 6.5 are the measured and the analytically calculated transmission through a 1 μm thick, non-perforated film of SiO_2 on a 500 μm thick silicon wafer. First, the transmission through and reflection from the SiO_2 film alone were calculated using a wave optics formulation. The film was modeled as a thin homogeneous dielectric sandwiched between two infinite half spaces of vacuum ($\varepsilon = 1$) and silicon ($\varepsilon = 11.7$), resulting in the transmissivity, $T_{film}(\omega)$, and reflectivity, $R_{film}(\omega)$, of the film alone [104]. On the other side of the silicon wafer next to air, Fresnel coefficients were used to calculate the corresponding quantities, $T_{back}(\omega)$ and $R_{back}(\omega)$.The inset to Figure 6.5 shows a side view of the light path through the sample and the definition of the transmissivities and reflectivities. Ray tracing of the intensity through the substrate is then used to calculate the transmission through the entire structure [45].

In addition, absorption in the silicon wafer, $A_{silicon}(\omega) = \exp(-4\pi\kappa d/\lambda)$ where κ is the imaginary part of the complex index of refraction, d is the thickness of the wafer, and λ

is the wavelength, was significant due to the large thickness and was also included. Thus, the overall transmission is given by

$$T_{overall}(\omega) = \frac{T_{film}(\omega) T_{back}(\omega)}{1 - R_{film}(\omega) R_{back}(\omega)} A_{silicon}(\omega), \tag{6.1}$$

where all quantities are frequency dependent. The optical constants for SiO_2 and silicon used in these calculations were taken from published values [45].

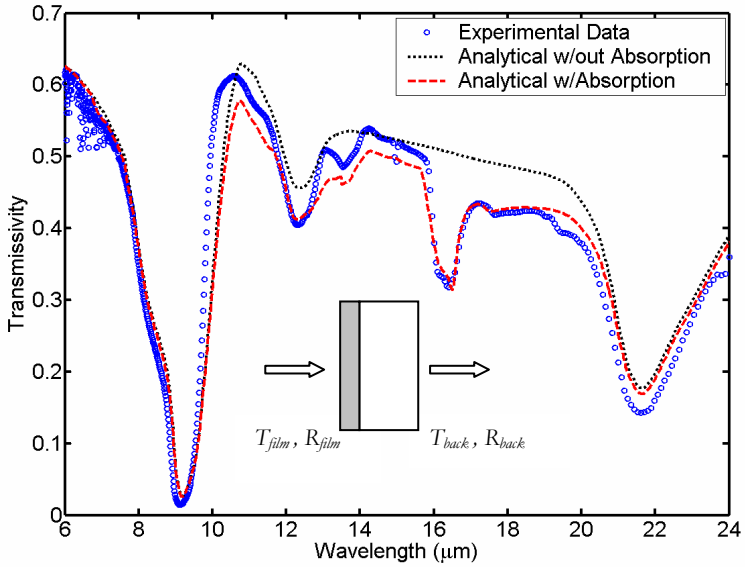

Figure 6.5 Measured and Calculated Transmission Through a Solid Film

Overall, there is very good agreement between the analytically calculated and measured transmission spectra. It is also seen that the effect of absorption in the silicon substrate is quite important in matching the experimental data. In particular, at 16 μm the effect of the silicon transverse optical phonon is quite important. Overall, the gross features of the spectrum are clearly reproduced, as is much of the small scale structure. The small discrepancy between the measured and analytically calculated spectra is likely due to the fact that the actual optical constants depend on the doping level of the silicon [110, 111].

6.3.2 Perforated Films

Next, measurements were made of the oxide films with holes etched through them. Plotted in Figure 6.6 is the measured transmission spectra of a perforated SiO_2 film normalized to the transmission through a solid film. Thus, a value greater than unity indicates that the transmission through the perforated film is more than that through the solid film. In the range of wavelengths from 6 μm to 24 μm, the 2 μm holes are clearly below the cutoff wavelength and do not support any propagating modes. Thus, for most of the range the transmission ratio is unity as is expected. Nevertheless, it is observed that the perforated film has significantly greater transmission in two regions: one around 9 μm and the other around 21 μm. Furthermore, these two wavelength ranges correspond exactly to where the real part of the silicon dioxide dielectric function is negative.

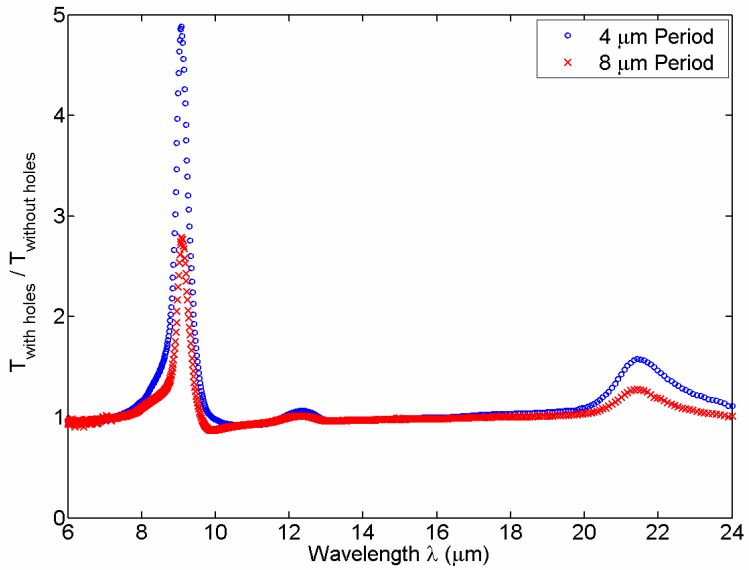

Figure 6.6 Measured Transmission Through Perforated Oxide Films

The question then is whether or not surface phonon-polaritons are supported at these wavelengths. The frequency range where surface phonon-polaritons exist is roughly

bounded by the transverse optical and longitudinal optical phonon frequencies of each resonance. However, as discussed in Section 2.3.2, the highly damped nature of the SiO_2 phonon resonances indicate that the complex plot of the real and imaginary parts of the wavevector needs to be examined to determine whether or not there is a mode trapped on the surface. Although the dispersion relation will be modified by the array of holes, it has been noted that the effect will be to lower the frequency of the existing modes [40], and the magnitude of such red-shifts have been observed to be on the order of 10 to 100 nm [112, 113]. As such, we consider the usual dispersion relation at a smooth interface for simplicity.

Shown in Figure 6.7 is a complex plot of the wavevector which has been normalized to the light line in vacuum. It is seen that there are two frequency ranges (8.6 – 9.3 μm and 20.2 – 21.6 μm) where the real part of the wavevector is greater than the light line. Hence, these modes are non-radiating. Furthermore, there are portions of these ranges where the imaginary part of the wavevector is small (less than a tenth of the real part), which indicates that the damping is low. As discussed in Section 2.3.2, together these two characteristics indicate the existence of surface modes. Also plotted in the figure are the wavelengths where the peak EOT occurs, at 9.1 μm and 21.4 μm. It is seen that these wavelengths clearly fall in the range of these surface phonon-polaritons.

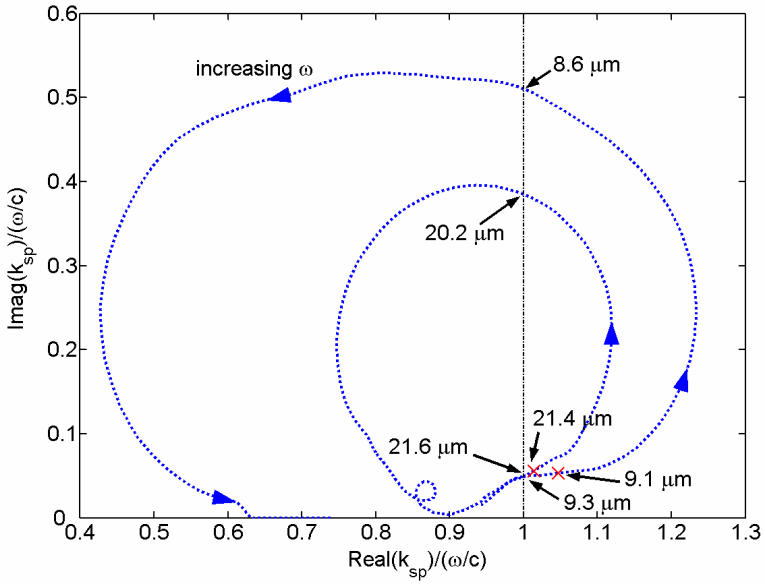

Figure 6.7 Complex Plot of the SiO_2 Surface Phonon-Polariton Wavevector

It could be argued that the transmission enhancement is due to a reduction in the effective refractive index of the film caused by the holes. However, this mechanism would increase transmission over the entire spectrum, which is clearly not the case. Rather, the fact that EOT is only observed at the frequencies where surface phonon-polaritons exist, strongly points towards their involvement in the transmission. Coupling of the normally incident light to the surface modes on the air-SiO_2 interface is via the grating momentum provided by the hole array [112]. After some type of resonant interaction in the perforated film, the lack of a surface mode at the SiO_2-silicon interface then allows for the resonant mode to couple directly back into a propagating wave in the silicon substrate.

6.4 FDTD Simulations

Numerical simulations were performed in collaboration with Rafif Hamam of Prof. Marin Soljačić's group using a finite-difference time-domain (FDTD) algorithim [114]. Apart from discretization, these simulations model Maxwell's equations in 3D exactly, taking into

account both material dispersion and absorption. As shown in Figure 6.8, the computational cell had dimensions of $a \times a \times 250$ grid points (GP), where a is the lattice constant (in GP) of the hole period, and every GP corresponds to 0.1 μm. The SiO_2 film was placed in the middle of the computational cell, and was surrounded by vacuum on one side, and a half space of silicon on the other.

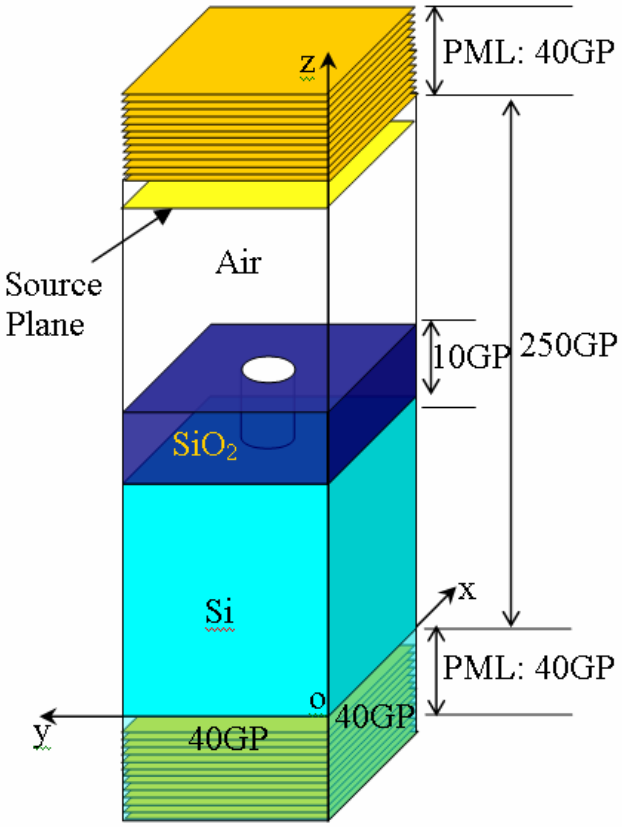

Figure 6.8 FDTD Computational Cell (courtesy of Rafif Hamam)

Absorption and dispersion in the SiO_2 film was incorporated by means of a modified Lorentz model for the dielectric function,

$$\varepsilon(\omega) = \varepsilon_\infty + \sum_{j=1}^{2} \frac{\sigma_j}{\omega_{0,j}{}^2 - \omega^2 - i\omega\gamma_j}, \tag{6.2}$$

where ε_∞ is the high-frequency dielectric constant, $\omega_{0,i}$ is the resonance absorption frequency, γ_i is the linewidth due to damping, and σ_i is the conductivity. These coefficients were obtained by fitting the actual complex dielectric function values [45] for SiO_2 to the above equation, and are listed in Table 6.1.

Parameter	$\sigma_i \left(rad^2 s^{-2}\right)$	$\omega_{0,i} \left(rad\ s^{-1}\right)$	$\gamma_i \left(rad\ s^{-1}\right)$	ε_∞
Resonance 1	4.4767×10^{27}	8.6732×10^{13}	3.3026×10^{12}	2.0014
Resonance 2	2.3584×10^{28}	2.0219×10^{14}	8.3983×10^{12}	2.0014

Table 6.1 FDTD Dielectric Function Parameters

A temporally Gaussian pulse was incident normally on the SiO_2 film from the vacuum side. Perfectly-matched-layer (PML) [115, 116] boundary conditions were applied on the boundaries normal to the incident light to prevent reflections, and periodic boundary conditions were applied in the other directions.

The electromagnetic fields at planes located on both sides of the film just before the PMLs were recorded. Then, the Poynting power fluxes were calculated from the discrete Fourier-transforms of the fields. However, this power then needs to be normalized to the incident flux. Thus, the simulation was repeated with vacuum only in the computational cell, and the fluxes were recorded again. The transmissivity, $T_{film}(\omega)$, is given by the ratio of the flux through the plane with the structure, over the flux through the same plane, but in the case where there is only vacuum. The calculation for the reflectivity, $R_{film}(\omega)$, is similar, although in this case the incident and reflected fields need to be separated before calculating the flux. The same procedure and calculations were also repeated for the perforated SiO_2 films.

FDTD simulations were run for the same geometries as the experimentally measured samples: 2 μm circular holes on a square lattice with a 4 μm or 8 μm period. The results are plotted in Figure 6.9. It is seen that there is very good agreement between the simulations and the measurements. The frequencies of the enhancement are the same, and even the magnitudes agree to within 10%.

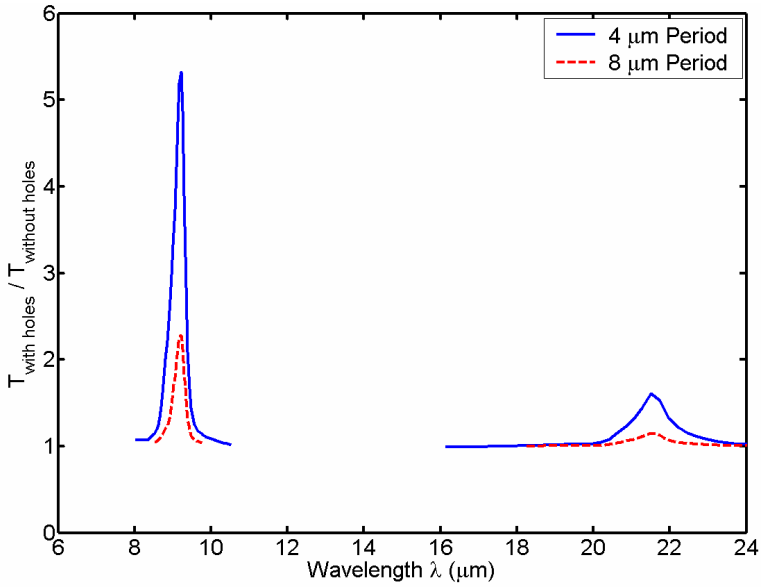

Figure 6.9 FDTD Simulation Results (courtesy of Rafif Hamam)

6.5 Conclusions

In this chapter, experimental measurements were made of infra-red transmission through silicon dioxide films perforated by subwavelength holes. It was seen that at particular frequencies, the transmission through the perforated film is significantly greater than that through a solid film. The frequencies where the extraordinary optical transmission is observed correspond very well with where surface phonon-polaritons are found to exist. Furthermore, results from FDTD simulations match the measured data very well. Further experiments with unsupported dielectric films and varied hole diameters could potentially further elucidate the mechanisms of transmission.

Chapter 7

Conclusions

7.1 Thesis Contributions

The contributions of this thesis can be grouped into two main themes. One is the transport of energy by surface polaritons along the in-plane direction of a thin film. The other is the transmission of energy in the perpendicular direction, through an amorphous film that is perforated by sub-wavelength holes.

This work is the first investigation of the energy transported by surface polaritons along the in-plane direction of thin films. Using a kinetic theory-based approach, it was calculated that the surface polaritons can transport a considerable amount of energy when the films are thin enough for significant splitting of the dispersion relations to occur [95]. The interesting result is that as the film thickness decreases, the energy transported by the surface polaritons increases. For a film of amorphous silicon dioxide, at a film thickness of 50 nm the surface phonon-polariton thermal conductivity is comparable to the bulk phonon thermal conductivity.

Next, a fluctuational electrodynamics approach was applied to the same problem. While this method has previously been applied to near-field radiation and direct emission calculations in the direction perpendicular to the film, before this work the in-plane direction

had not been addressed. The fluctuational electrodynamics calculations agree within a factor of two with the kinetic theory results.

Both calculations of the in-plane surface polariton energy flux point to the surface polariton propagation length as the source of the increased energy flux. Thus, an experimental measurement of the propagation length using ATR was performed. While ATR has been used to measure propagation lengths of surface polaritons on metals and crystalline dielectrics, this thesis presents the first experimental measurement of surface phonon-polaritons on an amorphous material. Although not generally considered a "good" polaritonic material due to its non-crystalline nature, these experiments show that surface phonon-polaritons on amorphous silicon dioxide can have a respectable propagation length.

The second major theme of this thesis is the transmission of energy through an amorphous silicon dioxide film perforated by sub-wavelength holes. Much theoretical and experimental work on EOT has been performed over the past decade, and while EOT has previously been observed, the material systems under consideration were metals and crystalline dielectrics. The experimental measurements of this work are the first observations of EOT for an amorphous material [117], and are also confirmed by FDTD simulations.

On a practical note, a survey of deposition conditions to develop a low-stress oxide was also performed. It was found that the residual stress of TEOS-based PECVD oxide films could be varied from compressive to tensile by changing the percentage of low-frequency RF power during the deposition. This result is of potential use in the micro-fabrication of free-standing structures.

7.2 Future Directions

The results for the in-plane energy transport by surface polaritons calculations are quite interesting, and suggest more consideration. In particular, the integration in the fluctuational electrodynamics should be treated with more advanced numerical techniques, perhaps along the lines of those suggested in Section 4.7.

While the EOT results strongly suggest the involvement of surface phonon-polaritons, the dependence of the enhanced transmission on the hole diameter and period could be teased out with more experiments. The observations suggest that smaller periods should be examined, but this requires commensurately smaller hole diameters which are beyond the resolution of the available contact photolithography. Finer linewidths using image reduction stepper projection is an option.

On the experimental side, measurements of suspended thin films would be the next step in validating the theoretical predictions. The first step would be to make ATR measurements of the anti-symmetric thin film surface polariton propagation length. This would then be followed by the more challenging in-plane thermal conductivity measurements, which might be accomplished using the 3ω method [118, 119] or an adaption of other techniques [120, 121]. However, regardless of the measurement method there are significant experimental challenges to overcome in the fabrication of the required suspended structures.

Finally, in regard to potential applications, both the kinetic theory model and the fluctuational electrodynamics calculation show that the source of the increase in thin film energy transport is the long propagation length of the anti-symmetric mode. However, this mode propagates mainly outside the film, and in the case that the surrounding dielectric is lossless. For practical devices in microelectronics and optoelectronics, this physical structure

is not realistic. An interesting avenue to pursue is cladding layers of photonic crystals [122] or superlattices [123] that may allow realization of the low damping and long propagation lengths in practical structures.

Appendix A

Fluctuational Electrodynamics Expressions

Explicit expressions for the electric and magnetic Green's functions of Chapter 4 are given in this Appendix, followed by some details of the algebraic manipulations of Eqn. (4.7). Example surface plots of the real and imaginary parts of the integrand for particular values of k_y, z, and z' are also shown for the case when the source and observation are both inside the film.

$$\ddot{G}_E(\vec{r},\vec{r}',\omega) = \int_{-\infty}^{\infty}\int_{-\infty}^{\infty} \frac{dk_x dk_y}{4\pi^2}\frac{i}{2k_{z3}} e^{i\left(k_x(x-x')+k_y(y-y')\right)} \times$$

$$\left[\begin{array}{c}
\frac{1}{k_\rho^2}\hat{x}\hat{x}\left(k_y^2\left(e^{ik_{z3}|z-z'|}+\rho_{32}^s e^{ik_{z3}(z+z')}+\rho_{31}^s e^{ik_{z3}(2d-z-z')}\right)+\frac{k_x^2 k_{z3}^2}{k_3^2}\left(\rho_{32}^p e^{ik_{z3}(z+z')}+\rho_{31}^p e^{ik_{z3}(2d-z-z')}\right)\right)\\
-\frac{k_x k_y}{k_\rho^2}\hat{x}\hat{y}\left(\left(e^{ik_{z3}|z-z'|}+\rho_{32}^s e^{ik_{z3}(z+z')}+\rho_{31}^s e^{ik_{z3}(2d-z-z')}\right)-\frac{k_{z3}^2}{k_3^2}\left(\rho_{32}^p e^{ik_{z3}(z+z')}+\rho_{31}^p e^{ik_{z3}(2d-z-z')}\right)\right)\\
+\hat{x}\hat{z}\left(\frac{k_x k_{z3}}{k_3^2}\left(\rho_{32}^p e^{ik_{z3}(z+z')}-\rho_{31}^p e^{ik_{z3}(2d-z-z')}\right)\right)\\
-\frac{k_x k_y}{k_\rho^2}\hat{y}\hat{x}\left(\left(e^{ik_{z3}|z-z'|}+\rho_{32}^s e^{ik_{z3}(z+z')}+\rho_{31}^s e^{ik_{z3}(2d-z-z')}\right)-\frac{k_{z3}^2}{k_3^2}\left(\rho_{32}^p e^{ik_{z3}(z+z')}+\rho_{31}^p e^{ik_{z3}(2d-z-z')}\right)\right)\\
+\frac{1}{k_\rho^2}\hat{y}\hat{y}\left(k_x^2\left(e^{ik_{z3}|z-z'|}+\rho_{32}^s e^{ik_{z3}(z+z')}+\rho_{31}^s e^{ik_{z3}(2d-z-z')}\right)+\frac{k_y^2 k_{z3}^2}{k_3^2}\left(\rho_{32}^p e^{ik_{z3}(z+z')}+\rho_{31}^p e^{ik_{z3}(2d-z-z')}\right)\right)\\
+\hat{y}\hat{z}\left(\frac{k_y k_{z3}}{k_3^2}\left(\rho_{32}^p e^{ik_{z3}(z+z')}-\rho_{31}^p e^{ik_{z3}(2d-z-z')}\right)\right)\\
-\hat{z}\hat{x}\left(\frac{k_x k_{z3}}{k_3^2}\left(\rho_{32}^p e^{ik_{z3}(z+z')}-\rho_{31}^p e^{ik_{z3}(2d-z-z')}\right)\right)\\
-\hat{z}\hat{y}\left(\frac{k_y k_{z3}}{k_3^2}\left(\rho_{32}^p e^{ik_{z3}(z+z')}-\rho_{31}^p e^{ik_{z3}(2d-z-z')}\right)\right)\\
+\frac{1}{k_0^2\varepsilon_3}\hat{z}\hat{z}\left(\left(k_\rho-\frac{k_{z3}(z-z')}{|z-z'|}\right)^2 e^{ik_{z3}|z-z'|}-k_\rho^2\left(\rho_{32}^p e^{ik_{z3}(z+z')}+\rho_{31}^p e^{ik_{z3}(2d-z-z')}\right)+i2k_{z3}\delta(z-z')\right)
\end{array}\right]$$

$$\ddot{\vec{G}}_H\left(\vec{r},\vec{r}',\omega\right)=\int_{-\infty}^{\infty}\int_{-\infty}^{\infty}\frac{dk_x dk_y}{4\pi^2}e^{i\left(k_x(x-x')+k_y(y-y')\right)}\frac{-1}{2k_{z3}}\times$$

$$\left[\begin{array}{c}
\frac{k_x k_y k_{z3}}{k_\rho^2}\hat{x}\hat{x}\left(\left(e^{ik_{z3}|z-z'|}+\rho_{32}^s e^{ik_{z3}(z+z')}-\rho_{31}^s e^{ik_{z3}(2d-z-z')}\right)-\frac{\left(k_\rho^2+k_{z3}^2\right)}{k_3^2}\left(\rho_{32}^p e^{ik_{z3}(z+z')}-\rho_{31}^p e^{ik_{z3}(2d-z-z')}\right)\right)\\
-\frac{k_{z3}}{k_\rho^2}\hat{x}\hat{y}\left(k_x^2\left(e^{ik_{z3}|z-z'|}+\rho_{32}^s e^{ik_{z3}(z+z')}-\rho_{31}^s e^{ik_{z3}(2d-z-z')}\right)+\frac{k_y^2\left(k_\rho^2+k_{z3}^2\right)}{k_3^2}\left(\rho_{32}^p e^{ik_{z3}(z+z')}-\rho_{31}^p e^{ik_{z3}(2d-z-z')}\right)\right)\\
+\frac{k_y}{k_3^2}\hat{x}\hat{z}\left(\left(k_\rho-\frac{k_{z3}(z-z')}{|z-z'|}\right)^2 e^{ik_{z3}|z-z'|}-\left(k_\rho^2+k_{z3}^2\right)\left(\rho_{32}^p e^{ik_{z3}(z+z')}+\rho_{31}^p e^{ik_{z3}(2d-z-z')}\right)+2ik_{z3}\delta(z-z')\right)\\
+\frac{k_{z3}}{k_\rho^2}\hat{y}\hat{x}\left(k_y^2\left(e^{ik_{z3}|z-z'|}+\rho_{32}^s e^{ik_{z3}(z+z')}-\rho_{31}^s e^{ik_{z3}(2d-z-z')}\right)+\frac{k_x^2\left(k_\rho^2+k_{z3}^2\right)}{k_3^2}\left(\rho_{32}^p e^{ik_{z3}(z+z')}-\rho_{31}^p e^{ik_{z3}(2d-z-z')}\right)\right)\\
\frac{-k_x k_y k_{z3}}{k_\rho^2}\hat{y}\hat{y}\left(\left(e^{ik_{z3}|z-z'|}+\rho_{32}^s e^{ik_{z3}(z+z')}-\rho_{31}^s e^{ik_{z3}(2d-z-z')}\right)-\frac{\left(k_\rho^2+k_{z3}^2\right)}{k_3^2}\left(\rho_{32}^p e^{ik_{z3}(z+z')}-\rho_{31}^p e^{ik_{z3}(2d-z-z')}\right)\right)\\
\frac{-k_x}{k_3^2}\hat{y}\hat{z}\left(\left(k_\rho-\frac{k_{z3}(z-z')}{|z-z'|}\right)^2 e^{ik_{z3}|z-z'|}-\left(k_\rho^2+k_{z3}^2\right)\left(\rho_{32}^p e^{ik_{z3}(z+z')}+\rho_{31}^p e^{ik_{z3}(2d-z-z')}\right)+2ik_{z3}\delta(z-z')\right)\\
-k_y\hat{z}\hat{x}\left(e^{ik_{z3}|z-z'|}+\rho_{32}^s e^{ik_{z3}(z+z')}+\rho_{31}^s e^{ik_{z3}(2d-z-z')}\right)\\
+k_x\hat{z}\hat{y}\left(e^{ik_{z3}|z-z'|}+\rho_{32}^s e^{ik_{z3}(z+z')}+\rho_{31}^s e^{ik_{z3}(2d-z-z')}\right)\\
+0\hat{z}\hat{z}
\end{array}\right]$$

Substitution of $\ddot{\mathbf{G}}_{\mathbf{E}}$ and $\ddot{\mathbf{G}}_{\mathbf{H}}$ into Eqn. (4.7) results in,

$$
\begin{aligned}
&\left\langle E_y H_z^* - E_z H_y^* \right\rangle = \\
&\frac{i\omega^2 \mu_o \varepsilon_o \varepsilon''\Theta(\omega,T)}{\pi} \int_{z_1}^{z_2} dz' \int_{-\infty}^{\infty} dy' \int_{-\infty}^{0} dx' \int_{-\infty}^{\infty}\int_{-\infty}^{\infty} \frac{dk_x dk_y}{4\pi^2} \frac{i}{2k_{z3}} e^{i\left(k_x(x-x')+k_y(y-y')\right)} \int_{-\infty}^{\infty}\int_{-\infty}^{\infty} \frac{dk_{x'} dk_{y'}}{4\pi^2} e^{-i\left(k_{x'}(x-x')+k_{y'}(y-y')\right)} \frac{-1}{2k_{z3}^*} \bullet \\
&\left(-\frac{k_x k_y}{k_\rho^2}\left(\left(e^{ik_{z3}|z-z'|} + \rho_{32}^s e^{ik_{z3}(z+z')} + \rho_{31}^s e^{ik_{z3}(2d-z-z')} \right) - \frac{k_{z3}^2}{k_3^2}\left(\rho_{32}^p e^{ik_{z3}(z+z')} + \rho_{31}^p e^{ik_{z3}(2d-z-z')} \right) \right) \bullet \right. \\
&\left(-k_{y'} \left(e^{ik_{z3'}|z-z'|} + \rho_{32}^s, e^{ik_{z3'}(z+z')} + \rho_{31}^s, e^{ik_{z3'}(2d-z-z')} \right) \right)^* \\
&+ \frac{1}{k_\rho^2}\left(k_x^2 \left(e^{ik_{z3}|z-z'|} + \rho_{32}^s e^{ik_{z3}(z+z')} + \rho_{31}^s e^{ik_{z3}(2d-z-z')} \right) + \frac{k_y^2 k_{z3}^2}{k_3^2}\left(\rho_{32}^p e^{ik_{z3}(z+z')} + \rho_{31}^p e^{ik_{z3}(2d-z-z')} \right) \right) \bullet \\
&\left(k_{x'} \left(e^{ik_{z3'}|z-z'|} + \rho_{32}^s, e^{ik_{z3'}(z+z')} + \rho_{31}^s, e^{ik_{z3'}(2d-z-z')} \right) \right)^* \\
&+ \left(\frac{k_x k_{z3}}{k_3^2}\left(\rho_{32}^p e^{ik_{z3}(z+z')} - \rho_{31}^p e^{ik_{z3}(2d-z-z')} \right) \right) \bullet \\
&\left(\frac{k_{z3'}}{k_{\rho'}^2}\left(k_{y'}^2 \left(e^{ik_{z3'}|z-z'|} + \rho_{32}^s, e^{ik_{z3'}(z+z')} - \rho_{31}^s, e^{ik_{z3'}(2d-z-z')} \right) + \frac{k_{x'}^2 \left(k_{\rho'}^2 + k_{z3'}^2 \right)}{k_3^2}\left(\rho_{32}^p, e^{ik_{z3'}(z+z')} - \rho_{31}^p, e^{ik_{z3'}(2d-z-z')} \right) \right) \right)^* \\
&+ \left(\frac{k_y k_{z3}}{k_3^2}\left(\rho_{32}^p e^{ik_{z3}(z+z')} - \rho_{31}^p e^{ik_{z3}(2d-z-z')} \right) \right) \bullet \\
&\left(\frac{-k_x, k_y, k_{z3'}}{k_{\rho'}^2}\left(\left(e^{ik_{z3'}|z-z'|} + \rho_{32}^s, e^{ik_{z3'}(z+z')} - \rho_{31}^s, e^{ik_{z3'}(2d-z-z')} \right) - \frac{\left(k_{\rho'}^2 + k_{z3'}^2 \right)}{k_3^2}\left(\rho_{32}^p, e^{ik_{z3'}(z+z')} - \rho_{31}^p, e^{ik_{z3'}(2d-z-z')} \right) \right) \right)^* \\
&- \frac{1}{k_0^2 \varepsilon_3}\left(\left(k_\rho - \frac{k_{z3}(z-z')}{|z-z'|} \right)^2 e^{ik_{z3}|z-z'|} - k_\rho^2 \left(\rho_{32}^p e^{ik_{z3}(z+z')} + \rho_{31}^p e^{ik_{z3}(2d-z-z')} \right) + i2k_{z3}\delta(z-z') \right) \bullet \\
&\left. \left(\frac{-k_{x'}}{k_3^2}\left(\left(k_{\rho'} - \frac{k_{z3'}(z-z')}{|z-z'|} \right)^2 e^{ik_{z3'}|z-z'|} - \left(k_{\rho'}^2 + k_{z3'}^2 \right)\left(\rho_{32}^p, e^{ik_{z3'}(z+z')} + \rho_{31}^p, e^{ik_{z3'}(2d-z-z')} \right) + 2ik_{z3'}\delta(z-z') \right) \right)^* \right)
\end{aligned}
$$

collect x' and y' terms, and do integrations over x' and y' to get Dirac delta functions in k_y and k_x

$$\int_{-\infty}^{\infty} dy' e^{i\left(k_{y'}-k_y\right)y'} = \left(2\pi\right)\delta\left(k_{y'}-k_y\right)$$

$$\int_{-\infty}^{0} dx' e^{i\left(k_{x'}-k_x\right)x'} = \left(\pi\right)\delta\left(k_{x'}-k_x\right)+\frac{i}{\left(k_{x'}-k_x\right)}$$

$$\left\langle E_y H_z^* - E_z H_y^* \right\rangle = \frac{\omega^2 \mu_o \varepsilon_o \varepsilon'' \Theta\left(\omega,T\right)}{32\pi^4} \int_{z_1}^{z_2} dz' \int_{-\infty}^{0} dx' e^{i\left(k_{x'}-k_x\right)x'} \int_{-\infty}^{\infty}\int_{-\infty}^{\infty} \frac{dk_x dk_y}{k_{z3} k_{z3'}^*} \int_{-\infty}^{\infty} \frac{dk_{x'}}{1} e^{i\left(k_x-k_{x'}\right)x}$$

$$\left(
\begin{array}{l}
-\frac{k_x k_y}{k_\rho^2}\left(\left(e^{ik_{z3}|z-z'|}+\rho_{32}^s e^{ik_{z3}(z+z')}+\rho_{31}^s e^{ik_{z3}(2d-z-z')}\right)-\frac{k_{z3}^2}{k_3^2}\left(\rho_{32}^p e^{ik_{z3}(z+z')}+\rho_{31}^p e^{ik_{z3}(2d-z-z')}\right)\right)\bullet \\
\left(-k_y\left(e^{-ik_{z3'}^*|z-z'|}+\rho_{32}^{s*} e^{-ik_{z3'}^*(z+z')}+\rho_{31}^{s*} e^{-ik_{z3'}^*(2d-z-z')}\right)\right) \\
+\frac{1}{k_\rho^2}\left(k_x^2\left(e^{ik_{z3}|z-z'|}+\rho_{32}^s e^{ik_{z3}(z+z')}+\rho_{31}^s e^{ik_{z3}(2d-z-z')}\right)+\frac{k_y^2 k_{z3}^2}{k_3^2}\left(\rho_{32}^p e^{ik_{z3}(z+z')}+\rho_{31}^p e^{ik_{z3}(2d-z-z')}\right)\right)\bullet \\
\left(k_{x'}\left(e^{-ik_{z3'}^*|z-z'|}+\rho_{32}^{s*} e^{-ik_{z3'}^*(z+z')}+\rho_{31}^{s*} e^{-ik_{z3'}^*(2d-z-z')}\right)\right) \\
+\left(\frac{k_x k_{z3}}{k_3^2}\left(\rho_{32}^p e^{ik_{z3}(z+z')}-\rho_{31}^p e^{ik_{z3}(2d-z-z')}\right)\right)\bullet \\
\left(\frac{k_{z3'}^*}{k_{\rho'}^2}\left(k_y^2\left(e^{-ik_{z3'}^*|z-z'|}+\rho_{32}^{s*} e^{-ik_{z3'}^*(z+z')}-\rho_{31}^{s*} e^{-ik_{z3'}^*(2d-z-z')}\right)+\frac{k_{x'}^2\left(k_{\rho'}^2+k_{z3'}^{2*}\right)}{k_3^{2*}}\left(\rho_{32}^{p*} e^{-ik_{z3'}^*(z+z')}-\rho_{31}^{p*} e^{-ik_{z3'}^*(2d-z-z')}\right)\right)\right) \\
+\left(\frac{k_y k_{z3}}{k_3^2}\left(\rho_{32}^p e^{ik_{z3}(z+z')}-\rho_{31}^p e^{ik_{z3}(2d-z-z')}\right)\right)\bullet \\
\left(\frac{-k_x k_{z3'}^*}{k_{\rho'}^2}\left(\left(e^{-ik_{z3'}^*|z-z'|}+\rho_{32}^{s*} e^{-ik_{z3'}^*(z+z')}-\rho_{31}^{s*} e^{-ik_{z3'}^*(2d-z-z')}\right)-\frac{\left(k_{\rho'}^2+k_{z3'}^{2*}\right)}{k_3^{2*}}\left(\rho_{32}^{p*} e^{-ik_{z3'}^*(z+z')}-\rho_{31}^{p*} e^{-ik_{z3'}^*(2d-z-z')}\right)\right)\right) \\
-\frac{1}{k_0^2\varepsilon_3}\left(\left(k_\rho-\frac{k_{z3}\left(z-z'\right)}{|z-z'|}\right)^2 e^{ik_{z3}|z-z'|}-k_\rho^2\left(\rho_{32}^p e^{ik_{z3}(z+z')}+\rho_{31}^p e^{ik_{z3}(2d-z-z')}\right)+i2k_{z3}\delta\left(z-z'\right)\right)\bullet \\
\left(\frac{-k_{x'}}{k_3^{2*}}\left(\left(k_{\rho'}-\frac{k_{z3'}^*\left(z-z'\right)}{|z-z'|}\right)^2 e^{-ik_{z3'}^*|z-z'|}-\left(k_{\rho'}^2+k_{z3'}^{2*}\right)\left(\rho_{32}^{p*} e^{-ik_{z3'}^*(z+z')}+\rho_{31}^{p*} e^{-ik_{z3'}^*(2d-z-z')}\right)-2ik_{z3'}^*\delta\left(z-z'\right)\right)\right)
\end{array}
\right)$$

$$\left\langle E_y H_z^* - E_z H_y^* \right\rangle = \frac{\omega^2 \mu_o \varepsilon_o \varepsilon'' \Theta(\omega, T)}{32\pi^3} \int_{z_1}^{z_2} dz' \int_{-\infty}^{\infty} \int_{-\infty}^{\infty} \frac{dk_x dk_y}{k_{z3} k_{z3}^*}$$

$$\left(\begin{array}{l}
\frac{k_x k_y^2}{k_\rho^2} \left(\left(e^{ik_{z3}|z-z'|} + \rho_{32}^s e^{ik_{z3}(z+z')} + \rho_{31}^s e^{ik_{z3}(2d-z-z')} \right) - \frac{k_{z3}^2}{k_3^2} \left(\rho_{32}^p e^{ik_{z3}(z+z')} + \rho_{31}^p e^{ik_{z3}(2d-z-z')} \right) \right) \bullet \\
\left(e^{-ik_{z3}^*|z-z'|} + \rho_{32}^{s*} e^{-ik_{z3}^*(z+z')} + \rho_{31}^{s*} e^{-ik_{z3}^*(2d-z-z')} \right) \\
+ \frac{1}{k_\rho^2} \left(k_x^2 \left(e^{ik_{z3}|z-z'|} + \rho_{32}^s e^{ik_{z3}(z+z')} + \rho_{31}^s e^{ik_{z3}(2d-z-z')} \right) + \frac{k_y^2 k_{z3}^2}{k_3^2} \left(\rho_{32}^p e^{ik_{z3}(z+z')} + \rho_{31}^p e^{ik_{z3}(2d-z-z')} \right) \right) \bullet \\
\left(k_x \left(e^{-ik_{z3}^*|z-z'|} + \rho_{32}^{s*} e^{-ik_{z3}^*(z+z')} + \rho_{31}^{s*} e^{-ik_{z3}^*(2d-z-z')} \right) \right) \\
+ \left(\frac{k_x k_{z3}}{k_3^2} \left(\rho_{32}^p e^{ik_{z3}(z+z')} - \rho_{31}^p e^{ik_{z3}(2d-z-z')} \right) \right) \bullet \\
\left(\frac{k_{z3}^*}{k_\rho^2} \left(k_y^2 \left(e^{-ik_{z3}^*|z-z'|} + \rho_{32}^{s*} e^{-ik_{z3}^*(z+z')} - \rho_{31}^{s*} e^{-ik_{z3}^*(2d-z-z')} \right) + \frac{k_x^2 \left(k_\rho^2 + k_{z3}^{2*} \right)}{k_3^{2*}} \left(\rho_{32}^{p*} e^{-ik_{z3}^*(z+z')} - \rho_{31}^{p*} e^{-ik_{z3}^*(2d-z-z')} \right) \right) \right) \\
+ \left(\frac{k_y k_{z3}}{k_3^2} \left(\rho_{32}^p e^{ik_{z3}(z+z')} - \rho_{31}^p e^{ik_{z3}(2d-z-z')} \right) \right) \bullet \\
\left(\frac{-k_x k_y k_{z3}^*}{k_\rho^2} \left(\left(e^{-ik_{z3}^*|z-z'|} + \rho_{32}^{s*} e^{-ik_{z3}^*(z+z')} - \rho_{31}^{s*} e^{-ik_{z3}^*(2d-z-z')} \right) - \frac{\left(k_\rho^2 + k_{z3}^{2*} \right)}{k_3^{2*}} \left(\rho_{32}^{p*} e^{-ik_{z3}^*(z+z')} - \rho_{31}^{p*} e^{-ik_{z3}^*(2d-z-z')} \right) \right) \right) \\
- \frac{1}{k_0^2 \varepsilon_3} \left(\left(k_\rho - \frac{k_{z3}(z-z')}{|z-z'|} \right)^2 e^{ik_{z3}|z-z'|} - k_\rho^2 \left(\rho_{32}^p e^{ik_{z3}(z+z')} + \rho_{31}^p e^{ik_{z3}(2d-z-z')} \right) + i2k_{z3} \delta(z-z') \right) \bullet \\
\left(\frac{-k_x}{k_3^{2*}} \left(\left(k_\rho - \frac{k_{z3}^*(z-z')}{|z-z'|} \right)^2 e^{-ik_{z3}^*|z-z'|} - \left(k_\rho^2 + k_{z3}^{2*} \right) \left(\rho_{32}^{p*} e^{-ik_{z3}^*(z+z')} + \rho_{31}^{p*} e^{-ik_{z3}^*(2d-z-z')} \right) - 2ik_{z3}^* \delta(z-z') \right) \right)
\end{array} \right)$$

continued on next page

$$
+\frac{i\omega^2\mu_o\varepsilon_o\varepsilon''\Theta(\omega,T)}{32\pi^4}\int_{z_1}^{z_2}dz'\int_{-\infty}^{\infty}\int_{-\infty}^{\infty}dk_x dk_y\int_{-\infty}^{\infty}dk_{x'}\frac{e^{i(k_x-k_{x'})x}}{(k_{x'}-k_x)k_{z3}k_{z3'}^*}
$$

$$
\left(\begin{array}{l}
\left(\frac{k_x k_y^2}{k_\rho^2}\left(\left(e^{ik_{z3}|z-z'|}+\rho_{32}^s e^{ik_{z3}(z+z')}+\rho_{31}^s e^{ik_{z3}(2d-z-z')}\right)-\frac{k_{z3}^2}{k_3^2}\left(\rho_{32}^p e^{ik_{z3}(z+z')}+\rho_{31}^p e^{ik_{z3}(2d-z-z')}\right)\right)\bullet\right.\\
\left(e^{-ik_{z3'}^*|z-z'|}+\rho_{32}^{s*}e^{-ik_{z3'}^*(z+z')}+\rho_{31}^{s*}e^{-ik_{z3'}^*(2d-z-z')}\right)\\
+\frac{1}{k_\rho^2}\left(k_x^2\left(e^{ik_{z3}|z-z'|}+\rho_{32}^s e^{ik_{z3}(z+z')}+\rho_{31}^s e^{ik_{z3}(2d-z-z')}\right)+\frac{k_y^2k_{z3}^2}{k_3^2}\left(\rho_{32}^p e^{ik_{z3}(z+z')}+\rho_{31}^p e^{ik_{z3}(2d-z-z')}\right)\right)\bullet\\
\left(k_{x'}\left(e^{-ik_{z3'}^*|z-z'|}+\rho_{32}^{s*}e^{-ik_{z3'}^*(z+z')}+\rho_{31}^{s*}e^{-ik_{z3'}^*(2d-z-z')}\right)\right)\\
+\left(\frac{k_x k_{z3}}{k_3^2}\left(\rho_{32}^p e^{ik_{z3}(z+z')}-\rho_{31}^p e^{ik_{z3}(2d-z-z')}\right)\right)\bullet\\
\left(\frac{k_{z3'}^*}{k_{\rho'}^2}\left(k_y^2\left(e^{-ik_{z3'}^*|z-z'|}+\rho_{32}^{s*}e^{-ik_{z3'}^*(z+z')}-\rho_{31}^{s*}e^{-ik_{z3'}^*(2d-z-z')}\right)+\frac{k_{x'}^2\left(k_{\rho'}^2+k_{z3'}^{2*}\right)}{k_3^{2*}}\left(\rho_{32}^{p*}e^{-ik_{z3'}^*(z+z')}-\rho_{31}^{p*}e^{-ik_{z3'}^*(2d-z-z')}\right)\right)\right)\\
+\left(\frac{k_y k_{z3}}{k_3^2}\left(\rho_{32}^p e^{ik_{z3}(z+z')}-\rho_{31}^p e^{ik_{z3}(2d-z-z')}\right)\right)\bullet\\
\left(\frac{-k_x,k_y k_{z3'}^*}{k_{\rho'}^2}\left(\left(e^{-ik_{z3'}^*|z-z'|}+\rho_{32}^{s*},e^{-ik_{z3'}^*(z+z')}-\rho_{31}^{s*},e^{-ik_{z3'}^*(2d-z-z')}\right)-\frac{\left(k_{\rho'}^2+k_{z3'}^{2*}\right)}{k_3^{2*}}\left(\rho_{32}^{p*},e^{-ik_{z3'}^*(z+z')}-\rho_{31}^{p*},e^{-ik_{z3'}^*(2d-z-z')}\right)\right)\right)\\
-\frac{1}{k_0^2\varepsilon_3}\left(\left(k_\rho-\frac{k_{z3}(z-z')}{|z-z'|}\right)^2 e^{ik_{z3}|z-z'|}-k_\rho^2\left(\rho_{32}^p e^{ik_{z3}(z+z')}+\rho_{31}^p e^{ik_{z3}(2d-z-z')}\right)+i2k_{z3}\delta(z-z')\right)\bullet\\
\left.\left(\frac{-k_{x'}}{k_3^{2*}}\left(\left(k_{\rho'}-\frac{k_{z3'}^*(z-z')}{|z-z'|}\right)^2 e^{-ik_{z3'}^*|z-z'|}-\left(k_{\rho'}^2+k_{z3'}^{2*}\right)\left(\rho_{32}^{p*},e^{-ik_{z3'}^*(z+z')}+\rho_{31}^{p*},e^{-ik_{z3'}^*(2d-z-z')}\right)-2ik_{z3'}^*\delta(z-z')\right)\right)\right)
\end{array}\right)
$$

The first term (on the previous page) is the symmetric term which occurs when the entire film is at the same temperature. Thus, only the second term (the one on this page) contributes to the in-plane flux.

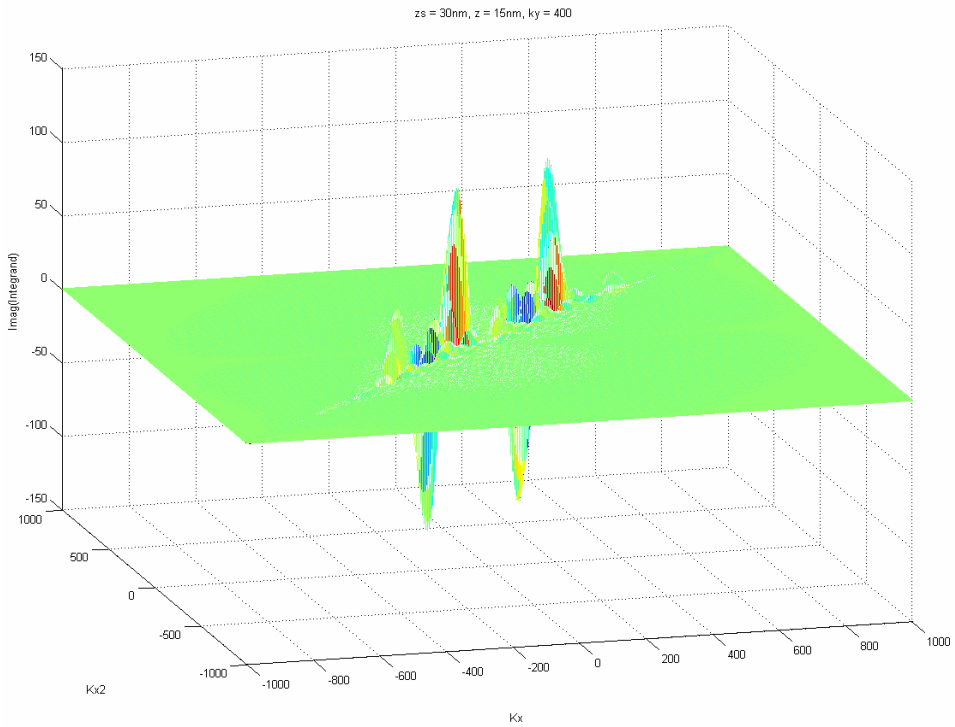

Figure A.1 Imaginary Part of Integrand

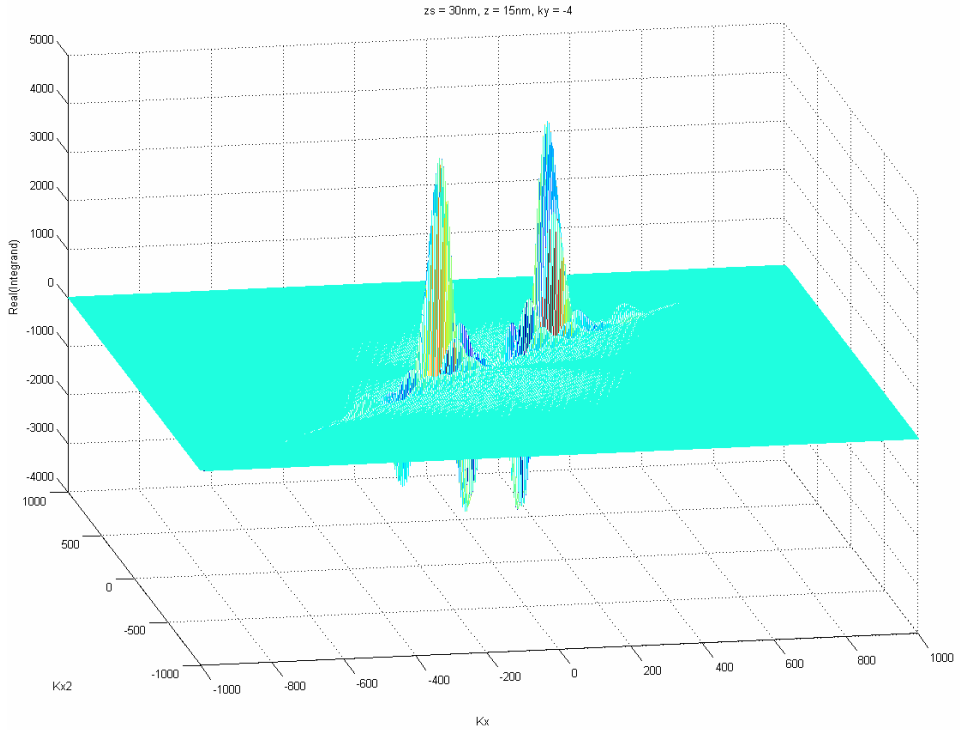

Figure A.2 Real Part of Integrand

Appendix B

FORTRAN Recursion Code

In this Appendix a stripped-down version of the code used to perform the numerical integration is given. The actual code is split around the four singularities that occur in the integrand. The main program, functions and modules have been re-arranged below to permit ease of following the logical flow. The actual program has all of the modules listed before the main program, and all of the functions after. Note the use of recursive functions which allow the functions to call themselves (either directly or indirectly). The particular QUADPACK subroutine QAGS (Quadrature Adaptive General integrand Singularities) is not given but is easily found in the literature [92].

```
program
       call integralzs(e1,e2,e3,d,z,x)   ! passes the various parameters to use
end program

! this function does the 4th integration over zs
function integralzs(e1, e2, e3, d, z, x)
       use params
       use func1
       real, intent(in) :: e1, e2, d, z, x
       complex, intent(in) :: e3
       real :: integralzs

       e1val = e1
       e2val = e2
       e3val = e3
       dval = d
       zval = z
       xval = x

       call qags (fzs, zsmin, zsmax, epsabs, epsrel, result, abserr, neval, ier)
       integralzs = result
end function integralzs

! takes a fxn of 1 variable and parameters, and makes it callable as a function
! of one variable: zs
module func1
       real :: e1val, e2val, dval, zval, xval
       complex :: e3val
contains
       function fzs(zsval)
              real, intent(in) :: zsval
              real :: fzs

              fzs = integralky(zsval, e1val, e2val, e3val, dval, zval, xval)
```

```
	end function fzs
end module func1


! this function does the 3rd integration over ky
function integralky(zs, e1, e2, e3, d, z, x)
	use params
	use func2
	real, intent(in) :: zs, e1, e2, d, z, x
	complex, intent(in) :: e3
	real :: integralky

	zsval = zs
	e1val = e1
	e2val = e2
	e3val = e3
	dval = d
	zval = z
	xval = x

	call qags(fky, kymin, kymax, epsabs, epsrel, result, abserr, neval, ier)
	integralky = result
end function integralyky

! takes a fxn of 2 variables and parameters, and makes it callable as a
! function of one variable: ky
module func2
	real :: zsval, e1val, e2val, dval, zval, xval
	complex :: e3val
contains
	function fky(kyval)
		real, intent(in) :: kyval
		real :: fky

		fky = integralkx(kyval, zsval, e1val, e2val, e3val, dval, zval,
xval)
	end function fky
end module func2

! this function does the 2nd integration over kx
recursive function integralkx(ky, zs, e1, e2, e3, d, z, x)
	use params
	use func3
	real, intent(in) :: ky, zs, e1, e2, d, z, x
	complex, intent(in) :: e3
	real :: integralkx

	kyval = ky
	zsval = zs
	e1val = e1
	e2val = e2
	e3val = e3
	dval = d
	zval = z
	xval = x

	call qags(fkx, kxmin, kxmax, epsabs, epsrel, result, abserr, neval, ier)
	integralkx = result
end function integralkx

! takes a fxn of 3 variables and parameters, and makes it callable as a
! function of one variable: kx
module func3
	real :: kyval, zsval, e1val, e2val, dval, zval, xval
	complex :: e3val
contains
	function fkx(kxval)
		real, intent(in) :: kxval
		real :: fkx

		fkx = integralkx2(kxval, kyval, zsval, e1val, e2val, e3val, dval,
zval, xval)
```

```
	end function fkx
end module func3

! this function does the 1st integration over kx2
recursive function integralkx2(kx, ky, zs, e1, e2, e3, d, z, x)
	use params
	use func4
	real, intent(in) :: kx, ky, zs, e1, e2, d, z, x
	complex, intent(in) :: e3
	real :: integralkx2

	kxval = kx
	kyval = ky
	zsval = zs
	e1val = e1
	e2val = e2
	e3val = e3
	dval = d
	zval = z
	xval = x

	call qags(fkx2, kx2min, kx2max, epsabs, epsrel, result, abserr, neval,
ier)
	integralkx2 = result
end function integralkx2

! takes a fxn of 4 variables and parameters, and makes it callable as a
! function of one variable: kx2
module func4
	real :: kxval, kyval, zsval, e1val, e2val, dval, zval, xval
	complex :: e3val
contains
	function fkx2(kx2val)
		real, intent(in) :: kx2val
		real :: fkx2		! this is the function to integrate

		fkx2 = function(kx2val, kxval, kyval, zsval, e1val, e2val, e3val,
dval, zval, xval)
	end function fkx2
end module func4



! the actual function to integrate is below:
function fkx2(kx2val)
	real, intent(in) :: kx2val
	real :: fkx2			! this is the function to integrate
					! this one for the quadruple integral
					! this function expects normalized values for
					! kx, kx2, ky, and zs
	real :: kp, kp2, k0		! these are intermediate variables used just
					! inside this function

	complex :: kz1, kz2, kz3, kz12, kz22, kz32
	complex :: rs31, rs32, rp31, rp32
	complex :: ps31, ps32, pp31, pp32
	complex :: rs312, rs322, rp312, rp322
	complex :: ps312, ps322, pp312, pp322
	complex :: GEyx, GEyy, GEzx, GEzy, GEzz
	complex :: GHxz2, GHyz2, GHxy2, GHyy2, GHzy2

!	c = 3e8;
!	k0 = w/c;			! real

	k0 = 1.0d0			! everything is normalized to k0, so k0 = 1

	kz1 = sqrt(dcmplx(e1val*k0**2 - kxval**2 - kyval**2))
		! real or imaginary if kx and/or ky is big enough
	kz2 = sqrt(dcmplx(e2val*k0**2 - kxval**2 - kyval**2))
		! real or imaginary if kx and/or ky is big enough
	kz3 = sqrt(dcmplx(e3val*k0**2 - kxval**2 - kyval**2))
		! complex because e3 is complex
```

```
      kp = sqrt(kxval**2 + kyval**2)
            ! real and positive


      kz12 = sqrt(dcmplx(e1val*k0**2-kx2val**2-kyval**2))
            ! real or imaginary if kx and/or ky is big enough
      kz22 = sqrt(dcmplx(e2val*k0**2-kx2val**2-kyval**2))
            ! real or imaginary if kx and/or ky is big enough
      kz32 = sqrt(dcmplx(e3val*k0**2-kx2val**2-kyval**2))
            ! complex because e3 is complex
      kp2 = sqrt(kx2val**2 + kyval**2)
            ! real and positive

      rs31 = (kz3 - kz1)/(kz3 + kz1)    ! complex because kz3 is complex
      rs32 = (kz3 - kz2)/(kz3 + kz2)    ! complex because kz3 is complex
      rp31 = (e1val*kz3 - e3val*kz1)/(e1val*kz3 + e3val*kz1)
      rp32 = (e2val*kz3 - e3val*kz2)/(e2val*kz3 + e3val*kz2)

      rs312 = (kz32 - kz12)/(kz32 + kz12)     ! complex because kz3 is complex
      rs322 = (kz32 - kz22)/(kz32 + kz22)     ! complex because kz3 is complex
      rp312 = (e1val*kz32 - e3val*kz12)/(e1val*kz32 + e3val*kz12)
      rp322 = (e2val*kz32 - e3val*kz22)/(e2val*kz32 + e3val*kz22)

      ps31 = rs31/(1 - rs31*rs32*exp((0.0d0,1.0d0)*2.0d0*kz3*dval))
      ps32 = rs32/(1 - rs31*rs32*exp((0.0d0,1.0d0)*2.0d0*kz3*dval))
      pp31 = rp31/(1 - rp31*rp32*exp((0.0d0,1.0d0)*2.0d0*kz3*dval))
      pp32 = rp32/(1 - rp31*rp32*exp((0.0d0,1.0d0)*2.0d0*kz3*dval))

      ps312 = rs312/(1 -rs312*rs322*exp((0.0d0,1.0d0)*2.0d0*kz32*dval))
      ps322 = rs322/(1 -rs312*rs322*exp((0.0d0,1.0d0)*2.0d0*kz32*dval))
      pp312 = rp312/(1 -rp312*rp322*exp((0.0d0,1.0d0)*2.0d0*kz32*dval))
      pp322 = rp322/(1 -rp312*rp322*exp((0.0d0,1.0d0)*2.0d0*kz32*dval))

      GEyx = (kxval*kyval**2/kp**2)*((exp((0.0d0,1.0d0)*kz3*abs(zval - zsval))
+ ps32*exp((0.0d0,1.0d0)*kz3*(zval + zsval)) +
ps31*exp((0.0d0,1.0d0)*kz3*(2.0d0*dval - zval - zsval))) -
(kz3**2/(e3val*k0**2))*(pp32*exp((0.0d0,1.0d0)*kz3*(zval + zsval)) +
pp31*exp((0.0d0,1.0d0)*kz3*(2.0d0*dval - zval - zsval))))

      GEyy = (1/kp**2)*(kxval**2*(exp((0.0d0,1.0d0)*kz3*abs(zval - zsval)) +
ps32*exp((0.0d0,1.0d0)*kz3*(zval + zsval)) +
ps31*exp((0.0d0,1.0d0)*kz3*(2.0d0*dval - zval - zsval))) +
(kyval**2*kz3**2/(e3val*k0**2))*(pp32*exp((0.0d0,1.0d0)*kz3*(zval + zsval)) +
pp31*exp((0.0d0,1.0d0)*kz3*(2.0d0*dval - zval - zsval))))

      GEzx = (kxval*kz3/(e3val*k0**2))*(pp32*exp((0.0d0,1.0d0)*kz3*(zval +
zsval)) - pp31*exp((0.0d0,1.0d0)*kz3*(2.0d0*dval - zval - zsval)))

      GEzy = (kyval*kz3/(e3val*k0**2))*(pp32*exp((0.0d0,1.0d0)*kz3*(zval +
zsval)) - pp31*exp((0.0d0,1.0d0)*kz3*(2.0d0*dval - zval - zsval)))

      if (abs(zval - zsval) <= 1.0d-50) then
            GEzz = (-1/(e3val*k0**2))*((kp - sign(1.0e0,(zval -
zsval))*kz3)**2*exp((0.0d0,1.0d0)*kz3*abs(zval - zsval)) -
kp**2*(pp32*exp((0.0d0,1.0d0)*kz3*(zval + zsval)) +
pp31*exp((0.0d0,1.0d0)*kz3*(2.0d0*dval - zval - zsval))) +
(0.0d0,1.0d0)*2.0d0*kz3)
      else
            GEzz = (-1/(e3val*k0**2))*((kp - sign(1.0e0,(zval -
zsval))*kz3)**2*exp((0.0d0,1.0d0)*kz3*abs(zval - zsval)) -
kp**2*(pp32*exp((0.0d0,1.0d0)*kz3*(zval + zsval)) +
pp31*exp((0.0d0,1.0d0)*kz3*(2.0d0*dval - zval - zsval))))
      end if

      GHxz2 = (exp(-(0.0d0,1.0d0)*conjg(kz32)*abs(zval - zsval)) +
conjg(ps322)*exp(-(0.0d0,1.0d0)*conjg(kz32)*(zval + zsval)) +
conjg(ps312)*exp(-(0.0d0,1.0d0)*conjg(kz32)*(2.0d0*dval - zval - zsval)))

      GHyz2 = kx2val*(exp(-(0.0d0,1.0d0)*conjg(kz32)*abs(zval - zsval)) +
conjg(ps322)*exp(-(0.0d0,1.0d0)*conjg(kz32)*(zval + zsval)) +
conjg(ps312)*exp(-(0.0d0,1.0d0)*conjg(kz32)*(2.0d0*dval - zval - zsval)))
```

```
      GHxy2 = (conjg(kz32)/kp2**2)*(kyval**2*(exp(-
(0.0d0,1.0d0)*conjg(kz32)*abs(zval - zsval)) + conjg(ps322)*exp(-
(0.0d0,1.0d0)*conjg(kz32)*(zval + zsval)) - conjg(ps312)*exp(-
(0.0d0,1.0d0)*conjg(kz32)*(2.0d0*dval - zval - zsval))) + (kx2val**2*(kp2**2 +
conjg(kz32**2))/(conjg(e3val)*k0**2))*(conjg(pp322)*exp(-
(0.0d0,1.0d0)*conjg(kz32)*(zval + zsval)) - conjg(pp312)*exp(-
(0.0d0,1.0d0)*conjg(kz32)*(2.0d0*dval - zval - zsval))))

      GHyy2 = (-kx2val*kyval*conjg(kz32)/kp2**2)*((exp(-
(0.0d0,1.0d0)*conjg(kz32)*abs(zval - zsval)) + conjg(ps322)*exp(-
(0.0d0,1.0d0)*conjg(kz32)*(zval + zsval)) - conjg(ps312)*exp(-
(0.0d0,1.0d0)*conjg(kz32)*(2.0d0*dval -zval - zsval))) - ((kp2**2 +
conjg(kz32**2))/(conjg(e3val)*k0**2))*(conjg(pp322)*exp(-
(0.0d0,1.0d0)*conjg(kz32)*(zval + zsval)) - conjg(pp312)*exp(-
(0.0d0,1.0d0)*conjg(kz32)*(2.0d0*dval - zval - zsval))))

      if (abs(zval - zsval) <= 1.0d-50) then
            GHzy2 = (-kx2val/(conjg(e3val)*k0**2))*((kp2 - sign(1.0e0,(zval -
zsval))*conjg(kz32))**2*exp(-(0.0d0,1.0d0)*conjg(kz32)*abs(zval - zsval)) -
(kp2**2 + conjg(kz32**2))*(conjg(pp322)*exp(-(0.0d0,1.0d0)*conjg(kz32)*(zval +
zsval)) + conjg(pp312)*exp(-(0.0d0,1.0d0)*conjg(kz32)*(2.0d0*dval - zval -
zsval))) - 2.0d0*(0.0d0,1.0d0)*conjg(kz32))
      else
            GHzy2 = (-kx2val/(conjg(e3val)*k0**2))*((kp2 - sign(1.0e0,(zval -
zsval))*conjg(kz32))**2*exp(-(0.0d0,1.0d0)*conjg(kz32)*abs(zval - zsval)) -
(kp2**2 + conjg(kz32**2))*(conjg(pp322)*exp(-(0.0d0,1.0d0)*conjg(kz32)*(zval +
zsval)) + conjg(pp312)*exp(-(0.0d0,1.0d0)*conjg(kz32)*(2.0d0*dval - zval -
zsval))))
      end if

      fkx2 = imag(exp((0.0d0,1.0d0)*(kxval - kx2val)*xval)*(GEyx*GHxz2 +
GEyy*GHyz2 + GEzx*GHxy2 + GEzy*GHyy2 + GEzz*GHzy2)/((kx2val -
kxval)*kz3*conjg(kz32)))  ! this is the function to integrate
```

Appendix C

EOT Mask Set

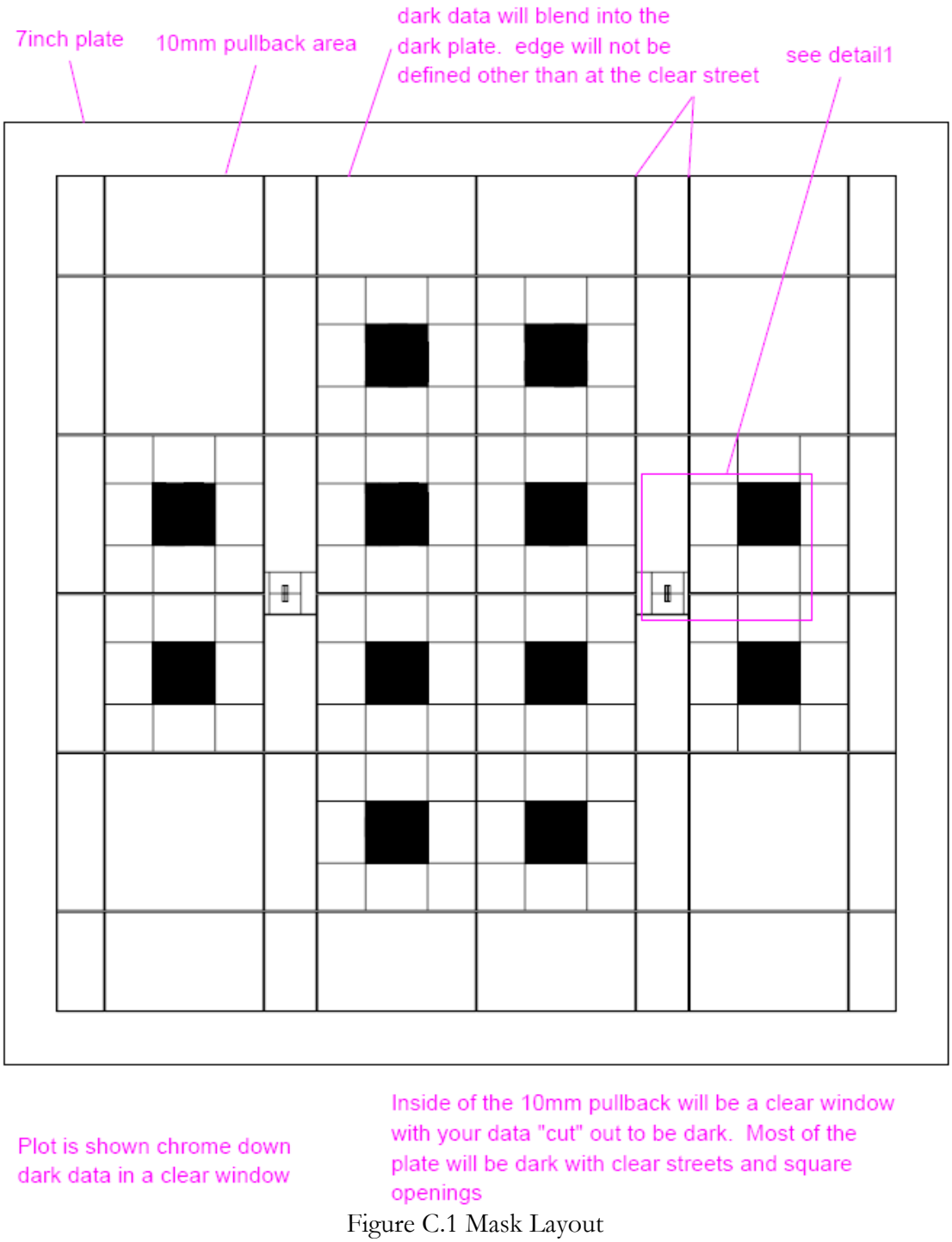

Figure C.1 Mask Layout

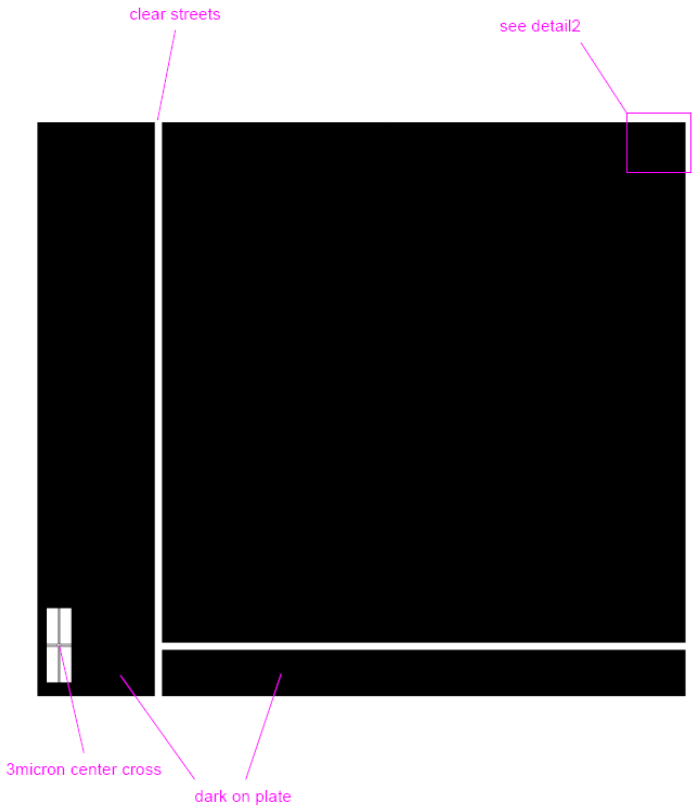

Figure C.2 Mask Detail 1

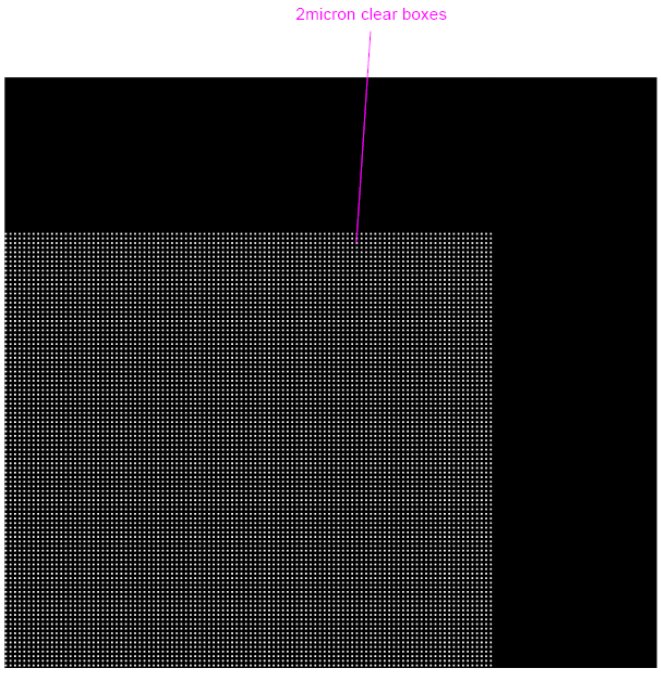

Figure C.3 Mask Detail 2

References

[1] U. Fano, "*Atomic Theory of Electromagnetic Interactions in Dense Materials*", Physical Review **103**, 1202–18 (1956 September 1).

[2] R. H. Ritchie, "*Plasma Losses by Fast Electrons in Thin Films*", Physical Review **106**, 874-81 (1957).

[3] S. L. Cunningham, A. A. Maradudin, and R. F. Wallis, "*Effect of a Charge Layer on the Surface Plasmon-Polariton Dispersion Curve*", Physical Review B **10**, 3342 (1974).

[4] M. L. Brongersma and P. G. Kik, *Surface Plasmon Nanophotonics* (Springer, 2007).

[5] J. Homola, S. S. Yee, and G. Gauglitz, "*Surface Plasmon Resonance Sensors: Review*", Sensors and Actuators B: Chemical **54**, 3-15 (1999).

[6] M. Sakaguchi, T. Thio, R. A. Linke, T. W. Ebbesen, and H. J. Lezec, "*Surface Plasmon-Enhanced Read/Write Heads for Optical Data Storage Media*",U.S. Patent 6834027, 2004 December 21

[7] M. Moskovits, "*Surface-Enhanced Raman Spectroscopy: A Brief Retrospective*", J. Raman. Spec. **36**, 485-96 (2005).

[8] H. Ditlbacher, J. R. Krenn, G. Schider, A. Leitner, and F. R. Aussenegg, "*Two-Dimensional Optics with Surface Plasmon Polaritons*", Applied Physics Letters **81**, 1762-4 (2002).

[9] J. R. Krenn, H. Ditlbacher, G. Schider, A. Hohenau, A. Leitner, and F. R. Aussenegg, "*Surface Plasmon Micro- and Nano-Optics*", Journal of Microscopy **209**, 167-72 (2003 March).

[10] T. Nikolajsen, K. Leosson, and S. I. Bozhevolnyi, "*Surface Plasmon Polariton Based Modulators and Switches Operating at Telecom Wavelengths*", Applied Physics Letters **85**, 5833-5 (2004 December 13).

[11] A. Narayanaswamy and G. Chen, "*Direct Computation of Thermal Emission from Nanostructures*", Annual Review of Heat Transfer **14**, 169-96 (2005).

[12] A. Narayanaswamy and G. Chen, "*Surface Modes for Near-Field Thermophotovoltaics*", Applied Physics Letters **82**, 3544-6 (2003).

[13] W. L. Barnes, A. Dereux, and T. W. Ebbesen, "*Surface Plasmon Subwavelength Optics*", Nature **424**, 824-30 (2003).

[14] W. L. Barnes, "*Surface Plasmon–Polariton Length Scales: A Route to Sub-Wavelength Optics*", Journal of Optics A: Pure and Applied Optics **8**, S87-S93 (2006).

[15] J. R. Sambles, G. W. Bradbery, and F. Z. Yang, "*Optical-Excitation of Surface-Plasmons - An Introduction.*", Contemporary Physics **32**, 173-83 (1991).

[16] *Proceedings of a One-Day Workshop of the Thin Films and Surfaces Group* (The Institute of Physics, London, 1987 November 25).

[17] H. Raether, *Surface Plasmons on Smooth and Rough Surfaces and on Gratings* (Springer-Verlag, Berlin, 1988).

[18] E. Burstein and F. D. Martini, *Proceedings of the First Taormina Research Conference on the Structure of Matter* (Pergamon, Taormina, Italy, 1972 October 2-6).

[19] V. M. Agranovich and R. Loudon, *Surface Excitations* (North-Holland, New York, 1984).

[20] D. G. Cahill, W. K. Ford, K. E. Goodson, G. D. Mahan, A. Majumdar, H. J. Maris, R. Merlin, and S. R. Phillpot, "*Nanoscale Thermal Transport*", Journal of Applied Physics **93**, 793-818 (2003 January 15).

[21] K. E. Goodson, "*Thermal Conduction in Nonhomogeneous CVD Diamond Layers in Electronic Microstructures*", Journal of Heat Transfer, **118**, 279-86 (1996 May).

[22] G. Chen, in *Semiconductors and Semimetals, Recent Trends in Thermoelectric Materials Research*, edited by T. Tritt (Academic Press, San Diego, 2001), Vol. 71, p. 203-59.

[23] D. L. Mills, "*Attenuation of Surface Polaritons by Surface Roughness*", Physical Review B **12**, 4036–46 (1975 November 15).

[24] J. Schoenwald, E. Burstein, and J. M. Elson, "*Propagation of Surface Polaritons over Macroscopic Distances at Optical Frequencies*", Solid State Communications **12**, 185-9 (1973).

[25] J. J. Burke, G. I. Stegeman, and T. Tamir, "*Surface-Polariton-Like Waves Guided by Thin, Lossy Metal Films*", Physical Review B **33**, 5186–201 (1986 April 15).

[26] R. Carminati and J.-J. Greffet, "*Near-Field Effects in Spatial Coherence of Thermal Sources*", Physical Review Letters **82**, 1660–3 (1999 February 22).

[27] J.-P. Mulet, K. Joulain, R. Carminati, and J.-J. Greffet, "*Nanoscale Radiative Heat Transfer Between a Small Particle and a Plane Surface*", Applied Physics Letters **78**, 2931-3 (2001 May 7).

[28] Z. Lenac and M. S. Tomas, "*Enhanced Molecular Fluorescence Mediated by Long-Range Surface Polaritons*", Surface Science **215**, 299 (1989).

[29] P. Andrew and W. L. Barnes, "*Energy Transfer Across a Metal Film Mediated by Surface Plasmon Polaritons*", Science **306**, 1002 (2004 November 5).

[30] T. W. Ebbesen, H. J. Lezec, H. F. Ghaemi, T. Thio, and P. A. Wolff, "*Extraordinary Optical Transmission Through Sub-Wavelength Hole Arrays*", Nature **391**, 667 (1998).

[31] H. A. Bethe, "*Theory of Diffraction by Small Holes*", Physical Review **66**, 163 (1944).

[32] W. L. Barnes, W. A. Murray, J. Dintinger, E. Devaux, and T. W. Ebbesen, "*Surface Plasmon Polaritons and Their Role in the Enhanced Transmission of Light through Periodic Arrays of Subwavelength Holes in a Metal Film*", Phys. Rev. Lett. **92**, 107401 (2004).

[33] H. F. Ghaemi, T. Thio, D. E. Grupp, T. W. Ebbesen, and H. J. Lezec, "*Surface Plasmons Enhance Optical Transmission Through Subwavelength Holes*", Phys. Rev. B **58**, 6779 (1998).

[34] D. E. Grupp, H. J. Lezec, T. W. Ebbesen, K. M. Pellerin, and T. Thio, "*Crucial Role of Metal Surface in Enhanced Transmission Through Subwavelength Apertures*", Appl. Phys. Lett. **77**, 1569 (2000).

[35] T. J. Kim, T. Thio, T. W. Ebbesen, D. E. Grupp, and H. J. Lezec, "*Control of Optical Transmission Through Metals Perforated with Subwavelength Hole Arrays*", Opt. Lett. **24**, 256 (1999).

[36] T. Thio, H. F. Ghaemi, H. J. Lezec, P. A. Wolff, and T. W. Ebbesen, "*Surface-Plasmon-Enhanced Transmission Through Hole Arrays in Cr Films*", J. Opt. Soc. Am. B **16**, 1743 (1999 October).

[37] J. Bravo-Abad, F. J. García-Vidal, and L. Martín-Moreno, "*Resonant Transmission of Light Through Finite Chains of Subwavelength Holes in a Metallic Film*", Physical Review Letters **93**, 227401 (2004).

[38] D. L. C. Chan, M. Soljacic, and J. D. Joannopoulos, "*Thermal Emission and Design in One-Dimensional Periodic Metallic Photonic Crystal Slabs*", Physical Review E **74**, 016609 (2006).

[39] F. J. Garcia-Vidal, L. Martín-Moreno, and J. B. Pendry, "*Surfaces with Holes in Them: New Plasmonic Metamaterials*", Journal of Optics A: Pure and Applied Optics **7**, S97-S101 (2005 February).

[40] J. B. Pendry, L. Martín-Moreno, and F. J. Garcia-Vidal, "*Mimicking Surface Plasmons with Structured Surfaces*", Science Magazine **305**, 847-8 (2004 August 6).

[41] W. Fan, S. Zhang, B. Minhas, K. J. Malloy, and S. R. J. Brueck, "*Enhanced Infrared Transmission through Subwavelength Coaxial Metallic Arrays*", Phys. Rev. Lett. **94**, 033902 (2005).

[42] L. Martín-Moreno, F. J. García-Vidal, H. J. Lezec, K. M. Pellerin, T. Thio, J. B. Pendry, and T. W. Ebbesen, "*Theory of Extraordinary Optical Transmission through Subwavelength Hole Arrays*", Phys. Rev. Lett. **86**, 1114 (2001).

[43] D. Korobkin, Y. Urzhumov, B. N. III, G. Shvets, Z. Zhang, and .D.Mayergoyz, "*Giant Transmission and Dissipation in Perforated Films Mediated by Surface Phonon Polaritons*", e-print physics/0606207 (2006).

[44] N. W. Ashcroft and N. D. Mermin, *Solid State Physics* (Thomson Learning, 1976).

[45] E. D. Palik, *Handbook of Optical Constants of Solids* (Academic Press, Orlando, 1985).

[46] P. B. Johnson and R. W. Christy, "*Optical Constants of the Noble Metals*", Physical Review B **6**, 4370-9 (1972 December 15).

[47] P. B. Johnson and R. W. Christy, "*Optical Constants of Transition Metals: Ti, V, Cr, Mn, Fe, Co, Ni and Pd*", Physical Review B **9**, 5056-70 (1974 June 15).

[48] P. B. Johnson and R. W. Christy, "*Optical Constants of Copper and Nickel as a Function of Temperature*", Physical Review B **11**, 1315-23 (1975 February 15).

[49] http://www.ifm.liu.se/matephys/new_page/research/sic/Chapter2.html#2.2

[50] W. G. Spitzer, D. Kleinman, and J. Walsh, "*Infrared Properties of Hexagonal Silicon Carbide*", Physical Review **113**, 127 (1959).

[51] J. A. Kong, *Electromagnetic Wave Theory* (EMW Publishing, Cambridge, MA, 2000).

[52] M. Fukui, V. C. Y. So, and R. Normandin, "*Lifetimes of Surface Plasmons in Thin Silver Films*", Physica Status Solidi (b) **91**, K61 (1979).

[53] J. LeGall, M. Olivier, and J.-J. Greffet, "*Experimental and Theoretical Study of Reflection and Coherent Thermal Emission by a SiC Grating Supporting a Surface-Phonon Polariton*", Physical Review B **55**, 10105–14 (1997 April 15).

[54] M. V. Simkin and G. D. Mahan, "*Minimum Thermal Conductivity of Superlattices*", Physical Review Letters **84**, 927-30 (2000 January 31).

[55] J. B. Pendry, *Low Energy Electron Diffraction* (Academic Press, New York, 1974).

[56] K. Joulain, J.-P. Mulet, F. Marquier, R. Carminati, and J.-J. Greffet, "*Surface Electromagnetic Waves Thermally Excited: Radiative Heat Transfer, Coherence Properties and Casimir Forces Revisited in the Near Field*", Surface Science Reports **57**, 59-112 (2005).

[57] E. Anemogiannis and E. N. Glytsis, "*Multilayer Waveguides: Efficient Numerical Analysis of General Structures*", Journal of Lightwave Technology **10**, 1344-51 (1992 October).

[58] E. N. Economou, "*Surface Plasmons in Thin Films*", Physical Review **182**, 539-54 (1969 June 10).

[59] D. Sarid, "*Long-Range Surface-Plasma Waves on Very Thin Metal Films*", Physical Review Letters **47**, 1927–30 (1982 December 28).

[60] R. H. Ritchie, E. T. Arakawa, J. J. Cowan, and R. N. Hamm, "*Surface-Plasmon Resonance Effect in Grating Diffraction*", Physical Review Letters **21**, 1530-3 (1968).

[61] J. Watanabe, K. Uchinokura, and T. Sekine, "*Surface-Phonon Polariton on Grating of GaP Thin Slabs: Far-Infrared Reflection*", Physical Review B **40**, 5677-82 (1989 September 15).

[62] G. Lévêque and O. J. F. Martin, "*Optimization of Finite Diffraction Gratings for the Excitation of Surface Plasmons*", Journal of Applied Physics **100**, 124301 (2006 December 15).

[63] S. Shen, E. Forsberg, Z. Han, and S. He, "*Strong Resonant Coupling of Surface Plasmon Polaritons to Radiation Modes Through a Thin Metal Slab with Dielectric Gratings*", Journal of the Optical Society of America A **24**, 225-30 (2007).

[64] A. Kocabas, A. Dâna, and A. Aydinli, "*Excitation of a Surface Plasmon with an Elastomeric Grating*", Applied Physics Letters **89**, 041123 (2006 July 24).

[65] B. Hecht, H. Bielefeldt, L. Novotny, Y. Inouye, and D. W. Pohl, "*Local Excitation, Scattering, and Interference of Surface Plasmons*", Physical Review Letters **77**, 1889–92 (1996 August 26).

[66] H. Ditlbacher, J. R. Krenn, N. Felidj, B. Lamprecht, G. Schider, M. Salerno, A. Leitner, and F. R. Aussenegg, "*Fluorescence Imaging of Surface Plasmon Fields*", Applied Physics Letters **80**, 404-6 (2002 January 21).

[67] R. Hillenbrand, "*Towards Phonon Photonics: Scattering-Type Near-Field Optical Microscopy Reveals Phonon-Enhanced Near-Field Interaction*", Ultramicroscopy **100**, 421-7 (2004).

[68] A. Huber, N. Ocelic, D. Kazantsev, and R. Hillenbrand, "*Near-Field Imaging of Mid-Infrared Surface Phonon Polariton Propagation*", Applied Physics Letters **87**, 081103 (2005 August 22).

[69] A. Otto, "*Excitation of Nonradiative Surface Plasma Waves in Silver by the Method of Frustrated Total Reflection*", Zeitschrift fur Physik **216**, 398-410 (1968 July 8).

[70] A. Otto, in *Polaritons* (Pergamon Press, New York, 1972), p. 117-21.

[71] E. Kretschmann and H. Raether, "*Radiative Decay of Nonradiative Surface Plasmons Excited by Light*", Z. Naturforsch A. **23**, 2135-6 (1968).

[72] R. Siegel and J. R. Howell, *Thermal Radiation Heat Transfer* (Hemisphere Pub. Corp., Washington, D. C., 1992).

[73] S. Rosseland, *Theoreteical Astrophysics; Atomic Theory and the Analysis of Stellar Astrophysics and Envelopes* (Clarendon Press, Oxford, 1936).

[74] M. Lundstrom, *Fundamentals of Carrier Transport* (Cambridge University Press, New York, 2000).

[75] G. Chen, *Nanoscale Energy Transport and Conversion* (Oxford University Press, New York, 2005).

[76] J. M. Ziman, *Electrons and Phonons* (Clarendon Press, Oxford, 1960).

[77] http://www.ioffe.rssi.ru/SVA/NSM/Semicond/SiC/index.html

[78] C. Dames and G. Chen, "*Theoretical Phonon Thermal Conductivity of Si/Ge Superlattice Nanowires*", Journal of Applied Physics **95**, 682-93 (2004 January 15).

[79] Y. Goldberg, M. E. Levinshtein, and S. L. Rumyantsev, *Properties of Advanced SemiconductorMaterials GaN, AlN, SiC, BN, SiC, SiGe* (John Wiley & Sons, New York, 2001).

[80] A. F. Mills, *Heat and Mass Transfer* (Irwin, Boston, 1995).

[81] S. Rytov, Sov. Phys. JETP **6**, 130 (1978).

[82] S. Rytov, Y. Kravtsov, and V. Tatarskii, *Principles of Statistical Radiophysics* (Springer-Verlag, Berlin, 1989).

[83] L. Tsang, J. A. Kong, and K. H. Ding, *Scattering of Electromagnetic Waves* (Wiley, New York, 2000).

[84] J. E. Sipe, "*New Green-Function Formalism for Surface Optics*", Journal of the Optical Society of America B **4**, 481-9 (1987).

[85] L. D. Landau, E. M. Lifshitz, and L. P. Pitaevskii, *Statistical Physics* (Pergamon Press, Oxford, 1980).

[86] H. B. Callen and T. A. Welton, "*Irreversibility and Generalized Noise*", Physical Review **83**, 34-40 (1951).

[87] P. J. Davis and P. Rabinowitz, *Methods of Numerical Integration* (Academic Press, Inc., New York, 1984).

[88] W. H. Press and G. R. Farrar, "*Recursive Stratified Sampling for Multidimensional Monte Carlo Integration*", Computers in Physics **4**, 190–5 (1990).

[89] H. Niederreiter, *Society for Industrial and Applied Mathematics*, 1992).

[90] I. M. Sobol, "*The Distribution of Points in a Cube and the Approximate Evaluation of Integrals*", USSR Comput. Math. Math. Phys. **7**, 86 (1967).

[91] H. Faure, "*Discrepance de Suites Associees a un Systeme de Numeration (en Dimensions)*", Acta Arith. **41**, 337-51 (1982).

[92] R. Piessens, E. d. Doncker-Kapenga, C. W. Uberhuber, and D. K. Kahaner, *QUADPACK A Subroutine Package for Automatic Integration* (Springer Verlag, 1983).

[93] A. S. Kronrod, *Nodes and Weights of Quadrature Formulas.* (Consultants Bureau, New York, 1965).

[94] P. Wynn, "*On a Device for Computing the em(Sn) Transformation*", Math. Comp. **10**, 91-6 (1956).

[95] D.-Z. A. Chen, A. Narayanaswamy, and G. Chen, "*Surface Phonon-Polariton Mediated Thermal Conductivity Enhancement of Amorphous Thin Films*", Physical Review B **72**, 155435 (2005 October).

[96] R. Cools and A. Haegemans., "*Algorithm 824: CUBPACK: A Package for Automatic Cubature; Framework Description.*", ACM Transactions on Mathematical Software **29**, 287-96 (2003).

[97] T. O. Espelid and A. Genz, "*DECUHR: An Algorithm for Automatic Integration of Singular Functions over a Hyperrectangular Region*", Numerical Algorithms **8**, 201-20 (1994).

[98] P. Dawson, B. A. F. Puygranier, and J.-P. Goudonnet, "*Surface Plasmon Polariton Propagation Length: A Direct Comparison Using Photon Scanning Tunneling Microscopy and Attentuate Total Reflection*", Physical Review B **63**, 205410 (2001).

[99] Y. Kuwamura, Y. Yokota, M. Fukui, and O. Tada, "*ATR Mode of Surface Polaritons*", Journal of the Physical Society of Japan **51**, 2962-5 (1982 September).

[100] Y. Kuwamura, M. Fukui, and O. Tada, "*Experimental Observation of Long-Range Surface Plasmon Polaritons*", Journal of the Physical Society of Japan **52**, 2350-5 (1983 July).

[101] H. Tsuchida, I. Kamata, and K. Izumi, "*Infrared Attenuated Total Reflection Spectroscopy of 6H–SiC(0001) and (0001-bar) Surfaces*", Journal of Applied Physics **85**, 3569-75 (1999 April 1).

[102] K. Torii, T. Koga, T. Sota, T. Azuhata, S. F. Chichibu, and S. Nakamura, "*An Attenuated-Total-Reflection Study on the Surface Phonon-Polariton in GaN*", Journal of Physics: Condensed Matter **12**, 7041-4 (2000).

[103] S. S. Ng, Z. Hassan, and H. A. Hassan, "*Experimental and Theoretical Studies of Surface Phonon Polariton of AlN Thin Film*", Applied Physics Letters **90**, 081902 (2007).

[104] M. Born and E. Wolf, *Principles of Optics* (Cambridge University Press, New York, 1999).

[105] S. D. Senturia, *Microsystem Design* (Kluwer Academic Publishers, Boston, 2001).

[106] G. G. Stoney, "*The Tension of Metallic Films Deposited by Electrolysis*", Proceedings of the Royal Society **A82**, 172-5 (1909).

[107] C. A. Klein, "*How Accurate are Stoney's Equation and Recent Modifications*", Journal of Applied Physics **88**, 5487-9 (2000 November 1).

[108] Z. Cao and X. Zhang, "*Density Change and Viscous Flow During Structural Relaxation of Plasma-Enhanced Chemical-Vapor-Deposited Silicon Oxide Films*", Journal of Applied Physics **96**, 4273 (2004 October 15).

[109] X. Zhang, K.-S. Chen, R. Ghodssi, A. A. Ayon, and S. M. Spearing, "*Residual Stress and Fracture in Thick Tetraethylorthosilicate (TEOS) and Silane-Based PECVD Oxide Films*", Sensors and Actuators A **91**, 373-80 (2001).

[110] B. Lojek, *11th IEEE International Conference on Advanced Thermal Processing of Semiconductors. RTP 2003* (IEEE, Charleston, NC, 2003).

[111] Y. Laghla and E. Scheid, "*Optical Study of Undoped, B or P-doped Polysilicon*", Thin Solid Films **306**, 67 (1997).

[112] C. Genet and T. W. Ebbesen, "*Light in Tiny Holes*", Nature **445**, 39-46 (2007 January 4).

[113] C. Genet, M. P. v. Exter, and J. P. Woerdman, "*Fano-type Interpretation of Red Shifts and Red Tails in Hole Array Transmission Spectra*", Opt. Commun. **225**, 331-6 (2003).

[114] A. Taflove and S. C. Hagness, *Computational Electrodynamics: The Finite-Difference Time-Domain Method* (Artech, Norwood, MA, 2000).

[115] P. Lalanne and E. Silberstein, "*Fourier-Modal Methods Applied to Waveguide Computational Problems*", Optics Letters **25**, 1092-4 (2000).

[116] E. Silberstein, P. Lalanne, J.-P. Hugonin, and Q. Cao, "*Use of Grating Theories in Integrated Optics*", Journal of the Optical Society of America A **18**, 2865-75 (2001).

[117] D.-Z. A. Chen, R. Hamam, M. Soljacic, J. D. Joannopoulos, and G. Chen, "*Extraordinary Optical Transmission Through Sub-Wavelength Holes in a Polaritonic Silicon Dioxide Film*", Applied Physics Letters **90**, 181921 (2007 April 30).

[118] D. G. Cahill, "*Thermal Conductivity Measurement from 30 to 750 K: The 3ω Method*", Review of Scientific Instruments **61**, 802-8 (1990).

[119] C. Dames and G. Chen, "*1, 2, and 3ω Methods for Measurement of Thermal Properties*", Review of Scientific Instruments **76**, 124902 (2005).

[120] K. E. Goodson, *Thermal Conduction in Microelectronic Circuits,* Ph. D. Thesis, Mechanical Engineering Department, Massachusetts Institute of Technology, 1993.

[121] T. M. Tritt, *Thermal Conductivity: Theory, Properties, and Applications* (Kluwer Academic/Plenum Publishers, Boston, 2004).

[122] A. Christ, T. Zentgraf, S. G. Tikhodeev, N. A. Gippius, O. J. F. Martin, J. Kuhl, and H. Giessen, "*Interaction Between Localized and Delocalized Surface Plasmon Polariton Modes in a Metallic Photonic Crystal*", Physica Status Solidi(b) **243**, 2344-8 (2006 August).

[123] E. L. Albuquerque and M. G. Cottam, "*Superlattice Plasmon-Polaritons*", Physics Reports **233**, 67-135 (1993).